Receiver Design for a Directional Borehole Radar System

Vom Fachbereich Elektrotechnik, Informationstechnik, Medientechnik
der Bergischen Universität zur Erlangung des akademischen Grades eines

Doktor Ingenieur

genehmigte Dissertation

von

Olaf Borchert
aus Solingen

Referent:	Univ.-Prof. Dr.-Ing. A. Glasmachers
Korreferent:	Univ.-Prof. Dr.-Ing. H. Chaloupka
Tag der mündlichen Prüfung:	11. Juli 2008

Acknowledgments

It is important to acknowledge key individuals, who without their enormous support, mentoring and help in my research work and study, wouldn't have made this work possible.

Firstly I would like to thank my supervisor, Prof. Dr.-Ing. A. Glasmachers, who over the years provided his professional guidance, numerous technical support and mentoring. I feel I have richly benefited from his expertise knowledge and advice, and enjoyed working together in his department.

As well I would like to thank Prof. Dr.-Ing. H. Chaloupka for spending much time revising my work. I also take the opportunity to thank my work colleagues who played an invaluable part in their support in various ways over the years. Notably I appreciate the great support that Jutta Winter made in organizing business trips, breakfasts and events. Also many thanks to the following individuals for their contributions: M. Aliman, K. Behaimanot, S. Gencol, M. Kühn, A. Laue, E. Matz, W. Risse, D. Rozic and J. Schmackers.

I want to thank the German Federal Ministry of Education and Research (BMBF) for partly funding this research project, reference number 02C1084 [1]. It was very enjoyable to work together with a team with people like A. Becker (BUW [2]), U. Buschmann (BGR [3]), D. Eisenburger (BGR [3]), V. Gundelach (BGR [3]), M. Kaluza (BUW [2]), G. Kroeger (DMT [4]), J. Lichau (DMT [4]), T. Reinhards (BUW [2]), K. Siever (DMT [4]).

I want to express much gratitude to my family and friends for all their support during my research period. Finally I want to thank my wife, Heather, for her support and her part in the correcting and editing of my thesis.

Solingen, August 2008

Olaf Borchert

Contents

List of Figures

List of Tables

Glossary

$\Delta\Omega$	Difference in circular frequency
Δt	Time difference
ϵ_0	$\epsilon_0 = 8.854 \cdot 10^{-12} \frac{As}{Vm}$
ι	Number of interleaved sampling intervals
●—○	Fourier or Laplace backward transformation
○—●	Fourier or Laplace forward transformation
μs, μsec	Microseconds
μ_0	$\mu_0 = 4\pi \cdot 10^{-7} \frac{Vs}{Am}$
ω	Circular frequency $\omega = 2\pi f$
ω_0	Circular frequency of an oscillator
ω_1	Circular frequency of a damped resonant circuit
Ω_s	Circular sampling frequency
σ	Variance, radar cross section, conductivity
τ_0	Start value for τ
A	Amplitude
c_0	Speed of light in vacuum $c_0 = 2.997925 \cdot 10^8 \frac{m}{s}$
E	Error factor
F_s	Sampling frequency $F_s = \frac{1}{T_s}$
k_B	Boltzman's constant, $k_B = 1.38 \cdot 10^{-23} \frac{J}{K}$
M	Number of samples
n_0	Number of zero crossings
T_s	Sampling interval, $T_s = \frac{1}{F_s}$
$T_{\mathbf{is}}$	Interleaved sampling interval, $T_{\text{is}} = \frac{1}{F_{\text{is}}}$
V_T	Temperature voltage of a transistor, $V_T \approx 26$ mV at room temperature
ADC	Analog-to-Digital Converter
BGR	Bundesanstalt für Geowissenschaften und Rohstoffe / Federal Institute for Geosciences and Natural Resources
CW	Continuous Wave
DAC	Digital-to-Analog Converter
DC	Direct Current
DCM	Digital Clock Manager
DLL	Delay-Locked Loop
DNL	Differential Nonlinearity, measured in LSB
DR	Dynamic Range
DSL	Digital Subscriber Line, technologies providing digital data transmission over wires of a local telephone network
ENOB	Effective number of Bits
FET	Field Effect Transistor
FFT	Fast Fourier Transformation
FIFO	First In, First Out
FMCW	Frequency Modulated Continuous Wave
FPGA	Field Programmable Gate Array
FSM	Finite State Machine
GPR	Ground Penetrating Radar
LAN	Local Area Network
LSB	Least Significant Bit
LTI	Linear Time Invariant
MSPS	Mega Samples per Second
ns, nsec	Nanoseconds

GLOSSARY

PAM	Pulse Amplitude Modulation
PROM	Programmable Read Only Memory
ps, psec	Picoseconds
Q	Quality factor
rad	Radian, 1 rad = $\frac{180^\circ}{\pi}$
Radar	Radio Detection and Ranging
RCS	Radar Cross Section
SCR	Signal to Clutter Ratio
SFCW	Stepped Frequency Continuous Wave
SINAD	Signal-to-Noise and Distortion
SNR	Signal-to-Noise Ratio
SPI	Serial Peripheral Interface
TCP/IP	Transmission Control Protocol / Internet Protocol
UXO	Unexploded Ordnance
vf	Velocity factor describing the reduced wave propagation in regard to the speed of light c_0
VGA	Variable Gain Amplifier
WAN	Wide Area Network

1

Introduction

There are materials where, for human beings, visible light cannot be used to illuminate the environment with its distinct features and hidden objects. One of these media is the solid surface of the earth consisting of various kinds of soil, rocks or ice. Some of these buried objects or features of the ground are dangerous to humans. Hidden land mines and other unexploded ordnances (UXO) can destroy lives. The same is true for water or gas filled cavities which are opened during mining operations. As there are harmful hazards below the surface of the earth can also be the sanctuary of hidden treasures. A vast pool of natural resources lays underground. These valuable materials are brought to the surface by the mining industry. Mining is in need of more and more energy-efficient operations, including cost-effective yet sophisticated mapping tools to reduce unneeded excavated material. Moreover, new natural resources are constantly explored. These operations need efficient tools to detect the features of the subsurface. Mechanical tools used in digging up the ground or drilling into the subsurface requires extensive work even when modern machinery is used. As an example, the drilling process for boreholes into relatively soft subsurface materials, e.g. salt, can be considered. Depending on the environment and the diameter the drilling operation is in general quite slow. The hole is progressing only a few meters per hour. Moreover, the bore equipment used in underground mining needs two to four miners operating the drill and borehole crawler.

Today there are many instruments producing images of materials where visible light cannot get through. Examples can be found in the medical field with X-rays or ultrasound imaging where even three-dimensional pictures are possible. Moreover, advanced radar technology enables airplanes to see through clouds. A similar technology is used to 'see' through the subsurface of the earth. Among other surveying methods seismic reflection, electrical resistivity measurements and magnetic methods are employed.

Ground penetrating radar (GPR) is one of these non-destructive instruments to visualize the features of the ground. It can be used from a distance, such as in helicopters, and locally where the radar system is in direct contact with soil or rock. This technology has a variety of applications. Among other methods, GPR is used to help archaeologists to locate and map ancient buildings. In civil engineering, surface penetrating radar analyzes bridge decks and locates buried pipes and cables. Scientists conducting snow and ice research can measure the depth and its features with the help of GPR. A combination of various sensor types, including GPR, is used in latest technology for detecting and removing unexploded ordnances (UXO) like land mines. Whenever the subsurface material is to be examined closer, probes are sampled. One common method is to drill holes and examine the sampled core. In turn the borehole can be used to insert a specialized ground penetrating radar: a borehole radar probe.

Borehole radar probes are in operation worldwide in different environments. Although this is true, the technology is still a niche market compared to the surface oriented GPR systems. At the moment the constant improvement of the technology and further development is widely supported by universities and publicly-funded research programs.

Ground penetrating radar (GPR) uses electromagnetic waves to illuminate the medium under investigation. Hence, advanced technology can create three dimensional images of structures which are inside low conductive materials. Such a low conductive material is salt. At the time of writing salt seems to be suitable for storing chemical and toxic waste. This is only possible in well mapped areas. Ground penetrating radars and especially borehole radar probes are non-destructive tools with a good range to map the subsurface. The constant improvement of these radars to produce more detailed images is the goal of the publicly-funded research project BMBF 02C1084 [1] in Germany.

Next the basic principle and application of ground penetrating radar technologies are shown, while focusing on the borehole application.

1.1 Functional Principle of Ground Penetrating Radar

The typical ground penetrating radar system consists of a transmitter, receiver and data acquisition unit. The transmitter antenna radiates electromagnetic waves or broadband pulses with an antenna into the subsurface material. The electromagnetic radiation travels through the material and whenever an object, in particular a material with different electrical properties, a part of the wave is reflected and the other part continues to travel through the new material. The reflected part of the wave reaches the receiving antenna and is stored as a reflector in the data acquisition system.

A specialized GPR system designed for insertion into holes, a borehole radar system, is presented in Figure 1.1. The top part of the probe is the receiver whereas the lower module contains the transmitter.

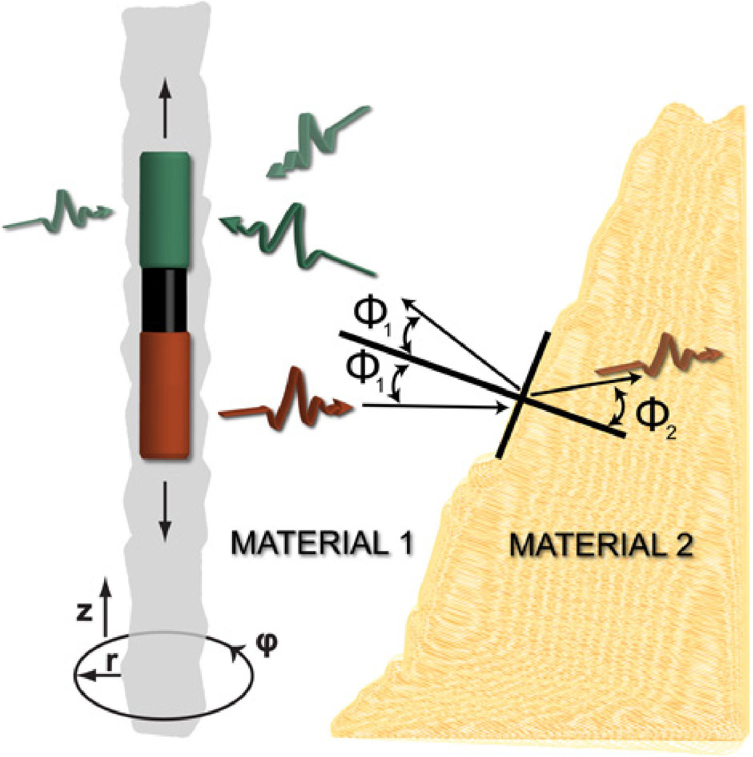

Figure 1.1: Borehole radar application principle.

The omni-directional transmitter radiates the electromagnetic waves. The waves are scattered by a contrast of materials. In particular the refraction is, among others, explained in Snell's law used in optics. Equation (1.1) represents this law where the angle depends on the refractive index of the medium n_1 and

n_2. This index represents the relation of the wave speed inside a medium c to the speed of light in vacuum c_0.

$$\frac{\sin \Phi_1}{\sin \Phi_2} = \frac{n_1}{n_2} \tag{1.1}$$

This contrast between materials is described by their refraction index. Primarily it results from the differences in conductivity and permittivity. These changes can be detected and a geologist can create a detailed map from the resulting radargram by connecting the matching echoes. Such a map containing raw data is shown in Figure 1.2.

Figure 1.2: Two-dimensional radargram example.

The properties of the location described by the coordinates z, r and φ illustrated in Figure 1.1 can be determined with the measured data. The radial distance r is defined by the two-way signal time of the echo signal T_{echo} and the signal velocity in the medium c.

$$r = \frac{T_{\text{echo}}}{2} \cdot c \tag{1.2}$$

The angle φ of such an echo is determined by the directional antenna structure. At last, the position z inside the borehole is the measured depth starting from the sidewall which represents the probe position.

More detailed information on ground penetrating radar (GPR) in general can be found, among others, in the proceedings of international GPR conferences. The foundation for this measurement method was laid more than 100 years ago as history shows.

1.2 History of Ground Penetrating Radar Technology

The foundation for radar systems in general was laid by Christian Hülsmeyer when he obtained the worldwide first patent in radar technology on April 30, 1904 (patent DE 165 546 [7]). Six years later Gotthelf Leimbach and Heinrich

Löwy [8] applied for a patent to use radar technology to locate buried objects with radar technology (patent DE 237 944). This system used surface antennas together with a continuous-wave radar. In 1926, a pulse radar system was introduced and filed for a patent (DE 489 434) by Dr. Hülsenbeck. The particular invention improved the depth resolution and is still widely used today.

One of the first worldwide ground penetrating radar survey was performed in Austria in 1929 by W. Stern [9, 10] when he measured the depth of a glacier. Thereafter GPR technology was not used anymore although some patents were filed in the field of "subsurface radar". This changed after the Second World War. Different scientific teams began to work on radar systems for viewing into the ground in the early 1970's. In the beginning, these radars were developed for military applications such as locating tunnels in the demilitarized zone between North and South Korea. Soon thereafter public utility and construction companies were interested in such radars as a practical tool to map pipes and utility lines under city streets as reported by R. M. Morey [11]. Other scientific investigations were started to use ground penetrating radar technology to explore, among others, water tables and salt deposits [12; 13].

According to Wollny [14], the first affordable GPR systems were sold in 1985 and first comprehensive reference books was written in the 1990s [15]. Nowadays there are various companies producing GPR systems while others provide measurements services. Moreover, universities worldwide conduct research in the field of ground penetrating radar systems. Most GPR systems are designed for surface applications where the transmitter and receiver are located above ground. Nevertheless there are applications where the GPR system has to fit into a narrow borehole which can be more than a kilometer long. These measurement tasks are conducted with a borehole radar as a special GPR tool.

1.3 Borehole Radar Applications

Most GPRs utilize a ground penetrating radar located on a surface of soil, concrete or snow. Holes are drilled into the subsurface and retreived borehole cores are used to analyze the material. These holes are often used to insert a GPR system fully into the opening. Thus borehole radar systems are specialized ground penetrating radars which can be inserted into boreholes. The advantage over GPR system operating above ground are its better antenna-ground coupling and less restrictions regarding radio licensing which would restrict the frequency range and transmit powers.

Borehole radars apply the same principles as surface ground penetration radar. A transmitter sends electromagnetic waves which are then detected by a receiver. The transmitter and receiver are moved to cover a specific area.

Borehole radar probes are connected with long logging cables to a control unit. The borehole diameters vary between approximately from as low as 30 mm up to some 100 mm. More room is available when caverns are measured. Such caverns are, for example, used to store oil reserves in salt deposits. Specifically the structure of the edge is of importance for safety evaluations where the diameter of such structures is in the range of some 10 meters.

The mining industry needs to map the subsurface to plan the mining locations carefully. Additional applications for borehole radar systems include the detection of fractures, cavities and voids. In civil engineering GPR is used to locate pipes and investigate hydro-power dams. Moreover, caverns are assessed and the delineation of ores is measured. The usage in salt includes salt layer investigation.

Borehole radars are used in different ways. The transmitter and receiver can be used in the same hole or can be placed in different boreholes, whereas some borehole radars are direction sensitive which enables the use of only one borehole.

1.4 Technology Development

Basically there are three major interest groups actively developing and using borehole radar systems. First there are companies developing radar systems to offer measurement services and sell GPR equipment. The second group develops borehole radars for scientific and research purposes. At last there are mining companies who develop their own radar systems which suit their specific environment which can lead to an advantage over competing mines.

Technical information about borehole radar systems can be found on the Internet for commercially available systems and radars used in science at universities around the world. In contrast, little or no information is publicly available of borehole systems designed by mining companies.

A directional borehole radar system with an antenna array connected to passive optical electrical field sensors is being worked on [16]. These optical fibers with its electronics are connected to a network analyzer for data acquisition.

Some applications, as in hard-rock mining, allow only for very small boreholes. These measurement tasks require ultra-slimline radar probes which allow only for diameters of 32 mm or even only below 25 mm. In order to achieve such small dimensions, a pulse radar system with analog optical data transmission was built [17].

Beside the hardware design, data analysis and three-dimensional reconstruction with the acquired measurement data are important. Worldwide research is conducted like among others in modeling and mapping of data acquired from several different boreholes [18].

One of the commercial directional borehole operates with a revolving bistatic radar antenna system [19]. The probe has a diameter of 160 mm and a length of 4.2 m. A pulse radar with a center frequency of 100 MHz detects objects in environments of up to 1.5 MPa pressure.

Other commercial systems mainly focus on non-directional borehole antennas. The provided borehole antennas are connected to standard data acquisition units [5; 20; 21; 22]. The advantage of such an approach is the flexibility of the data acquisition units, because no special borehole probe related electronics is provided. On the other hand special borehole radar equipment provides a better, more application specific, performance.

A battery powered pulse radar borehole system for South African gold mines for insertion into 38 mm holes was developed [23]. The omni-directional dipole antenna achieves a bandwidth of 40 MHz in environments of up to 70°C. The receiver contains several ADCs, FIFO memories and a micro controller connected to an up to 2000 m long optical link. The data acquisition is triggered by the transmitter.

One of the worldwide first directional borehole systems was developed containing two loop antennas and a dipole antenna more than 10 years ago [24; 25; 26; 27]. The particular radar probe samples the three antennas with a single multiplexed ADC while the overall receiver draws a power of 35 Watts. The main target applications of the system are caverns and salt mines whereas the antenna center frequencies can be modified from 25 MHz to 100 MHz.

1.5 Research Goals and Thesis Overview

The goal is to research design options for an adaptable directional borehole radar receiver. Flexibility is needed to explore and compare different radar measurement systems with the same tool during field tests. Although the receiver will include various options, the first receiver tests will focus on a pulse radar system. Along with the necessary modularity a high sensitivity is required, resulting in a low-noise design.

Measurement results can be more detailed and have a greater radar range with a sensitive low-noise receiver. These low-noise goals can be achieved by avoiding too many parts in the signal path as every single component adds noise. The down side to this approach is that the absolute accuracy is lower. The precision can be enhanced by calibration. Therefore the receiver design will include a test signal generator for different calibration methods. The possibilities will be explored with further research.

Despite the scientific goals, the probe handling has to be considered for simple operation by radar operators.

As technology advances with time, the electronic components become more powerful and energy efficient. New components can increase the efficiency of the borehole radar system. As a result measurement speed increases while the energy consumption is reduced at the same time. In turn the lower power requirements mean longer operating times. Moreover, smaller components lead to an overall reduced size of the radar equipment which can be used in boreholes with lower diameters. Therefore the receiver to be designed has to be built in a modular way to provide an open platform to include latest electronic parts as they become available.

The thesis starts with a brief overview of the ground physics. Thereafter the technologies are analyzed. As a third point the design of a borehole radar receiver is discussed. The practical implementation follows and the measurement results are used to review the design.

Chapter two provides the fundamentals on electromagnetic wave propagation used with ground penetrating radars. In particular the focus is on borehole radar application and especially the receiver electronics. The following chapter provides an overview of the borehole radar system while focusing on application specific details. In chapter four the radar receiver core components are analyzed and designed in detail. Thereafter the implementation of the receiver is explained. The completed receiver electronics was installed in a mechanical probe design for conducting the field test measurements. The test measurement results are presented and analyzed to show the capabilities of the radar receiver. Finally, in the last chapter the achievements of this work are summarized.

The objective when designing the borehole radar is to achieve good signal quality while providing convenient probe handling. An optimum of these goals can be achieved when the physical fundamentals and the borehole radar technology are considered together. First the physical fundamentals are reviewed.

2

Borehole Radar Fundamentals

Borehole ground penetrating radar produces images of the material around the borehole. These images should be in its maximum detail where the range of the detectable objects should be ideally as far as possible. In nature these two parameters, resolution and depth, are limited. In order to analyze the limiting factors, it is important to analyze the electromagnetic properties of the material and the propagation of electromagnetic waves in such media. At the same time different radar types have to be considered when searching for the optimal receiver design solution.

The next sections discuss these fundamentals of ground penetrating radar technology in brief, while focusing on the application of a borehole radar receiver. These fundamentals include electrical soil properties and basic radar technologies.

2.1 Electromagnetic Characteristics of Subsurface Materials

The electromagnetic waves in ground penetrating borehole radar applications are influenced by the electrical and magnetic properties of the soil under investigation. The amplitude and phase of these waves change as they travel through the soil. Therefore the soil can be viewed, in general, as a linear and time-invariant system.

The velocity of electromagnetic waves in the soil under investigation is of special importance to link the recorded echo time to a distinct location. Soils have specific propagation velocities which are determined by their permittivity and magnetic permeability describing charge storage and loss mechanisms.

Table 2.1 lists as primary characteristics permittivity and conductivity of some materials which are of importance for ground penetrating radar applications, whereas magnetic permeability of the soil is seldom of importance. The primary reason is that GPR is not effective in such materials due to the high attenuation of electromagnetic waves in magnetic materials.

Medium $T = 25°\mathrm{C}$, $f = 10$ MHz	**Dielectricity** ϵ'_r (relative)	**Loss Tangent** $\tan\delta$	**Conductivity** σ' [mS/m]
Dry Air	1.0005	≈ 0	0
Dry Clay	2.44	0.04	0.05
Wet Clay, moisture 20%	21.6	1.7	20.4
Dry Salt, fresh crystals	5.9	< 0.0002	< 0.001
Dry Sand	2.59	0.016	0.02
Wet Sand, moisture 16.8%	20	0.35	3.9

Table 2.1: Typical basic properties of some geologic materials [6].

Additional characteristics like the wave velocity and attenuation can be calculated with the primary parameters ϵ', $\tan\delta$ and σ'. The simplified equation for the electromagnetic wave velocity c in a certain material, without considering the magnetic properties, is written in (2.1). In particular, the approximation is suitable for materials with a loss tangent of $\tan\delta < 1$.

$$c \approx \frac{c_0}{\sqrt{\epsilon_r}} \tag{2.1}$$

The attenuation for non-magnetic ($\mu_r = 1$), low loss material can be estimated with Equation (2.2) [28], where the unit of α is $\frac{\mathrm{Np}}{\mathrm{m}}$.

$$\alpha \approx \frac{\sigma \cdot \sqrt{\mu_0 \cdot \mu_r}}{2 \cdot \sqrt{\epsilon_0 \cdot \epsilon_r}} \tag{2.2}$$

The typical signal velocities and attenuation for salt and air can be approximated with the above equations. Particular values are shown as examples in Table 2.2.

These properties vary with frequency, as Figure 2.1 illustrates. In general subsurface materials have a low pass filter characteristic for electromagnetic waves. In particular, the comparison of wet and dry sand highlights the influence of water on soil attenuation. Moreover, the graphs show that GPR in the

Medium $T = 25°\text{C}$, $f = 10$ MHz	**Velocity** c [m/ns]	**Attenuation** α [Np/m]
Dry Air	0.3	0
Dry Salt, fresh crystals	0.13	$51 \cdot 10^{-6}$
Dry Sand	0.19	$2.7 \cdot 10^{-3}$
Wet Sand, moisture 16.8%	0.07	$164 \cdot 10^{-3}$

Table 2.2: Velocity and attenuation of electromagnetic waves of specific geologic materials.

frequency range in a magnitude of 1 MHz up to 100 MHz is without significant dispersion for relative dry soil. This non-dispersive frequency range is of importance for ground penetrating radar applications.

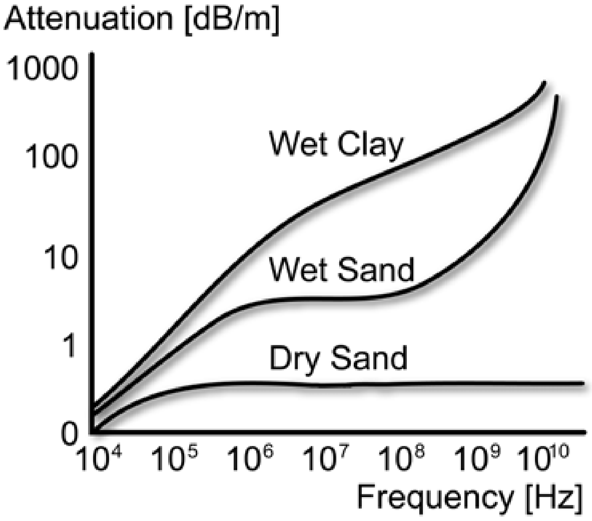

Figure 2.1: Frequency dependent attenuation of clay and sand [5].

The soil properties can be determined by measuring soil samples. One method is Time Domain Reflectometry (TDR) which uses a resonant hollow conductor where the material is inserted for investigation. The detectable change in resonant frequency of the hollow conductor is linked to the material properties. The permittivity can be calculated with the relation of the speed of light c_0 and signal velocity in the medium c in Equation (2.3).

$$\epsilon_r = \left(\frac{c_0}{c}\right)^2 \tag{2.3}$$

A more complex method to measure soil properties is known as Resonant Frequency Analysis (RFA) [29]. A RFA measurement acquires the signal strength to frequency relationship with a Vector Network Analyzer (VNA).

The electromagnetic waves in such media are attenuated by the soil to a much greater extent than air. Specifically, the low pass characteristics of soil in regard to electromagnetic waves lowers the radar range for higher frequencies. This effect is intensified by water content increasing the conductivity thus resulting in lower penetration depth. The applicable frequencies for ground penetrating are in the range with low dispersion effects as indicated in Figure 2.1. The discussed material properties dominate the electromagnetic wave propagation.

2.2 Electromagnetic Wave Propagation in Subsurface Materials

The principle of wave propagation in subsurface materials explains how the soil parameters affect the radar signals. It can be observed that the wave amplitude varies with the signal frequency and distance from the source. Abrupt changes occur when material parameters change suddenly causing reflections which are in turn detected by the radar receiver. These effects are based on electromagnetic wave propagation containing the material parameters. Accordingly the wave equations connect the subsurface material properties with the radar signals. The next paragraphs discuss some of these basic concepts briefly.

According to the Maxwell Equations [30], the propagation of electromagnetic waves can be expressed in general by two differential equations, separated in electric and magnetic fields. These equations depend on each other as in the Helmholtz wave Equation (2.4).

$$\left(\nabla^2 + \mu\epsilon\omega^2\right)\begin{pmatrix}\vec{E}\\ \vec{B}\end{pmatrix} \tag{2.4}$$

A possible solution in one dimension for such a medium is a plane wave propagating in one direction x as written in Equation (2.5) for frequency independent material parameters.

$$E(x) = E_0 \cdot e^{-j\ k\cdot x + j\ \omega\cdot t} \tag{2.5}$$

The factor E_0 is the electric field and k denotes the wave number which can be expressed with the material parameters μ and ϵ or the wavelength in the material λ like written in Equation (2.6). In fact, the wavelength λ is the distance the wave travels in one oscillation. Accordingly, propagation speed or signal wavelengths are directly linked to the material properties.

$$k = \omega \cdot \sqrt{\mu \cdot \epsilon} = \frac{\omega}{c} = \frac{2\pi}{\lambda} \tag{2.6}$$

Losses in the material are represented by complex numbers for the permeability $\boldsymbol{\mu}$ and permittivity $\boldsymbol{\epsilon}$ resulting in a complex wave number $\boldsymbol{k}$. The parameter $\boldsymbol{k}$ can be separated into an real and imaginary part to separate losses from wave propagation as indicated in Equation (2.7).

$$\boldsymbol{k} = \omega\sqrt{\boldsymbol{\mu} \cdot \boldsymbol{\epsilon}} = \beta + j\alpha \tag{2.7}$$

The complex material constants separated into a real part and an imaginary part representing material losses as in equations (2.9) and (2.8).

$$\boldsymbol{\mu} = \mu_0(\mu_r' - j\mu_r'') \tag{2.8}$$

$$\boldsymbol{\epsilon} = \epsilon_0(\epsilon_r' - j\epsilon_r'') \tag{2.9}$$

The complex dielectricity $\boldsymbol{\epsilon}$ contains the electric permittivity as the real part and the losses as the imaginary part. In ideal cases where the dielectricity is independent of frequency the imaginary part does not exist.

The relation of real and imaginary part of the permittivity $\boldsymbol{\epsilon}$ can be expressed with a loss tangent $\tan\delta_\epsilon$ like in Equation (2.10).

$$\tan\delta_\epsilon = \frac{\epsilon''}{\epsilon'} \tag{2.10}$$

The phase constant β and the attenuation constant α are used to rewrite the wave Equation (2.5):

$$E(x,t) = E_0 \cdot e^{-\alpha \cdot x} \cdot e^{+j(\omega t - \beta \cdot x)} \tag{2.11}$$

The subsurface material, used in conjunction with ground penetrating radar, has in most cases negligible magnetic properties. As a result $\mu = \mu_0$ is adequate for non-magnetic materials whereas in other cases $\mu = \mu_0\mu_r$ is valid. Finally, the loss tangent can be used to express the complex wave propagation constant $\boldsymbol{k}$ separated into its real part α (2.12) measured in $\frac{\mathrm{Np}}{\mathrm{m}}$ and imaginary part

β (2.13). These simplified equations do not include magnetic losses and the permittivity $\epsilon' = \epsilon_0 \cdot \epsilon_r'$ is frequency independent.

$$\alpha = \omega \sqrt{\frac{\mu\epsilon'}{2}\left(\sqrt{1+\tan^2\delta} - 1\right)} \tag{2.12}$$

$$\beta = \omega \sqrt{\frac{\mu\epsilon'}{2}\left(\sqrt{1+\tan^2\delta} + 1\right)} \tag{2.13}$$

In nature the material parameters $\boldsymbol{\mu}$ and $\boldsymbol{\epsilon}$ vary with frequency as Figure 2.1 illustrated earlier. Accordingly, the loss tangent for wet materials has to include the conductivity of the subsurface material incorporating the signal frequency as can be found in Equation (2.14) [15].

$$\tan\delta = \frac{\sigma' + \omega \cdot \epsilon''}{\omega \cdot \epsilon' - \sigma''} \tag{2.14}$$

Experimental studies [5; 6] show that the permittivity rises with the water content and the permittivity is lower for higher signal frequencies. After all, the properties of soil is rather complex due to the mixture of single elements with varying sizes and different characteristics.

The above equations link signal wavelengths and material properties. They explain the attenuation depending on the radar signal frequencies, thus defining limits for radar resolution and range. Moreover, the loss tangent and especially the attenuation factor α can be used to compare different soils and to estimate the achievable radar range. Further attenuation of the electromagnetic waves occur on the path from the transmitter to the receiver.

2.3 Radar Signal Path and its Parameters

The type of radar system influences the parameters of the signal path of the electromagnetic waves from the transmitter to the radar target and the received signal at the receiver. This signal path can be analyzed using the radar equation which includes the characteristics of the signal path and electronic components.

There are several interdependent characteristics to be considered. The spatial resolution describes the accuracy of the location of the radar target and the minimal detectable distance between two radar targets. The next set of characteristics, the range or penetration depth, is linked with the properties of the subsurface material and the radar transmitter including the antenna. Two other characteristics describe the unwanted received signals as signal-to-noise ratio (SNR) and signal-to-clutter ratio (SCR).

The unwanted received power from clutter are reflected signals which are received additional to the wanted power P_E. The unwanted signals can originate from external transmitters, multi-path reflections or small geology-dependent unwanted targets. The task for clutter reduction is to distinguish the received clutter from the wanted signals. In the case of moving targets it is possible to distinguish them from stationary targets to reduce the clutter. Unfortunately this method cannot be used for ground penetrating radars, because all targets are stationary. Therefore the clutter is included with the recorded data and has to be identified during data analysis by an expert and sophisticated software. Fortunately this kind of clutter is insignificant in the case of borehole radar system due to the good soil coupling.

The received power at the radar receiver, as denoted by P_R in Equation (2.15), includes the received echo from the radar target by P_E and the noise power by P_N. These two parameters together with the power of the transmitter can be used to estimate the range of the borehole radar system.

$$P_R = P_E + P_N \tag{2.15}$$

The following paragraphs analyze the components of the received power P_E with the radar equation followed by the noise power P_N.

2.3.1 Radar Equation for Received Power from Radar Target

The received power P_E from the radar target can be calculated by analyzing the signal path starting at the transmitter. The transmitter transmits the electromagnetic waves, which reach to a certain degree the radar target, and are reflected. This reflected echo signal is received, in turn, by the radar receiver as depicted for a bistatic configuration in Figure 2.2.

In the illustration a sphere with a different dielectricity ϵ_{r2} is used as the radar target. The target is illuminated by the omni-directional dipole transmitter antenna.

The next subsections follow the signal path with the depicted different signal powers and power densities. The material in the signal path is assumed to be homogeneous, isotropic and lossy.

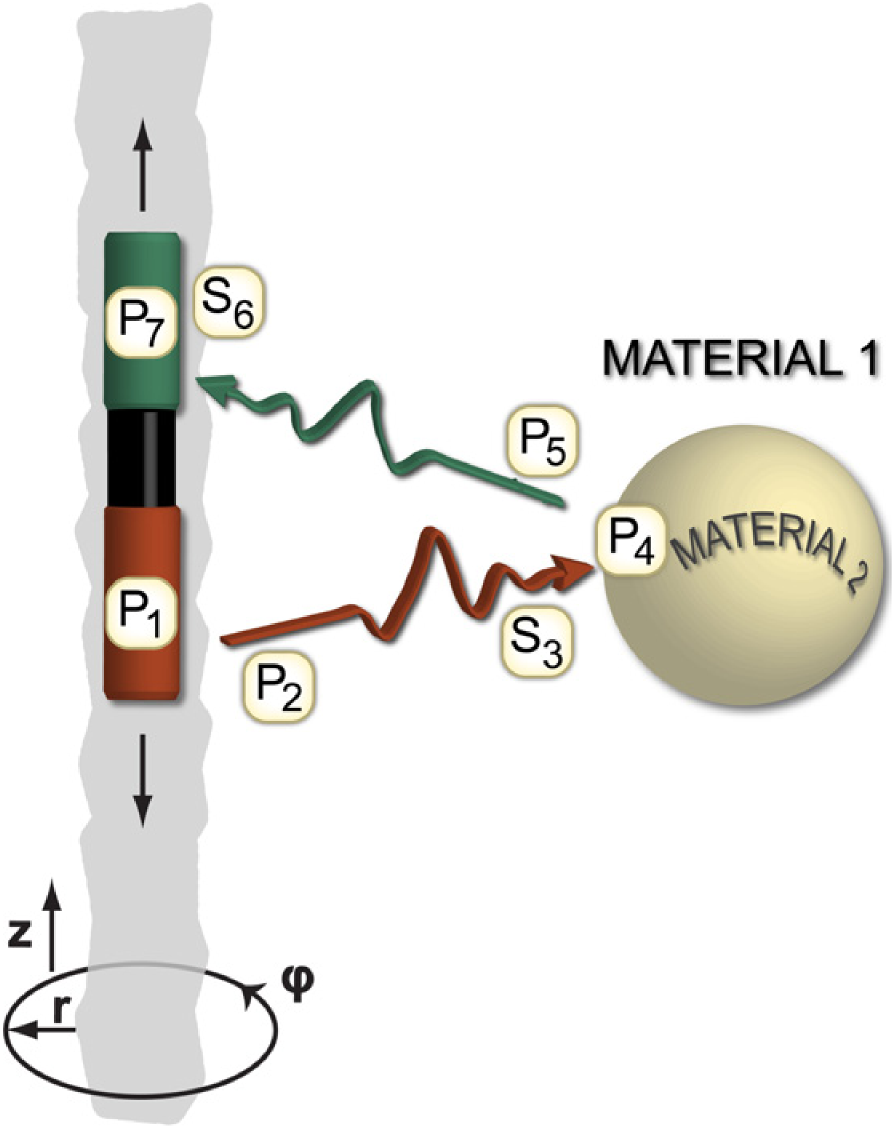

Figure 2.2: Signal path from radar transmitter to the radar receiver.

2.3.1.1 Radiated Power

The source power of the transmitter P_0 is coupled to the antennas. A loss occuring by antenna mismatch is represented by the antenna coupling factor η_{TX}. Consequently, the power at the antenna can be calculated with:

$$P_1 = \eta_{\mathrm{TX}} \cdot P_0 \tag{2.16}$$

2.3.1.2 Power Radiation in Target Direction

The radiated power in target direction depends on the antenna gain. This antenna gain factor G_{TX} includes the directivity and the antenna gain as well as the coupling to the surrounding media in the case of GPR. In cases where the air gap between antenna and subsurface material is small, the loss due to the antenna-air-material transition is very small.

$$P_2 = G_{\mathrm{TX}} \cdot P_1 \tag{2.17}$$

2.3.1.3 Power Density at Radar Target

The transmitted antenna, with its omni-directional characteristics, distributes the transmitter power over a wide area. An additional loss occurs by the attenuation of the subsurface material which further reduces the power reaching the target. The resulting power density S_3 can be calculated as follows:

$$S_3 = \frac{e^{-\alpha \cdot R_{\mathrm{TX}}}}{4 \cdot \pi \cdot R_{\mathrm{TX}}^2} \cdot P_2 \tag{2.18}$$

In Equation (2.18), the parameter α represents the loss factor of the ground and R_{TX} is the distance of the target to the transmitter.

2.3.1.4 Power Scattered by Target

The radar cross section (RCS) σ is the effective area which reflects the incoming power density S_3. The RCS factor σ depends on the properties of the specific scatterer as Table 2.3 shows. This effective area reflects an equivalent of hundred percent of the incoming power.

Object	RCS $\sigma_{\max}$	Symbols
Sphere	$\pi \cdot r^2$	r=radius
Flat Plane	$4 \cdot \pi \cdot \frac{w^2 \cdot h^2}{\lambda^2}$	h=heigth, w=width
Cylinder	$4 \cdot \pi \cdot \frac{r \cdot h^2}{\lambda}$	r=radius, h=height

Table 2.3: Radar cross section calculation for different metallic scatterers.

The cross section of a metallic sphere is independent of the wave length, but this is only valid for wavelengths statistically shorter than the diameter. This relative independence of the wavelength makes the sphere an ideal reference object.

In case of dielectric reflectors, the radar cross section σ depends not only on the shape but also the 'contrast'. The contrast can be estimated with the term $\frac{\epsilon_{\mathrm{m2}}-\epsilon_{\mathrm{m1}}}{\epsilon_{\mathrm{m2}}+\epsilon_{\mathrm{m1}}}$ where the maximum reflection coefficient of 1 occurs in the case of total reflection as with an air-metal transition.

The resulting back scattered power P_4 is calculated with

$$P_4 = \sigma \cdot S_3 \tag{2.19}$$

2.3.1.5 Power Density at Receiver

The power directed to the receiver is reduced further by spreading losses. Moreover, additional losses are caused by the attenuation of the subsurface material between the target and the receiver. The resulting power density S_5 is calculated with the next equation where the distance from the target to the receiver is denoted by R_{RX}.

$$S_5 = \frac{e^{-\alpha \cdot R_{\mathrm{RX}}}}{4 \cdot \pi \cdot R_{\mathrm{RX}}^2} \cdot P_4 \tag{2.20}$$

2.3.1.6 Power Reaching Receiver Antenna

The power density S_5 at the receiver antenna is converted to an electrical current by the effective area of the antenna A_{RX}. The resulting power is calculated with:

$$P_6 = A_{\mathrm{RX}} \cdot S_5 \tag{2.21}$$

The effective area of the antenna can be calculated with the wave velocity in the specific medium c, the signal frequency f and the antenna gain G_{RX} of the wave direction:

$$A_{\mathrm{RX}} = \frac{c^2}{4 \cdot \pi \cdot f^2} \cdot G_{\mathrm{RX}} \tag{2.22}$$

2.3.1.7 Power Received by Electronics

The power received by the antenna P_7 is processed by the receiver electronics. The matching between the receiver electronics and antenna is denoted by the factor η_{RX}. The received power is therefore calculated with

$$P_7 = \eta_{\mathrm{RX}} \cdot P_6 \tag{2.23}$$

The separate elements can be summarized in a radar equation where the influences of the different parameters can be analyzed.

2.3.1.8 Radar Equation

The factors in the previous subsections are combined to a radar equation showing the dependencies of the received power P_E in Equation (2.24).

$$P_E = \eta_{\text{RX}} \cdot \eta_{\text{TX}} \cdot A_{\text{RX}} \cdot G_{\text{TX}} \cdot \frac{e^{-\alpha \cdot (R_{\text{RX}} + R_{\text{TX}})}}{(4\pi)^2 \cdot R_{\text{RX}}^2 \cdot R_{\text{TX}}^2} \cdot \sigma \cdot P_0 \tag{2.24}$$

The equation includes material related parameters like α, σ and ϵ, as well as, technology related parameters as antenna gain and antenna matching factors. The radar cross section (RCS) σ varies with the contrast of the materials. In case of dielectric materials, which are common in geological environments characterized by GPR, the contrast is primarily determined by the material constant ϵ affecting the back scattered echo power.

In addition to the wanted received power P_E the receiver acquires unwanted noise.

2.3.2 Unwanted Noise Power

All electronic circuits contain noise generating elements. Additionally, external coupled noise sources increase these unwanted random signals. The noise power P_N of the receiver comes from different noise sources. Three specific noise sources can be identified. The first noise source is the environment. Moreover, the antenna adds noise to the received signals and at last the receiver itself is noisy.

2.3.2.1 Environmental Noise

The electromagnetic noise of the environment on the earths surface is determined by extraterrestrial noise like galactic radiation and noise coming from terrestrial transmitters. Moreover, today's electronic devices add noise to the environment. All these noise sources are attenuated by the earths soil. In fact, at a sufficient depth below the surface of the earth this above ground environmental noise is almost non-existent. Fortunately, borehole radar measurements are conducted in such 'quiet' environments.

2.3.2.2 Antenna Noise Power

The thermal antenna noise power P_{N1} can be calculated with the Boltzman's constant k_B, the temperature T and the bandwidth Δf as in Equation (2.25).

$$P_{\mathrm{N1}} = k_B \cdot T \cdot \Delta f \tag{2.25}$$

An estimated value $P_{\mathrm{N1}} = 0.41$ pW can be obtained by assuming a temperature of 300 K and a bandwidth of $\Delta f = 100$ MHz.

2.3.2.3 Receiver Noise

The magnitude of the output referred receiver noise P_{N2} can be calculated by assuming an amplifier noise of $N_{\mathrm{Amp}} = 20\ \mathrm{nV}/\sqrt{\mathrm{Hz}}$ connected to a load of $R = 100\ \Omega$. The bandwidth considered is $\Delta f = 100$ MHz.

$$P_{\mathrm{N2}} = \frac{N_{\mathrm{Amp}}^2 \cdot \Delta f}{R} = 400\ \mathrm{pW} \tag{2.26}$$

The different noise sources can be geometrically added as in Equation (2.27) where the antenna noise is negligible compared to the amplifier noise.

$$P_{\mathrm{N}} = \sqrt{P_{\mathrm{N1}}^2 + P_{\mathrm{N2}}^2} \approx P_{\mathrm{N2}} \tag{2.27}$$

The above estimations show the dominating receiver amplifier noise without considering other noise adding receiver components. This fact in particular is of importance as it shows that the receiver sensibility is not limited by the environment. As a result the lower the receiver noise is, the more sensitive the receiver is.

The analysis of the received power from the radar target P_E helps to understand the external influences of the received power P_R.

2.3.3 Analysis of Parameters Affecting the Received Power

The received power P_R of a given target is to be maximized to achieve best results. This means that the power back-scattered from the radar target has to be analyzed according to Equation (2.24). The advantage of borehole radar systems over surface operated GPR is the good antenna coupling to the ground.

The range of the radar system can be calculated when the minimal receiving power P_E is higher than the noise power P_N at the receiver while ignoring the clutter power P_C. The Equation (2.24) can be simplified to calculate the radar Range $R_{\max}$ using the following substitutions.

$$P_N = P_E \tag{2.28}$$

$$R = \frac{R_{\mathrm{RX}} + R_{\mathrm{TX}}}{2} \tag{2.29}$$

The range $R_{\max}$ for an object with full reflection ($P_5 = P_4$) without signal attenuation by the material is then approximated with

$$R_{\max} < \sqrt[4]{\eta_{\mathrm{RX}} \cdot \eta_{\mathrm{TX}} \cdot \frac{A_{\mathrm{RX}} \cdot G_{\mathrm{TX}} \cdot \sigma}{(4\pi)^2 \cdot P_N} \cdot P_0} \tag{2.30}$$

One of the important characteristics of Equation (2.30) is the fourth-root dependence. In the practical application it means that the transmitter power has to be increased 16 times to double the radar range. A more accurate result can be achieved by considering the material attenuation term $e^{-\alpha \cdot R}$. The attenuation of the material increases exponentially with the range and therefore intensifies the effect of the fourth-root. As a result a much higher transmitter power is needed for more signal power at the receiver. Such increased power levels are restricted by limited thermal conductivity and energy requirements.

The signal path of the radar signals show that the receiver plays an important role for a good radar range, because the transmitter power cannot be increased indefinitely. The radar range can be 'extended' by a sensitive low noise receiver.

2.3.4 Spatial Resolution

The spatial resolution of the radar systems depends on various parameters of the signal path and the radar system used. Moreover, the resolution can be improved with various algorithms including deconvolution filtering. According to [31] the resolution can be theoretically improved up to one eighth of the wavelength in cases with excellent data.

The minimum distance between two radar targets ΔR_{min} can be calculated in principle with Equation (2.31). The equation shows that with lower signal velocities in the medium c and higher bandwidths B, the resolution improves.

$$\Delta R_{\min} > \frac{c}{2 \cdot B} \tag{2.31}$$

The possible achievable resolution along the borehole is calculated differently. It decreases with the radar target distance due to a decreasing bandwidth, because of the grounds low pass characteristics.

2.4 Radar Systems Overview

The design of a borehole ground penetrating radar system in general includes the choice between radar technologies. Depending on the measurement task the suitable radar system technology is to be chosen. Radar systems can be grouped, as an example, into time domain or frequency based technologies. A pulse radar working in the time domain, detects the distance of objects as time difference between the transmitted pulse and pulse reception, whereas continuous wave radar systems use frequency or phase differences between transmitted and received signals.

The earthen soil can be modeled as a linear time invariant system (LTI). The soil as radar target is in regard to the measurement time invariant or stationary, because the geological features of the ground change relatively slow. Furthermore, the soil is linear because of its superposition property. For instance, the shape of electromagnetic waves propagating in the ground in general doesn't depend on the amplitude of the signals. The main characteristics of such a LTI system is that it changes only the amplitude and phase of sinusoidal input signals. There are different methods to examine the characteristics of a LTI system.

The basic principle behind all characterization methods is to transmit a signal $x(t)$ and measure the resulting output signal $y(t)$. These two signals determine the LTI system properties which are known as system transfer function $h(t) \circ\!\!-\!\!\bullet H(s)$.

2.4.1 Determining the System Transfer Function in the Time Domain

Any LTI system can be characterized by the system impulse response. In the time domain, this function is often written as $h(t)$. The output signal of an LTI system $y(t)$ is the convolution of the system impulse response $h(t)$ with the applied input signal $x(t)$ as illustrated in Figure 2.3.

The goal is to determine the system impulse response function $h(t)$ containing the system characteristics. An one step solution to obtain the system

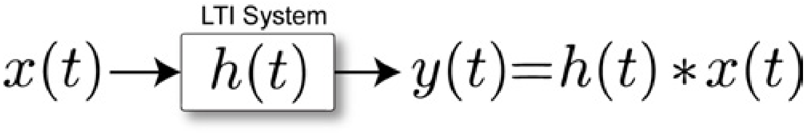

Figure 2.3: Characterization of a LTI system in the time domain.

characteristics $h(t)$ is possible by applying a Dirac delta function $\delta(t)$ as an input signal $x(t)$. The Dirac pulse function is defined with

$$\delta(t) = \begin{cases} \infty, & t = 0 \\ 0, & t \neq 0 \end{cases} \tag{2.32}$$

The system response is solved with a convolution of the Dirac pulse.

$$y(t) = h(t) * \delta(t) = \int_{-\infty}^{\infty} h(t-\tau) \cdot \delta(\tau) d\tau = h(t) \tag{2.33}$$

In the time domain, the characteristics of a LTI system can be measured directly by transmitting a Dirac pulse $\delta(t)$ into the soil and recording the response. This method, as noted in Equation (2.33), is used in impulse radar systems.

The core component of the pulse radar transmitter is the impulse generator. It generates short pulses with a high peak power mostly by means of avalanche transistors. The reliability of the pulse generation and the time uncertainties are critical parameters. An additional factor influencing the measurement time is the limited repetition rate. One of the restricting factors is the thermal conductivity of the avalanche transistors with their heatsink in combination with possibly relative high temperatures of the surrounding.

A pulsed radar transmits pulses with a large peak power and high bandwidth. The pulse width T_{PW} defines the bandwidth and at the same time resolution. The minimal resolution $\Delta R_{\min}$ defines how close two radar target can be located and still be distinguished from one another.

$$\Delta R_{\min} \approx \frac{c \cdot T_{\text{PW}}}{2} \tag{2.34}$$

Assuming a pulse width of $T_{\text{PW}} = 10$ nsec the resolution is approximately 0.65 m in salt. The pulse repetition rate is limited by the wave propagation time to the furthest radar target back to the receiver. This maximum repetition rate is one of the restricting factors for the fastest measurement speed possible.

With an assumed radar range R of 600 m, the pulse repetition rate T_{PRF} can be calculated when considering the wave propagation velocity in salt $c = 0.13\ \frac{m}{sec}$ with equation

$$T_{\mathrm{PRF}} = \frac{R}{c} \cdot 2 = \frac{600\ m}{0.l3\ \frac{m}{\mathrm{nsec}}} \cdot 2 = 9.2\ \mu\mathrm{sec} \tag{2.35}$$

The radar pulses have peak voltages of over several hundred volts resulting in a high peak power. The average power is much lower due to the relative low duty cycle. The average power of the above example can be computed assuming $T_{\mathrm{PRF}} = 10\ \mu$sec and a peak power of $P_{\mathrm{peak}} = 1$ kW.

$$P_{\mathrm{avg}} = \frac{T_{\mathrm{PW}}}{T_{\mathrm{PRF}}} \cdot P_{\mathrm{peak}} = 1\ W \tag{2.36}$$

The receiver electronics must have a wide bandwidth to record the echoes properly. At the same time, the receiver needs the capability to handle high input signals and therefore needs a quick recovery time from overmodulation.

2.4.2 Measuring the System Response in the Frequency Domain

The characterization principle of any LTI system in the frequency domain is equivalent to the time domain through an integral transformation. The Laplace transformation of the impulse response $h(t)$ is $H(s)$. Accordingly, the response of the LTI system in the frequency domain is noted in Figure 2.4.

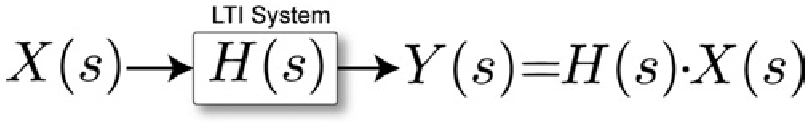

Figure 2.4: Linear time invariant system in the frequency domain.

The output $Y(s)$ represents directly the system characteristics $H(s)$ when the Heaviside or Theta function (2.37) is used as an input $X(s)$.

$$\Theta(s) = \begin{cases} 0, & s < 0 \\ 1, & s \geq 0 \end{cases} \tag{2.37}$$

The Heavisde function $\Theta(s)$ can be technically transmitted into the LTI system sequentially. The transmitter transmits all needed frequencies by the means of single sine waves and records the received phase and amplitude. Each of the frequencies is modified in phase and amplitude by the subsurface soil resulting in an exact system response $H(s)$. After such a signal sweep the system response $H(s)$ can be assembled by combining all single measurements.

In radar systems this method is represented by the various technologies operating in the frequency domain. Often not all frequencies are used as an input to the LTI system to save time and energy. Despite the imperfections of the input signal $Y(s)$ the system parameters $H(s)$ can be detected with a high accuracy.

The principle of frequency modulated radar is that a continuous modulated wave is radiated by the radar transmitter and acquired by the radar receiver at the same time. The radar receiver has a high sensitivity because the narrow bandwidth requirement for one single frequency. There are several variations of stepped frequency radars where frequency chirps, pulses or continuous waves are used. These variations require a transmitter containing a flexible signal generator with a subsequent power amplifier.

As technology with higher integration becomes more and more available, the more various forms of frequency radars are used for ground penetration radar systems and in particular borehole radars.

The requirements for the receiver are a broad receiving bandwidth where the bandwidth can be tunable in width and frequency.

2.4.3 Computing the System Characteristics with Cross-Correlation Measurements

Another form of time domain measurement is to compute the system response with cross-correlation. The method illustrated earlier in Figure 2.3 is limited to the Dirac function $\delta(t)$ as an input function. This restriction is weakened by cross-correlating the input signal $x(t)$ with the measured response of the LTI system $y(t)$. The principle is depicted in Figure 2.5.

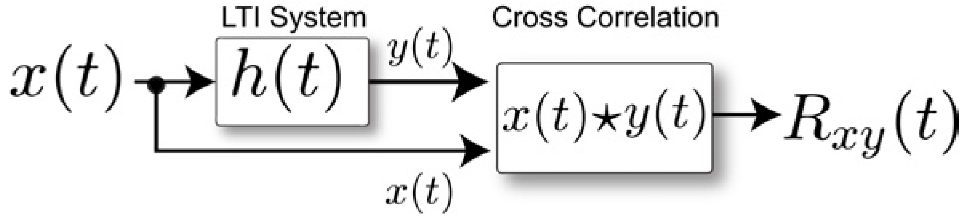

Figure 2.5: Determining LTI system characteristics with a cross-correlation measurement.

The signal $y(t)$ equals the measurable system output already defined earlier. The result of the block diagram 2.5 for $R_{xy}(t)$ is written in Equation (2.38) where the cross-correlation is represented by the $\star$ symbol and the convolution by $*$.

$$R_{xy}(t) = x(t) \star y(t) = x(t) \star (h(t) * x(t)) \tag{2.38}$$

The above Equation (2.38) can be rewritten as in Equation (2.39).

$$R_{xy}(t) = \underbrace{(x(t) \star x(t))}_{R_{xx}(t)} \cdot h(t) \tag{2.39}$$

The equation for $R_{xy}(t)$ can be simplified further by using the autocorrelation function $R_{xx}(t)$ of the input signal $x(t)$.

$$R_{xy}(t) = R_{xx}(t) \cdot h(t) \tag{2.40}$$

The continuous autocorrelation function defines the convolution of a conjugated complex signal shifted in time with original signal itself. The solution can be computed with Equation (2.41).

$$R_{xx}(t) = \lim_{T\to\infty} \frac{1}{T} \int_0^T x(\tau) \cdot x(\tau - t) d\tau \tag{2.41}$$

The result in cases of sufficient long signal sequences for $R_{xx}(t)$ is approximately equivalent to the Dirac delta function named $\delta'(t)$.

$$R_{xx}(t) = \delta'(t) \tag{2.42}$$

The above solution allows us to write the basic principle of cross-correlation radars as in Equation (2.43) which doesn't depend on the input signal anymore.

$$R_{xy}(t) = \delta' \cdot h(t) \tag{2.43}$$

The above calculation show the principle of determining the system response by cross-correlation. Although the input signal $x(t)$ is not part of Equation (2.43) there are certain requirements. These radar systems often use a so-called maximum length sequence (MLS) as an input signal $x(t)$, which contains a well defined pseudo-random binary sequence. Such cross-correlation radar measurements are used, among other fields, in acoustics [32] to determine the impulse response. Another example is found in the thesis: "Development of a modular measuring system for the determination of roomacoustic quality dimensions” [33].

In regard to the receiver cross-correlation measurements are similar except that the measurement time is not only dependent on the radar range but also on the selected input sequence.

2.5 Radar Receiver Considerations

The fundamentals of the borehole radar environment and its technology are the basis for the receiver design. Physical constraints set limits whereas technology makes the effort to reach these limits set by nature. In the case of the receiver an overview of the electromagnetic wave propagation along with the radar technology helps to define the receiver design goals.

The soil attenuates the radar signal with a low pass characteristics whereby water content has a significant influence. Therefore ground penetrating is best suited for dry materials. Moreover, a relative non-dispersive environment is needed to avoid radar signal distortion. These characteristics are found in a certain frequency range depending on the soil type.

A high resolution is only possible with high electro-magnetic wave frequencies. On the other hand, lower frequencies lead to a better radar range. After all, a compromise has to be found. In the case of a borehole radar for geological structures the goal is to have a good range with sufficient resolution. Borehole measurements were conducted with frequencies in order of 50 MHz [26; 27] with good results. As a result this receiver will be designed for frequencies up to an order of 100 MHz.

The analysis of the radar signal path showed that the increase in transmitter power for further range is limited. The radar range can be extended additionally by lower receiver noise.

The radar range can be estimated using the radar equation along with the attenuation parameter α (Equation (2.12)). Unfortunately the ground materials parameters cannot easily be measured for every location. Therefore, in most cases, an exact model cannot be given and sometimes only GPR measurements show if radar measurements are suitable for a certain location.

Each of the different radar systems have distinct properties in relevant areas of borehole radar applications. An advantage of these differences can be taken when the transmitter and receiver have multiple technologies implemented.

Such a combination and flexible solution brings benefits. Moreover, an adaptable receiver serves as basis for further research in the field. One example are radar technologies with lower mean power which in turn lead to lower average energy consumptions and longer measurement time with one set of batteries. On the other hand a measurement system configured for higher transmitter mean power can achieve a farther radar range or faster measurement times.

These options can be achieved with a versatile radar receiver to handle a pulse radar system with a high dynamic range as well as enough memory to record long signal sequences for measurements in the frequency domain or with cross-correlation methods.

The antenna size has its limits due to the borehole boundaries. Nevertheless the antennas should have a high sensitivity in radial direction and at the same time low sensitivity along the borehole to suppress the strong direct signal from the transmitter. This leads to better signal quality as research has shown [34].

The echoes are received from multiple directions around the borehole with varying levels. It is an advantage to be able to estimate the directions of the reflectors. The directional characteristics is achieved by combining multiple channels. These different antennas are connected to separate input channels. The receiver needs sufficient input channels to connect to the antennas.

Beside the physical constraints, the borehole radar system has to be simple to use in the field. Therefore the system design has to consider the requirements of operators of the equipment as it will be reviewed next.

3

System Overview

The system overview discusses the system design for a borehole probe and develops the design along the technical constraints. Further specific details and background information on certain design aspects follow in the next chapter.

As previously shown in chapter 2, there are many parameters and factors to consider for a borehole radar system. As an example, the decision for one center frequency or only one radar technology is difficult. An advanced system keeps the receiver flexible and adaptable as much as possible.

The most demanding radar technology is the pulse radar system. It requires high dynamic range and high bandwidth with a low noise figure. Unfortunately, noise increases with higher bandwidth. As an example, we consider thermal noise. The power spectral density of thermal noise - also referred to as Johnson-Nyquist noise - can be calculated for a resistor R with the Boltzman's constant k_B and temperature T in Kelvin. Equation (3.1) represents a white noise.

$$\overline{v}_n^2 = 4 \cdot k_B \cdot T \cdot R \tag{3.1}$$

The noise v_n for a given bandwidth Δf can be calculated, then, as:

$$v_n = \overline{v}_n \cdot \sqrt{\Delta f} \tag{3.2}$$

Equation 3.2 shows that the noise is significantly higher for higher bandwidths Δf as in pulse radar systems.

The results of the radar measurements, evaluated by geologists, are mostly recorded in the time domain with a pulse radar. As a consequence, first measurement results can be evaluated using the raw data. In cases where other radar technologies are used, the measured signals are often transformed to an equivalent of a pulse radar to be able to detect echoes of reflectors in the time domain.

The high requirements in sensitivity and relative simple evaluation of a pulse radar system makes it a good choice of technology for designing the initial directional borehole radar receiver.

We can distinguish three areas which affect the decisions for the overall receiver design:

1. General performance requirements
2. Electronic components and processes
3. Mechanical structure

The general requirements are items which affect the overall receiver system. More specific design goals are are mainly determined by operators of such a system.

The next point shows the components and processes needed for a radar receiver, like the antenna and data processing where some aspects are picked for further research. The last area for the design is the mechanical structure for the borehole radar. The structure is primarily determined by the borehole dimensions, whereas several options can be given on how to distribute needed components and processes. These three main areas are discussed below.

3.1 Application Specification and Performance Requirements

The design goals of the measurement system consist of constraints of the specific application and the mandatory performance specified by the project. Beyond these goals is the scientific research to add valuable practical knowledge to the field of ground penetrating radar.

Conducting borehole radar measurements involves preparation of boreholes and a derrick, or push rods. The more boreholes are involved the more time consuming and more expensive it gets. Therefore a directional borehole system will be designed which can be used with one borehole to get a three-dimensional view of the surrounding area around the borehole.

One of its main goals is a far range, where a clear radar image around the borehole can be constructed. Although the radar range has its limits due to various parameters they should not be limited by missing data storage capacity. Consequently an ambitious goal needs to be set for the radar range during the design analysis. The goal of this design is to receive echoes in a distance of up to $l = 600\ m$ (2000 ft) in dry salt. With an average speed of $v = 0.13\ \frac{m}{\mathrm{nsec}}$ we need a minimum recording time T_{MR} of:

$$T_{\mathrm{MR}} = 2 \cdot \frac{l}{v} = 2 \cdot \frac{600\ m}{0.13\ \frac{m}{\mathrm{nsec}}} = 9.2\ \mu\mathrm{sec} \tag{3.3}$$

The echoes are recorded in distinct positions along the borehole. These measurements are conducted over several hours and sometimes even days or weeks. Therefore it is vital that a battery-powered probe can be operated with one set of batteries for as long as possible. A minimum of ten hours is required for efficient operation, because changing batteries can be quite a challenge when the borehole probe is, for instance, lowered more than 1000 m and the measurement is to be conducted as low as 1500 m. Such a battery replacement will cost several working hours.

The fundamental measurement related borehole radar performance parameters consist of the penetration depth and spatial resolution. These properties can be determined when analyzing measurement data recorded in a known environment. Different measurement techniques can be used to trade the accuracy of one performance parameter with another one as shown before.

Previously different radar technologies were discussed and compared. The comparison shows that each technique has its advantages and disadvantages. Therefore the design of the receiver needs to be suited for different radar techniques. With the flexibility to choose the radar technique, the operator can select the best suitable radar technique for the measurement task. Such a feature has to be incorporated into the receiver design.

This borehole radar design focuses on a pulse radar system. The background on choosing a suitable mid-frequency are the fundamentals of the electromagnetic wave propagation in soil. As shown in the last chapter, a compromise between resolution and radar range has to be made. In this application a receiver mid-frequency of 50 MHz was selected. The bandwidth averages about the antenna mid-frequency although the bandwidth should be higher to allow for more flexibility.

The required dynamic range of the receiver depends on the technology used. The upper limit of the antenna signal is the direct signal from the transmitter, whereas the lower limit of the dynamic range is the noise of the first amplifier. A pulse radar system range can be improved by increasing the transmitter power, which in turn, requires a higher dynamic range because of a stronger direct signal from the transmitter.

The direct signal from the transmitter depends, among others, on the distance between receiver and transmitter and is assumed to be 20 dBm. This power can be estimated by using the radar equation adapted to the case of the direct signal.

The lower limit of the dynamic range is defined by the noise floor of the input channel. The actual thermal antenna noise can be calculated with equations (3.1) and (3.2) with roughly estimated system parameters. Assuming an effective antenna impedance magnitude of 1 Ω, a bandwidth Δf = 100 MHz and a temperature of T = 300 K the expected white noise can be calculated as in Equation (3.4).

$$v_{n1} = \sqrt{4 \cdot 1.38 \cdot 10^{-23} \cdot 300\ \mathrm{K} \cdot 1\ \Omega \cdot 100\ \mathrm{MHz}} = 1.3\ \mu\mathrm{V} \tag{3.4}$$

The input referred noise of an amplifier can be assumed with 3 $\mathrm{nV}/\sqrt{\mathrm{Hz}}$ [35] at a bandwidth of 100 MHz which results in a total noise voltage of

$$v_{n2} = 3\ \frac{\mathrm{nV}}{\sqrt{\mathrm{Hz}}} \cdot \sqrt{100\ \mathrm{MHz}} = 30\ \mu\mathrm{V} \tag{3.5}$$

The result shows that the amplifier noise clearly dominates. The calculated noise voltage can be converted to a noise power measured in dBm at a resistor of 50 Ω with the next equation.

$$v_{n,\mathrm{dBm}} = 10 \cdot \log \frac{v_{n2}^2}{50\ \Omega} = -107\ \mathrm{dBm} \tag{3.6}$$

The above assumptions and calculations show that the dynamic range covering the direct signal with 20 dBm down to the noise level of -107 dBm can be assumed to be in an order of magnitude of 127 dB.

The sensitivity of the radar receiver is limit by the noise power present at the antenna feed-point. Above the Earth surface cosmic noise, terrestrial radio stations or other transmitters create a noisy environment for a radar system. Fortunately, the noise of the environment is in this application very low, because electro-magnetic waves are highly attenuated by subsurface materials. As a result the receiver electronics sets the noise limits instead of the environment as the case with other radar systems. Therefore a goal is to design the radar receiver for lowest possible noise.

The requirements mentioned so far will be incorporated into the design analysis and also the design itself. Within the mechanical and electrical limits it is our goal to achieve high signal quality. The signal quality can be expressed, for example, in sensitivity and channel matching for direction estimation. These parameters rely on the components and processes used to acquire the radar echoes which will be examined in the following.

3.2 Electronic Components and Processes

The borehole radar receiver consists of several components and processes. These basic items illustrate the internal receiver signal path in Figure 3.1.

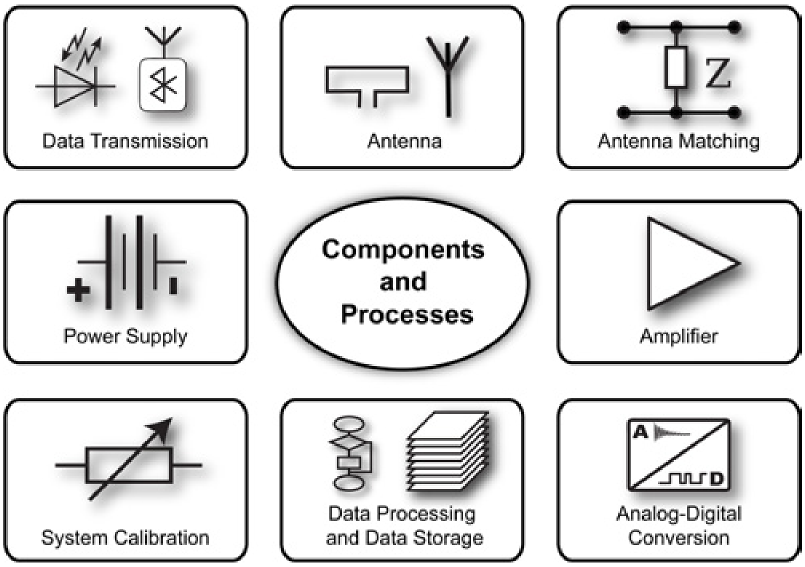

Figure 3.1: Components and processes of a borehole radar receiver.

The reflected radar echo is received by the antenna. The antenna is connected to an antenna matching circuit. This circuit can change the antenna properties within certain limits. The matching network couples the antenna to the amplifier. A variable amplifier is connected to the digitalization component. The signal digitalization involves the analog-todigital data converter as well as a timing critical synchronisation of the radar transmitter making the digitalization a complex component. After digitalization there is further data processing and storage needed. Additional vital components, among others, are an on-board calibration unit, power supply and reliable data transmission.

Now we are going to discuss the components and processes needed for a borehole radar receiver more in detail.

3.2.1 Antenna Design for Directional Borehole Radars

Direction estimation of the incoming echoes can be accomplished by using one dipole antenna and two loop antennas [26; 27]. The receiving characteristics of the loop antennas are shown together with the antenna structure in Figure 3.2. The additional dipole antenna has omni-directional characteristics which can be used to detect the correct quadrant of the receiving loop antennas.

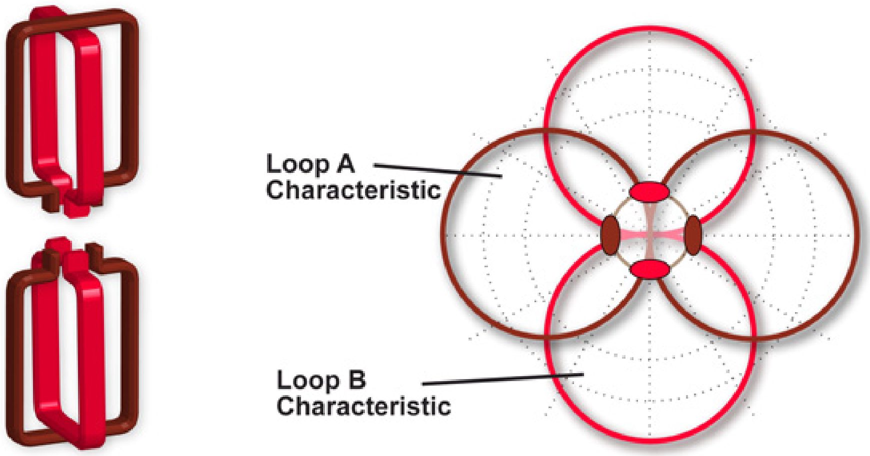

Figure 3.2: Receiver antenna principle and reception characteristics.

The received signal level depends on the dimension of the antenna, signal strength and wave length of the signal. The incoming wave causes a current in each of the perpendicular wires. These two currents are subtracted in the antenna where a higher phase difference of the two currents increases the signal level. Unfortunately, the size of the loop antennas is limited due to limited available space in a borehole radar receiver. The wave length can be calculated in general with, the following:

$$\lambda = \frac{c_0}{f} \cdot \frac{1}{\sqrt{\mu_r \cdot \epsilon_r}} \tag{3.7}$$

As an example, a wavelength for a signal frequency $f = 50$ MHz inside dry salt ($\mu_r = 1$ and $\epsilon_r = 5.9$) can be calculated with Equation (3.7):

$$\lambda = \frac{299792458\ \frac{m}{s}}{50\ \text{MHz}} \cdot \frac{1}{\sqrt{5.9}} = 2.47\ m \tag{3.8}$$

The maximum loop antenna diameter is only 0.1 m which corresponds to 4% of the signal wavelength, resulting in low sensitivity. An improvement in sensitivity is achieved by using modified loop antennas with long open loop antennas. Moreover, research has shown the effects of the strong direct signal from the transmitter to the receiver. It causes distortion of received echoes [34]. The signal quality can be improved by building an antenna which suppresses the direct signal along the borehole. The antenna design is a field for further extensive research including field simulations and is therefore not included in the receiver design.

3.2.2 Antenna Feed-Point and Antenna Adaption

The source impedance of the antenna varies with the surrounding media. Additionally higher efficiency and greater flexibility is possible by using a passive network at the antenna feed-point to modify the antenna properties. An adaption network can, for instance, change the bandwidth or mid-frequency. These features are important for different radar technologies as described in section 2.4. The design of such an adaption and its location are analyzed in the next chapter.

3.2.3 Signal Amplification

An amplifier is needed to adjust the signal level coming from the antenna. It requires careful selection to be suitable for this radar application. One important factor is a fast recovery time after overmodulation to minimize invalid measurement data.

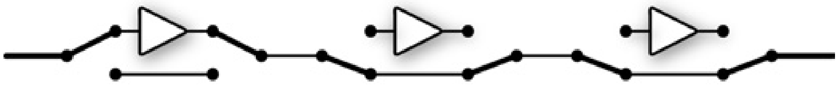

Figure 3.3: Series amplifier configuration.

There is a choice between fixed gain amplifiers and variable gain amplifiers. Fixed gain amplifiers can be switched to implement different gain settings as shown in Figure 3.4 and 3.3, whereas variable gain amplifiers (VGA) (as depicted in Figure 3.5) can be controlled by electrical continuous signals.

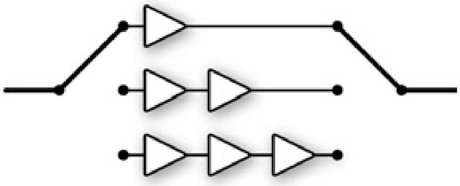

Figure 3.4: Parallel amplifier configuration.

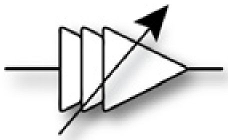

Figure 3.5: Variable gain amplifier.

Today's commercially available integrated amplifiers (e.g. AD8332 [35] or AD8099) are well suited for this application, as shown in a research conducted at the University of Wuppertal [36]. The research showed that the use of an variable gain amplifier has benefits for the application. Therefore there is no further in-depth research for this component required.

3.2.4 Analog-to-Digital Conversion

For data-processing, the incoming radar echo is converted from an analog-signal to a digital signal for further processing.

The center frequency of the radar system to be designed at first is below 100 MHz whereas the analog front-end of the receiver can process signals with an upper limit of spectral components of up to 200 MHz. According to the Nyquist-Shannon theorem, at least twice of the highest signal frequency is required to be used as sampling rate in order for the digital signal to be completely determined. Although this is true in practical applications the factor should be at least two-and-a-half. Consequently a sampling rate with a minimum of 500 MSPS is required for this radar receiver.

It is an advantage if the dynamic range of the ADC would be equal to the system dynamic performance. For instance, a dynamic range of 120 dB results in an ADC resolution of almost 20 bits.

Although the commercially available integrated circuits are improving every year the requirements in this design are not completely met by such standard components available today. Moreover, the digitalization involves synchronization of the receiver ADC components and the transmitter module. Therefore the options for the analog-to-digital conversion process need to be analyzed in detail.

3.2.5 Data Storage and Data Processing

The receiver system has limited energy capacity and limited processing power. Therefore the storage and processing of the received radar signals should be done preferably in the operator's computer.

The advantage of doing the data processing in a computer allows for direct visualization and different software packages to be used. This enables the operator to evaluate the measured data on the spot and parameters like measurement positions can be adjusted accordingly while the probe is inside the borehole.

Data processing outside the borehole probe requires high speed data transmission in order to keep the measurement time to a minimum. Today there are technologies for long distance high speed data transmission as the following section explains.

3.2.6 Data Transmission Over Borehole Cables

The connection to the borehole probe is essential for the qualified operator to adjust settings according to the measurement environment at any time. This online monitoring ensures correct operation, otherwise a complete measurement session can be conducted with wrong parameters which cause low measurement quality.

The probe is connected to the control station by a borehole logging cable with a length of several kilometers. Data transmission on these cables is challenging because most of the borehole wireline cables are unsuitable for data rates of more than a few kilobits per second due to their design.

The control and most of the data processing is done by a computer connected to the borehole cable. Therefore a reliable data transmission is required with an adequate data rate. A similar situation for high data rates and long transmission lines exists when standard telephone cables are used for high speed Internet connections with speeds of one MBit/sec and more.

The telephone cable is electrically better than some borehole cables as shown in a research project conducted at the university of Wuppertal [37]. This project examined the parameters of one specific borehole cable with a length of 1800

m. It was shown that the cable has high crosstalk and high attenuation for frequencies above 100 kHz. Therefore standard SDSL (Synchronous Digital Subscriber Line) modems were tested for data transmission. The achieved data transmission speed was more than 1.8 MBit/sec for a two wire connection and almost double the rate was reached with a four wire link over the same cable.

Field tests at the university of Wuppertal showed that commercially available DSL technology with discrete multi-tone modulation (DMT) or orthogonal frequency-division multiplexing (OFDM) can be used for high speed data transmission over electrically low-grade long borehole cables.

3.2.7 Calibration

Borehole radar systems are exposed to harsh environments. For instance, some boreholes are filled with liquids and temperatures that vary from extreme low up to extreme hot temperatures. Consequently, calibration is needed to minimize external influences and internal inaccuracies in the borehole radar receiver. One example for internal calibration are the antenna input channels which have to match for adequate directional resolution.

The external temperature is increasing under the subsurface of the earth depending on the location. The geothermal gradient varies highly depending on the location, whereas the average of a large area or region mostly has a gradient of below 10°C per 100 m. The variation within a few kilometers can be from below 2.5°C per 100 m up to more than 50°C per 100 m as the geothermal data for the state Utah, USA showed [38].

Correct system operation in all environments and environmental conditions is vital. Therefore calibration is an important process to ensure and correct system parameters. This process along with its components is examined in detail in the next chapter.

3.2.8 Power Supply

The radar electronics needs a reliable power source which can be used in the required temperature range. One source of energy can be provided by borehole logging cable connection. In cases where this is not possible, batteries can be used. There is the choice between rechargeable and non-rechargeable technologies. A suitable battery type with high capacities are, for example, non rechargeable batteries based on Lithium-Ion (e.g. [39]).

The supplied incoming voltage has to be converted to several local voltages. Switched power supplies provide flexible input voltages and very efficient voltage conversion. Such devices give more options for the power supply design. On the other hand, these switched voltage converters produce additional noise. Therefore switched power supplies have to be avoided to ensure that no extra noise is introduced into the sensitive measurement electronics.

3.3 Mechanical Probe Structure

The environment of mines and construction sites require a rugged mechanical design for the borehole probe. The boreholes where the probe is inserted are often used to take material probes. The smaller the diameter of these boreholes the faster is the drilling process. Therefore mines sometime drill holes with only 48 mm respectively 38 mm in diameter [23]. At the same time bigger boreholes allow for larger antennas with better sensitivity. The probe to be designed will be used in boreholes with a diameter down to 100 mm (3.9 in). Within these limits the mechanical structure must ensure that the sensitive electronics is well protected inside its body.

That means that the probe body has to withstand shocks which can occur when the probe is connected to a cable winch. Additionally it is planned to use the probe in liquid filled boreholes and therefore the mechanical design has to be water tight to withstand high pressure. For instance, the probe can be lowered down to 1000 m in a water filled borehole when the mechanical structure can withstand a pressure of 10 MPa (100 bar or 1450 psi). This needs to be considered when designing the structure of the borehole radar system.

There are several options for the mechanical structure of the borehole radar receiver. The structure affects the electronic design and the radar receiver performance. The most simple design would be a receiver consisting of two loop antennas and one dipole antenna in one module with a long borehole logging cable connected to a data acquisition module in a computer. The other extreme is a compact transient recorder including internal storage memory in the same module as the antennas with no need to have any electrical connection to the outside. Both design approaches have their advantages and disadvantages.

The length of the antenna cable connection is limited by the cable attenuation. Therefore a module with electronics has to translate the low level antenna signal before transmitting the signals over the long borehole cable. Moreover, there are more limiting factors for a cable connection at the antenna feed-point as it will be explained in detail later on.

The option to build an independent transient recorder as a receiver doesn't rely on any data transmission. This avoids the need of a sophisticated data transmission over the borehole logging cable. On the other hand, there would be no monitoring or control of the probe possible without a cable connection during measurements. In this case there is no option to evaluate data or change measurement options during the measurement. However, this design option cannot be used because the receiver is supposed to be flexible in parameters and radar methods which can be selected during the measurement campaign. Therefore the receiving antenna has to have a data acquisition unit connected within a short distance, which is in turn connected to a borehole wireline logging cable.

The direct signal of a pulse radar transmitter is very strong and can over-modulate the receiver, which makes it impossible to receive weak antenna signals for a certain amount of time. Therefore the transmitter has to be located at a well defined distance from the receiver. Furthermore, the antenna coupling is reduced in a bistatic radar system and it is possible to use different receiver and transmitter combinations.

Considering the design options mentioned before, the radar system will have a relatively long length. Consequently, a modular design for the borehole radar system is required for transportability.

Figure 3.6: Radar probe.

3.4 Modular Borehole Radar System

The terrain, which includes underground tunnels, where the probe is used is often difficult to reach. Therefore the probe is divided into several separate modules for easier transportation. Transportation includes trucks, manual carrying and cages in a mine shaft. Several mechanical modules can be used to provide space for a transmitter, receiver, control module and spacer modules.

Module	**Length**	
Control Module	1 m	3.3 ft
Distance Control-Receiver Module	6 m	19.7 ft
Receiver Module	3 m	9.8 ft
Distance Receiver-Transmitter Module	6 m	19.7 ft
Transmitter Module	2 m	6.6 ft
Total Length	**18 m**	**59 ft**

Table 3.1: Approximate probe dimensions.

The modules are connected tightly together with cap nuts. All three main modules are shown in Figure 3.6. The bottom of the probe is the transmitter. A few meters above is where the receiving antenna is located. The top part is the control module which communicates with the receiver electronics and the control station. The transmitter and receiver have to be some meters apart to avoid strong direct transmitting signals on the receiver side. This structure provides a good starting point for a borehole radar system design. The following table 3.1 lists the possible lengths of these modules.

3.5 Borehole Radar Receiver Components for Further Research

The system analysis shows that some components are commercially readily available whereas other components and processes require further research.

At first, the antenna feed-point has to be analyzed and designed for changing the antenna properties. This involves the connection to the digitalization unit and is therefore subject to further investigation in the next chapter.

The analog-digital-conversion process includes not only the ADC components itself. Moreover, the transmitter as well as additional digital circuitry are necessary for the conversion process. Among other critical factors is the synchronization between transmitter and analog-to-digital converters.

Another important point for further research is the signal quality which relies among other parameters on the signal digitalization process. Methods and parameters affecting the signal quality have to be defined. Adequate test signals can determine the signal quality. Also, such test data is suitable for calibration. Such knowledge about the receiver system makes it possible to improve the measurement results by calibrating the measurement data. The needed processes and components are investigated and evaluated in the next chapter.

4

System Analysis and Design

The radar receiver consists of many components, nevertheless three components can be considered as core parts. The first core part is the matching network connected to the antennas. The next important component is the digitalization which is connected to the antenna feed-point by a special matching network. The calibration unit is another core element of this receiver design to ensure reliable operation and calibrate the receiver for accurate results. Additionally calibration data can correct recorded measurement results before data analysis. These three modules are depicted in Figure 4.1.

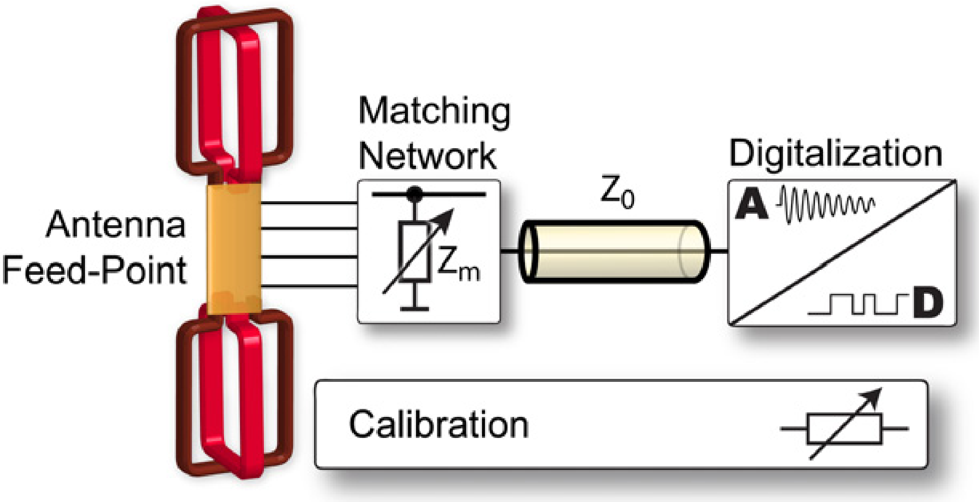

Figure 4.1: Core components of the borehole radar receiver.

The location of these core components along with its suitable type of connection are analyzed. It is important that these core parts themselves individually are designed for the specific task in a borehole radar system. In the following these three particular receiver system components are analyzed and a design is developed.

4.1 Antenna Connection and Antenna Adaption

At the antenna feed-point leads connect the antenna with the receiver electronics. These cables can vary from very short lengths to rather distant long cables. In the case of the borehole radar receiver design one option is to place all receiver components into the control module. It is directly connected to the borehole logging cable providing power and a reliable communication link. This setup would require a cable length of several meters to connect the electronics with the antennas.

The connection of the antenna feed and the receiver electronics must be carefully designed to avoid any reflections on the electrical cable. An electrically mismatched connection causes reflexions which appear as 'ghost echoes' in the radar data. Even small reflexions on the electrical connection can be detected with sensitive receiver electronics.

Another point to consider is the sensitivity of the antennas to avoid any unintended changes in their electro-magnetic structure. One of these changes is, for instance, caused by nearby conductive cables. Another factor is that the antenna properties can vary with the surrounding material. In a borehole the surrounding properties, including the moisture, can change over the length of the borehole.

4.1.1 Antenna Matching Network

A borehole radar system is used in different surrounding media and radar targets vary with the application. While the radar environment is changing, the antennas remain the same. Therefore it is an advantage to adapt the antennas to the specific measurement task. Moreover, such an antenna matching is able to modify the antennas properties for different radar technologies.

The tunable antenna properties are the resonant frequency and bandwidth. This means for example that it is possible to focus on far range measurement with narrow bandwidth or achieve broadband reception. Another application is to adapt the resonant frequency of the antenna to the transmitter in different surrounding media where resonant frequencies change.

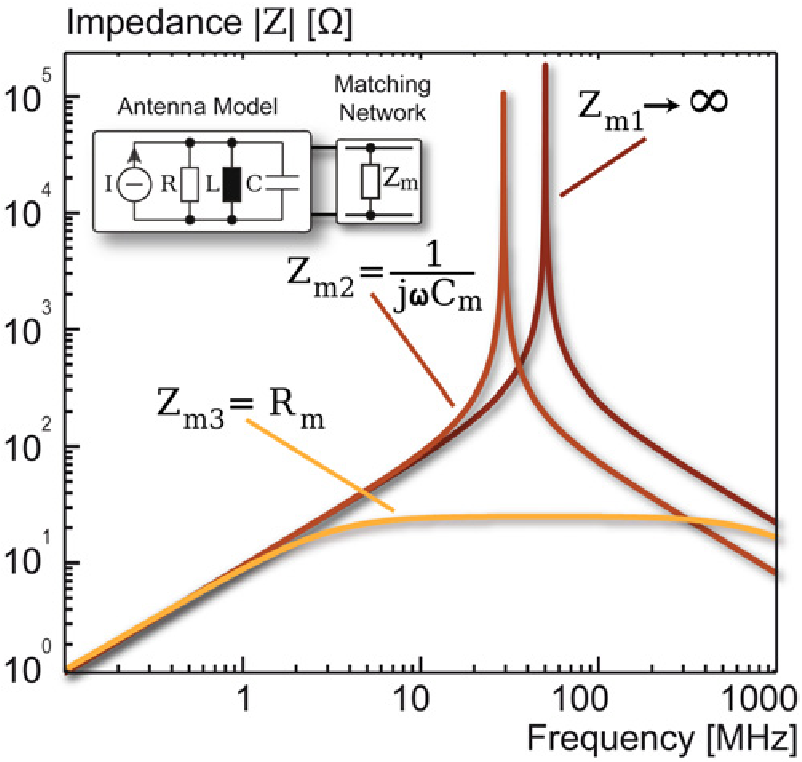

Figure 4.2: Varying antenna impedances for different connected matching networks: $C_m = 20$ pF, $R_m = 20\ \Omega$.

The antenna can be modeled as a parallel resonant circuit with a specific impedance Z_{Ant} where the impedance of the antenna shows its characteristics including the bandwidth. When a parallel resonant circuit is loaded with a resistor Z_{m3}, the impedance is lowered and the bandwidth broadens as shown in Figure 4.2. On the other hand the resonance frequency changes when a capacitance is connected as in the case of Z_{m2}.

The graphs in Figure 4.2 prove that an antenna matching network can effectively change the antenna properties. In the following sub-sections, the location and the connection of the matching network are analyzed.

4.1.2 Influence of Conductive Cables on the Antenna

Conductive cables connecting the antenna feed to components in a distance away of the antenna, as in the case of the control module, are forced to run close to the antennas due to space limitations. This case is illustrated in Figure 4.3 where the modules are separated in an order of several meters. These conductive cables influence the antenna characteristic because of the proximity to the antenna conductors.

These conductors can be placed inside the antenna structure without harming the antenna characteristics when the conductors are placed totally symmetrically. Although a misplacement of just a few millimeters changes the antenna radiation pattern already.

Measurement errors are caused by electrical coupling between the receiving antennas and conductive cables. The direct signal of the transmitter and the back scattered echoes induce electrical currents on the conductive cable. Such a cable wave guide is relatively long compared to the nearby relative short receiving antennas. Additional 'ghost' echoes are caused by cable mismatches. As a result, the coupling causes signal distortion and errors in the directional receiving pattern.

A research study, among others, was presented in the paper “Recognition of borehole radar cable related effects using variable offset sounding” [40]. The authors show that the induced currents on a cable are detected by the receiving antennas and “periodic artifacts can be introduced into data as a result of partial reflections that can occur in cables at system impedance mismatches.”.

Figure 4.3: Antenna with coax cable connections.

4.1.3 Cable Influences on Antenna Adaption Circuit

A parallel resonant circuit is a simplified model of the antenna feed-point. It helps to understand the electrical influence of a connected coaxial cable. In cases where the wave lengths of the transmitted signals are in the order of the cable length, the cable has to be treated as a transmission line. In fact, impedance matching at inter-connections becomes important. A rule of thumb says that an electrical cable connection with a length of less than a tenth of the shortest wavelength has an insignificant effect on the signal transmission.

The principle block diagram for an electrical long transmission line connected to the antenna feed point is shown in Figure 4.4. The connected antenna sees the input impedance Z_1 of the transmission line. Z_0 is the impedance of the transmission line whereas Z_m represents the antenna impedance matching network combined with the amplifier input impedance.

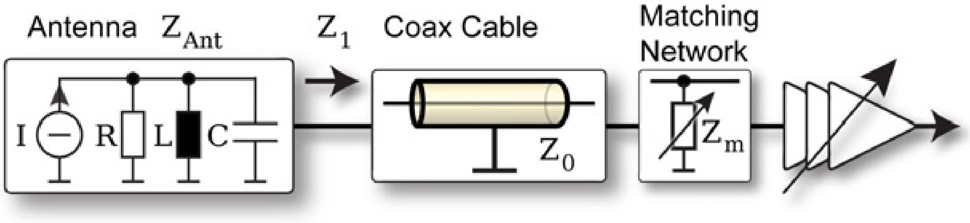

Figure 4.4: Antenna connected to the matching network by a transmission line.

The resulting impedance Z_1 in Figure 4.4 is the impedance the antenna sees at the feed-point. This impedance influences the antenna properties and is used for antenna adaption. The impedance Z_1 is the transformed impedance of the matching network Z_m. This effective impedance Z_1 seen by the antenna can be calculated for a simplified lossless transmission line with a length of l_0 with Equation (4.1).

$$Z_1 = Z_0 \cdot \frac{Z_m + jZ_0 \cdot \tan\left(2\pi \frac{l_0}{\lambda}\right)}{Z_0 + jZ_m \cdot \tan\left(2\pi \frac{l_0}{\lambda}\right)} \tag{4.1}$$

The signal wavelength λ in a specific cable, characterized by a velocity factor vf, is calculated with the speed of light c_0 and signal frequency f.

$$\lambda = \frac{c_0}{f} \cdot \mathrm{vf} \tag{4.2}$$

In order to dampen the antenna to achieve a higher bandwidth, a resistor can be used. This resistor needs to be effective for the desired bandwidth, at the antenna feed, resulting in a Z_1 with no imaginary component. In particular, the imaginary part of Equation (4.1) must be zero for the relevant frequency range. The parameters Z_0 and Z_m are non zero. Therefore the term $\tan\left(2\pi\frac{l_0}{\lambda}\right)$ contains parameters influencing the result. It can be seen that this tangent function only equals zero on a zero function parameter. In all other cases it converges to zero on short cable lengths l_0 or low frequencies which result in long wavelengths λ.

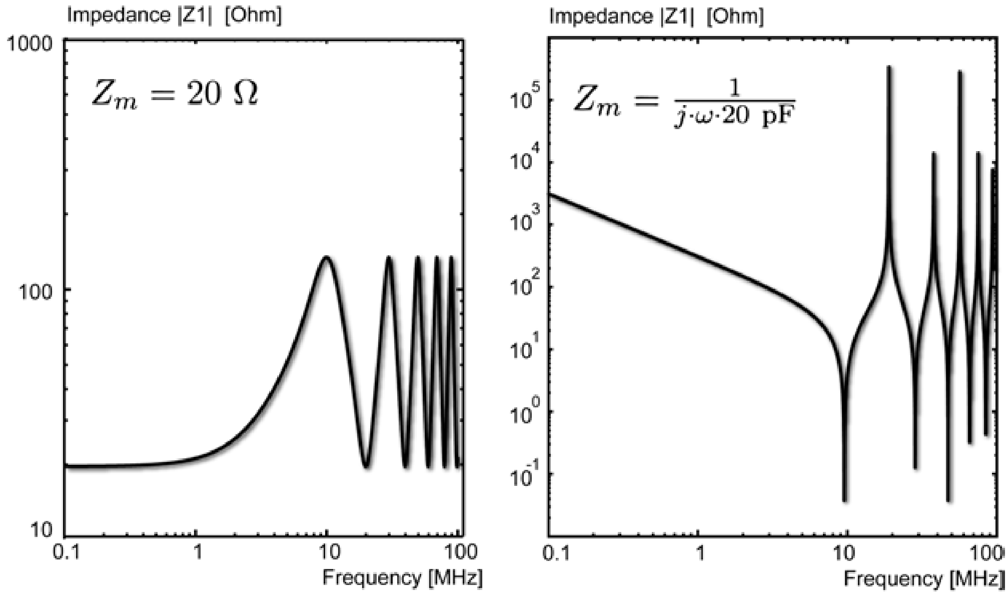

Figure 4.5: Input impedances Z_1 for $l_0 = 5\ m$ and $Z_0 = 50\ \Omega$.

The example in Figure 4.5 shows the input impedance characteristics $|Z_1|$ for a resistor (right graph) and a capacitor (left graph) as a matching network Z_m for frequencies from 100 kHz up to 100 MHz. It can be seen that for low frequencies the input impedance $|Z_1|$ equals the matching impedance. For higher frequencies the transformed input impedance $|Z_1|$ is highly non-uniform.

The signal transmission has to be uniform and must not produce any distortion due to non-uniform impedances. In particular, we can conclude that there must be no cable longer than approximately $\lambda/10$ between the antenna and the antenna adaption network. Assuming an upper limit signal frequency of 200 MHz, the resulting maximum cable length is:

$$\frac{\lambda}{10} = \frac{c_0}{f} \cdot \frac{\mathrm{vf}}{10} = \frac{299792458\ \frac{m}{s}}{200\ \mathrm{MHz}} \cdot \frac{0.66}{10} \approx 0.1\ m \tag{4.3}$$

As a consequence, it is important to connect the antenna matching network close to the antenna feed point and not to exceed a cable length of 0.1 m.

4.1.4 Antenna Feed-Point Link to Digitalization Unit for Active Antenna Adaption

The previous sections showed that conductive cables act like receiving dipoles where radar echoes induce electrical currents. These currents are detected by the receiver antenna and cause so called “ghost echoes”. As a consequence, it is important to prevent antenna disturbance by avoiding conductive cables. Furthermore, the antenna matching network has to be located close to the antenna feed-point in order that the connected matching network to be effective.

These requirements suggest to connect the matching network at the antenna-feed point with an optical link or non-interfering wireless link to the digitalization unit. The following sections discuss practical solutions in regard to these requirements. Two optical options are presented below

4.1.5 Optical Electric Field Sensor

Optical electric field sensors can be used to transmit the antenna signals by optical fibers using only the antenna signal. There is no external power supply needed. A polarized optical wave is transmitted by a laser diode over an optical fiber to the optical electrical field sensor. The received antenna voltage at the sensor modulates the passing optical wave. Figure 4.6 illustrates the principle. There are various systems commercially available. One of these commercial systems connects directional radar antennas to a network analyzer in a borehole probe research project [16].

As proposed earlier, antenna adaption is required for our application. The adaption network needs active electronics to switch different components. This is possible to a certain extent with an additional optical electrical field sensor using a photovoltaic cell. Such a system was presented [41] to power a local amplifier with 50 mW. Similar configurations are complex and not readily available. Another issue is impedance mismatch and reflections on the optical fiber which is partly caused by connectors.

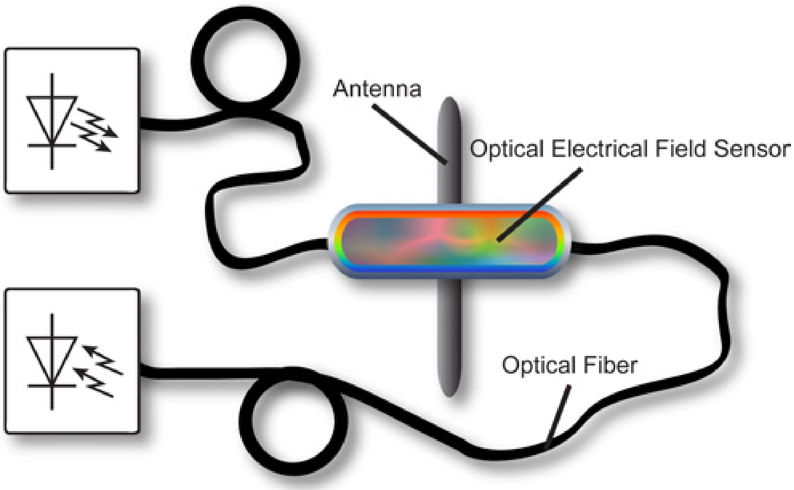

Figure 4.6: Principle of an optical electrical field sensor connected to a dipole antenna.

In general such an optical electric sensor is suited to be used in a steady state which is common in continuous wave radar systems and is therefore not suitable for a pulse radar system. An alternative option is to use electronics to convert the antenna signals and transmit the digital data by fiber optical cable.

4.1.6 Active Analog-to-Digital Conversion

Another approach to avoid conductive cables is to use optical fiber cable to transmit digitalized data from the antenna base point to the control module. Such method requires active electronics within the antenna feed point. The antenna feed is coupled to a receiver electronic with the proposed antenna matching network. Thereafter the signal is amplified and then converted from an analog to a digital signal as illustrated in Figure 4.7.

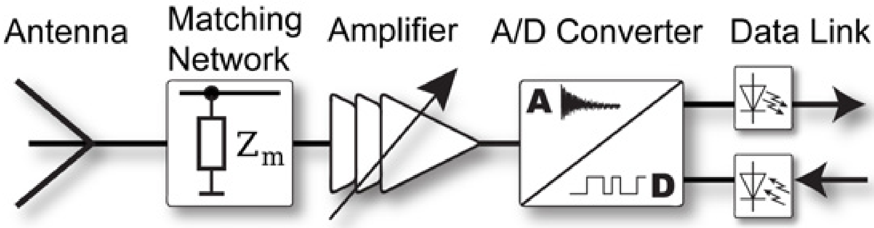

Figure 4.7: A/D converter at the antenna feed-point using a digital optical link.

The electronic circuit boards have to be located in the center of the antennas for least interference. Moreover, the switchable antenna matching network can be placed on a circuit board as close as possible to the antenna feed. A power supply by means of batteries can be placed together with the electronics. A bidirectional interface for an optical fiber can be attached to the digitalization unit. This allows for parameter configuration and data retrieval.

4.1.7 Comparison of Signal Processing Options for Optical Transmission

The previous sections analyzed the options of the antenna feed connection. The main features for an adaptable receiver can be summarized as:

1. Optical fiber connection for least antenna disturbance and no additional echoes on a conductive cable
2. Short connection to a switchable passive network for antenna adaption
3. No signal reflections on connection to digitalization module; matched cable connections

The above requirements must be met for the radar receiver. The reviewed options for the antenna feed-point are compared side by side in Table 4.1.

	Passive Optical E-Field Sensor	**Active A/D-Conversion**
Pro	+ no additional conductors + small dimensions + limited active components	+ high sensitivity + high dynamic range + variable antenna matching + bidirectional communication
Con	- low sensitivity - limited dynamic range - complex optical control electronics	- power supply needed - self induced errors possible - size

Table 4.1: Comparison of a passive optical electrical field sensor and active A/D-conversion located at the antenna feed.

The advantage of the optical electrical field sensor is the size and simplicity at the antenna feed point. Unlike the active A/D conversion option, the control electronics is rather complex. Moreover, the sensitivity and flexibility is limited and an adjustable antenna impedance matching is not possible.

Therefore it is proposed to use active electronics including A/D conversion right at the antenna feed-point in this design. Its size and the needed power supply is a drawback which is more than compensated by the increased flexibility. A high sensitivity receiver is only possible with active components at the antenna feed point. Moreover, a flexible efficient antenna adaption with a switched network is only possible when there are active electronic components available.

The next sections develop the design for such a receiver with direct signal digitalization at the antenna feed.

4.2 Signal Digitalization

The digitalization unit converts the analog signals coming from the antenna feed-point into digital signals. First the digitalization requirements are reviewed and thereafter current technologies are analyzed. Finally a signal digitalization unit for the borehole radar receiver is designed.

4.2.1 Available Analog-to-Digital Conversion Technology

As technology advances, the performance of analog-to-digital converters is constantly getting better while at the same time the power consumption decreases. Figure 4.8 gives an overview of the current technology where the box labeled "Borehole Radar Receiver" represents the application specific requirement.

The effective resolution equals the dynamic range of the converter which is less than the nominal resolution specified in bits due to internal ADC inaccuracies. One of the error sources is noise. This noise depends on different system parameters. There are several error sources like differential nonlinearity (DNL), integral nonlinearity (INL) and timing related errors. There is much literature available discussing every aspect of analog-digital conversion errors. Moreover, these parameters can not be influenced in commercially integrated circuits. Therefore these ADC specific inaccuracies are considered as not avoidable and the focus is set to the application specific issues of the borehole radar receiver.

Unfortunately, the required dynamic range, conversion speed and power consumption are not met by commercially available A/D converters today. As Illustration 4.8 shows, the effective resolution and throughput rate of the existing data converters have to be increased to have a suitable A/D converter for the application. The conversion speed can be traded for the effective resolution

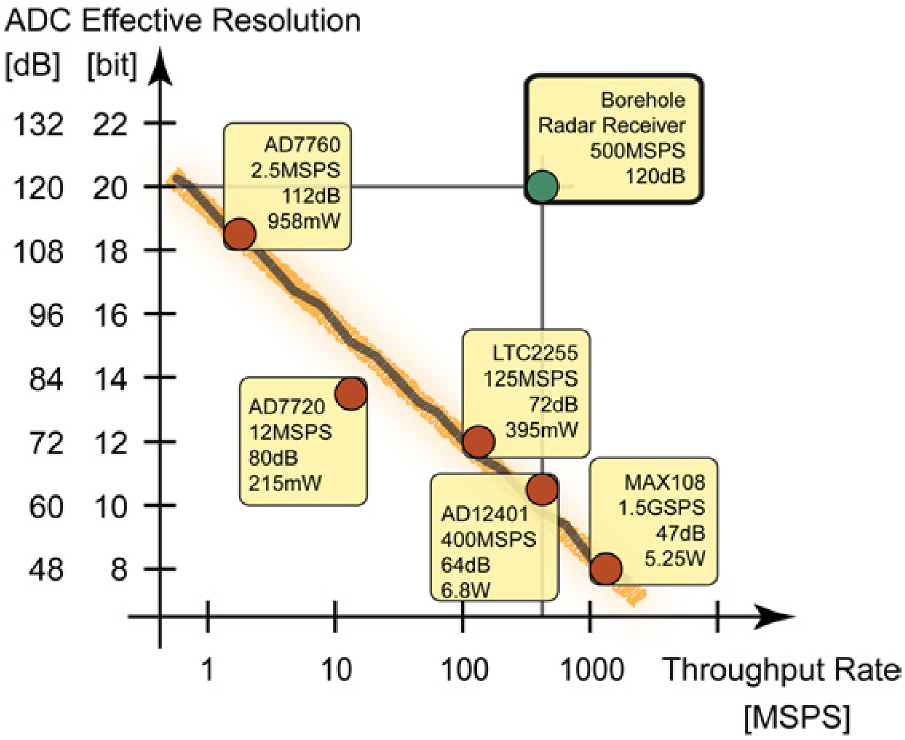

Figure 4.8: Available A/D converters as of the year 2007.

while higher conversion speeds have, unfortunately, higher power requirements. The choice of an ADC for the receiver can be expressed in numbers by calculating an application specific ADC efficiency.

$$\text{ADC Efficiency} = \frac{\text{Dynamic Range} \cdot \text{Throughput Rate}}{\text{Power Consumption}} \tag{4.4}$$

The values calculated with Equation (4.4) are higher for better suited data converters. The highest efficiencies scores can be calculated for mid-range high speed converters with 70 to 80 dB dynamic range, sampling rates from 100 MSPS to 125 MSPS and low power requirements. Such converters are therefore suited best for this borehole radar receiver.

The target conversion speed and required dynamic range can be attained when extending resolution range and throughput rate of the suitable data converter. The effective throughput speed of an A/D converter can be increased by using an interleaved sampling technique resulting in a finer time domain resolution. The dynamic range can be extended using adjustable amplifiers. These methods are widely used as, for instance, discussed in the article “Pushing the State of the Art with Multichannel A/D Converters” [42] where data averaging and time interleaving is suggested to improve noise figures of an analog-to-digital data converter system. The next sections will discuss the extension of the dynamic range while focusing on achieving high data throughput rates.

The range of the ADC can be extended by using amplifiers. Different amplifier settings can be used to attain the optimal signal level for the data converter. In the case of strong signals an attenuator might be required. These different settings result in multiple measurements for a radar system where the receiver has to cope with a high dynamic range. These variation in signal levels cause out of range errors in certain parts of the signal. Nevertheless a signal with no distortion can be created by combining different measurements.

In addition to amplifiers extending the dynamic range, data averaging is an effective method to extend the dynamic range.

4.2.2 Expansion of Dynamic Range and Noise Reduction by Averaging

Data averaging, sometimes called data stacking, improves the signal-to-noise ratio which leads to higher resolution. The principle used is that the effects of random noise is reduced through averaging, whereas in contrast systematic errors cannot be minimized in the same way. These errors are primarily synchronous to the ADC clock and other recurrent system events.

The gain G_{bits} achieved in the effective resolution by stacking with a factor of i can be calculated as in equation 4.5.

$$G_{\text{bits}} = \log_2(\sqrt{i}) \tag{4.5}$$

The above equation can be alternatively calculated in dB like in Equation (4.6).

$$G_{\text{dB}} = 20 \cdot \log_{10}(\sqrt{i}) \tag{4.6}$$

The equations show that it is beneficial to conduct multiple measurements, consequently increasing measurement time and thereby lowering random noise. On the other hand this method can only be used to a certain degree, because the resolution measured in bits increases by half a bit on every doubling of the averaging thus doubling the measurement time.

Another form of averaging is signal filtering. In fact the higher the conversion rate of the ADC is, the more data is available when filtering. A bandpass filter can be used, for instance, to remove unwanted erroneous signal frequencies.

4.2.3 Increasing an ADC Throughput Rate With Interleaved Sampling

Time interleaving of ADCs is a common concept which was introduced by Black and Hodges in 1980 [43] to increase the effective sampling rate of ADCs. There are several methods to build an interleaved sampling ADC system. One option is to use several A/D converters sampling the same signal at a time-shifted clock signal as depicted in Figure 4.9. In such a design the effective sampling speed increases with the number N of ADC converters $F_{s,\text{effective}} = N \cdot F_{s,\text{ADC}}$.

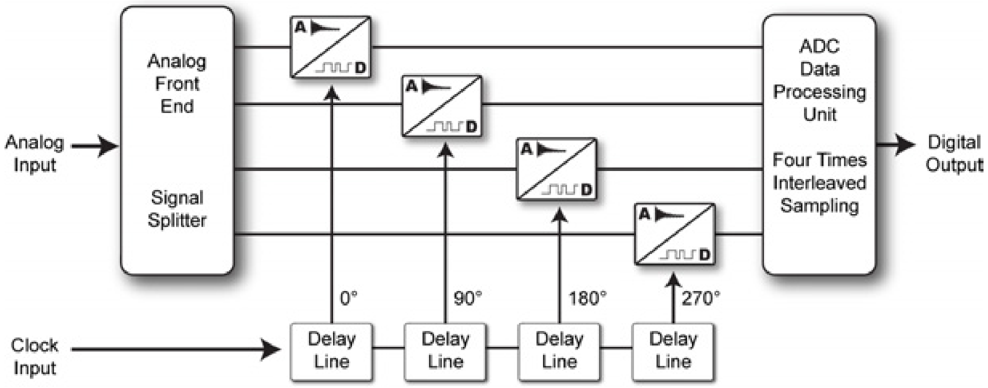

Figure 4.9: Interleaved sampling with parallel analog-to-digital conversion.

Another option is to use one ADC and to shift the ADC sampling clock relative to the input signal. This is illustrated in Figure 4.10. The shifting is done in fractions of the sampling clock up to the clock period. The borehole radar application makes it possible to shift the signal to be acquired instead. Shifting is done by shifting the transmitter trigger signal in fractions of the ADC sampling clock.

When the trigger signal of the digitalization circuit is used as an input signal a certain signal level triggers the digitalization process while the transmitter is configured for a free running self-triggered operation. The acquired samples are interleaved depending on the trigger occurrence in relation to the internal ADC clock signal. This process works only reliably with a stable direct echo from the radar transmitter. A more reliable option is to actively trigger the radar transmitter where the trigger signal is an output of the sampling circuit.

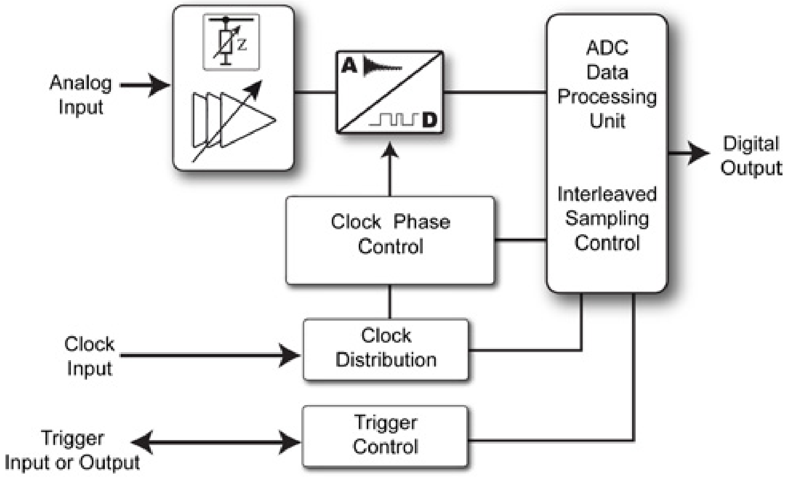

Figure 4.10: Interleaved sampling with analog-to-digital conversion in series.

The measurement task of the borehole radar receiver allows for enough time to make several repetitive measurements in the same probe position, because the radar targets are stationary. In this design it is therefore possible to shift the triggered radar pulse to build an interleaved sampling receiver with one ADC. This technique and its signals is depicted in Figure 4.11 for four times interleaved sampling. The receiver sends a trigger pulse to the radar transmitter and starts to record the antenna signals. The next trigger is shifted by 90° with reference to the sampling clock of the ADCs and the recorded signal is stored in its distinct interleaved memory location. Thereafter this process is repeated until all samples have been acquired.

The method of parallel interleaved sampling is impractical in this design due to limited space and tight power requirements.

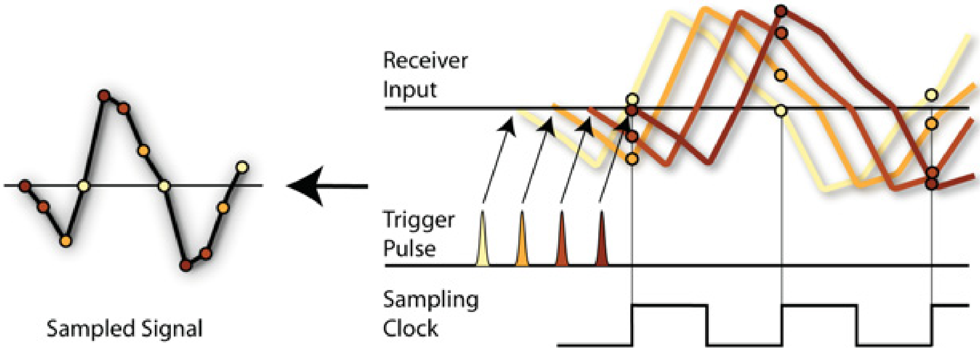

Figure 4.11: Four times interleaved sampling with a shifted trigger signal.

Regardless of the method used to build an interleaved sampling ADC receiver there are three basic error categories which result in conversion errors:

- gain mismatch - differences in gain factors
- offset mismatch - channel related offset voltage
- sample time mismatch - e.g. aperture jitter, clock jitter and transmitter uncertainties

These interleaved sampling specific errors can only be distinguished with methodical system analysis. In general, such errors can be separated into a systematic and random part. In the case of sample time errors with a Gaussian distribution such random error exists in form of a noise floor. In contrast, repeated sample time uncertainty results in systematic sampling errors.

The part of the distortion caused by systematic errors can be eliminated after proper calibration or parameter adjustment. Noise caused by random errors can be reduced by averaging techniques.

The accuracy of the interleaved sampling process is primarily determined by the timing accuracy between the ADC clock and the received radar signal. The sources of these time uncertainties will be considered next.

4.2.3.1 Sources of Time Uncertainties

We need to identify the sources of time inaccuracies to understand the effects better. After identifying the jitter sources it is possible to minimize the sampling timing uncertainties to get a better signal quality.

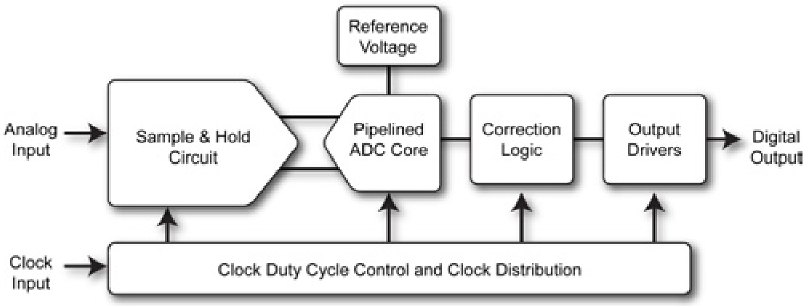

Figure 4.12: Structure of a sub-ranging A/D converter.

A block diagram of a subranging pipeline ADC helps to locate jitter sources. The sample and hold unit samples the incoming signal and stores it for a short time for further processing. This is the most critical part in regard to timing uncertainties. After this point there is more time for signal processing during the signal hold time.

There are two jitter sources affecting the sample-and-hold circuit. This circuit itself has a specific aperture jitter which is in a range of about $0.2\ \mathrm{ps}_{(\mathrm{RMS})}$ in current ADCs [44]. This jitter is caused by thermal noise in the input circuit and therefore can be modeled as independent Gaussian jitter [45]. Furthermore the input clock signal adds additional jitter.

The timing of an ADC is based on a stable clock signal. Nevertheles, the long-term and short-term stability has its limits. The short-term uncertainty is measured as cycle-to-cycle jitter or clock jitter. Another more common value is the phase noise of an oscillator which can be converted into a jitter equivalent value [46]. Commercially available crystal oscillators offer the lowest possible noise with jitter down to around 1 ps [47].

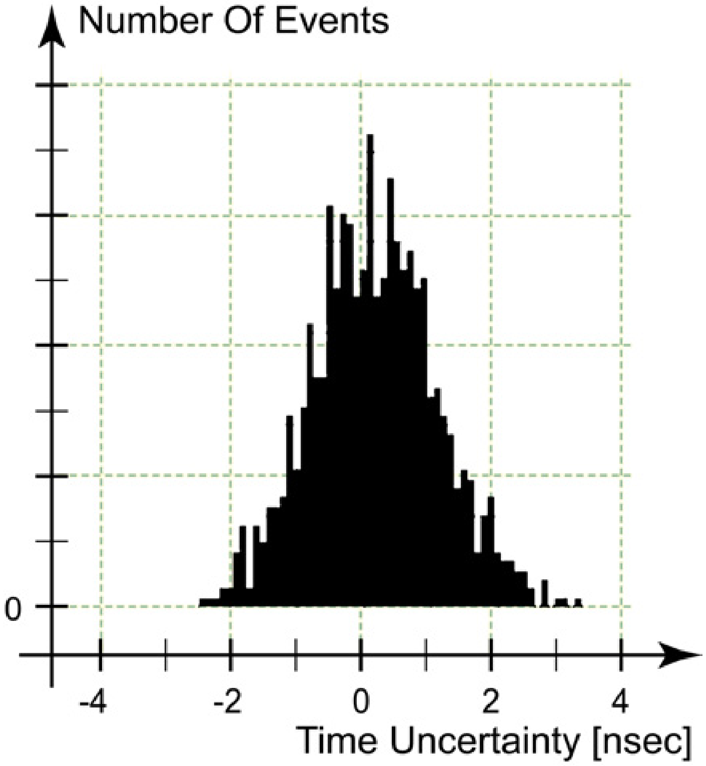

Figure 4.13: Trigger distribution of a pulse radar transmitter.

The jitter sources discussed above are the fundamental sources of time uncertainties. Additional time uncertainties can occur depending on the application. If logical gates are used in the clock path a jitter of approximately 1 ps is added when ultra-high-speed gates like 74ACT00 are used. Standard parts like 74LS00 (Δt = 4.94 ps [48]) or 74HCT00 (Δt = 2.2 ns [48]) add significantly more jitter and therefore must not be used in high-speed digital ADC circuits. Today's FPGA contain digital clock conditioning units. They are very practical when the clock frequency or phase has to be changed during circuit operation. These circuits contain logic gates and PLL logic units which add further jitter to the clock signal. When using a Xilinx FPGA digital clock manager the additional jitter is 250 ps peak-to-peak. Another option it to use a delay chain consisting of numerous logic gates inside the FPGA.

A major source of jitter in a pulse radar application is the transmitter. Most of the transmitter modules contain Avalanche transistors. In Figure 4.13 the trigger distribution of an Avalanche transmitter module was measured [49]. The result shows a trigger uncertainty of approximately 0.8 ns.

Jitter Source	**Value**	**Note**
Sample & Hold Circuit [44]	0.2 ps	RMS rated
Low Noise Clock Oscillator [47]	1 ps	RMS rated
Digital Clock Manager [50]	250 ps	peak-to-peak value
FPGA LVDS Buffer [51]	24 ps	peak-to-peak value
Pulse Radar Transmitter [49]	800 ps	RMS rated

Table 4.2: Comparison of jitter sources.

Table 4.2 lists the introduced jitter values along with their sources. The list shows that the pulse radar transmitter is a major source of time uncertainty in the digitalization process. The next sections analyze the consequences of this unavoidable high transmitter jitter when using interleaved sampling for the digitalization process. In general the timing uncertainties influence the sampling process itself. In the following sub-sections the fundamentals of the sampling are briefly explained.

4.2.4 Sampling Fundamentals

The ideal sampling process is a multiplication of the analog signal with a Dirac comb function. The resulting pulse amplitude modulation is quantized and the result is available at the output of the A/D converter. Figure 4.14 shows the process in the time and frequency domain side by side.

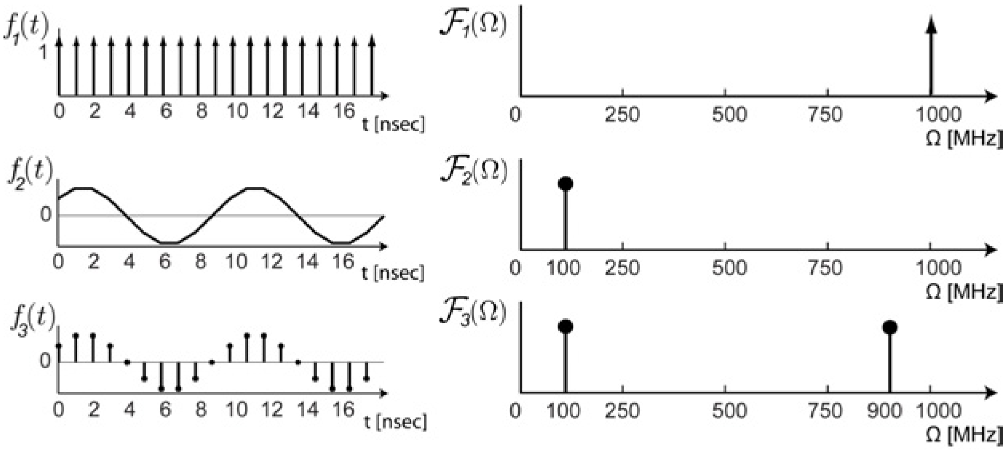

Figure 4.14: Sampling process in the time and frequency domain.

The sampling clock f_1 is multiplied with the input signal f_2. The result is a pulse amplitude modulation f_3. In the frequency domain, the signal spectrum is maintained in the resulting spectrum, and additionally, the input signal is convoluted around the sampling frequency $\mathcal{F}_1$ as in diagram $\mathcal{F}_3$.

$$f_1(t) = \sum_{n=-\infty}^{\infty} \delta(t - n \cdot T_s) \tag{4.7}$$

The sampling signal is a dirac comb function which is an infinite sequence of evenly distributed delta pulses as shown in Equation (4.7) and Figure 4.15. Some authors refer to this function as Shah function (like the cyrillic letter Shah). This function is multiplied with the input signal to produce the pulse amplitude modulated (PAM) signal for quantization.

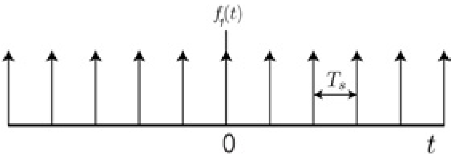

Figure 4.15: Time domain.

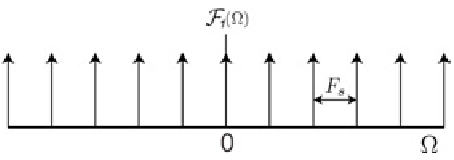

Figure 4.16: Frequency domain.

The comb function $f_1(t)$ can be transformed into the frequency domain as shown in Equation (4.8) and illustrated in Figure (4.16).

$$\mathcal{F}_1(\Omega) = \sum_{n=-\infty}^{\infty} e^{-j \cdot n \cdot T_s \cdot 2\pi\Omega} = \frac{1}{T_s} \sum_{m=-\infty}^{\infty} \delta(\Omega - m \cdot F_s) \tag{4.8}$$

$$F_s = \frac{1}{T_s} \tag{4.9}$$

In practical applications the uniform distribution of the Dirac comb function cannot be guaranteed due to jitter effects. This time uncertainty of every Dirac pulse can be modeled as ΔT_n in the time domain as shown in Equation (4.10).

$$f(t) = \sum_{n=-\infty}^{\infty} \delta(t - n \cdot T_s - \Delta T_n) \tag{4.10}$$

The consequence for the frequency domain can be calculated by using the rule for time shifted signals in the frequency domain as noted in (4.11).

$$f(t - T_0) \;\circ\!\!-\!\!\bullet\; e^{-j \cdot T_0 \cdot 2\pi\Omega} \cdot \mathcal{F}(\Omega) \tag{4.11}$$

The result of the transformation of Equation (4.10) into the frequency domain is written in Equation (4.12).

$$\mathcal{F}(\Omega) = \sum_{n=-\infty}^{\infty} e^{-j \cdot (n \cdot T_s + \Delta T_n) \cdot 2\pi\Omega} \tag{4.12}$$

In the case of $\Delta T_n = 0$ the sum of exponential functions can be written as Dirac pulses as in Equation (4.8), this is not the case when a sampling jitter in the form of $\Delta T_n \neq 0$ is present. The sampling jitter causes the Dirac pulses to expand resulting in a blurred quantized signal.

Only on the the special case of $\Delta T_n = T_0 \;\; \forall\, n$ the Dirac pulses are preserved as in Equation (4.13).

$$\mathcal{F}(\Omega) = \frac{1}{T_s} \cdot e^{-j \cdot T_0 \cdot 2\pi\Omega} \cdot \sum_{n=-\infty}^{\infty} \delta(\Omega - n \cdot F_s) \tag{4.13}$$

The previous equations and illustration show that timing inaccuracies limit the analog-to-digital conversion process. The effect of the sampling jitter can be investigated in more detail when considering a single sample.

4.2.5 Jitter Effects on Signal Sampling

The basic principle effect of jitter when sampling a signal can be explained by taking a sine wave as an input signal. A sinusoidal input signal $v(t)$ with an amplitude A and angular frequency $\omega = 2\pi f$ is sampled at the zero crossing $v(t) = 0$.

$$v(t) = A \cdot \sin(\omega \cdot t) \tag{4.14}$$

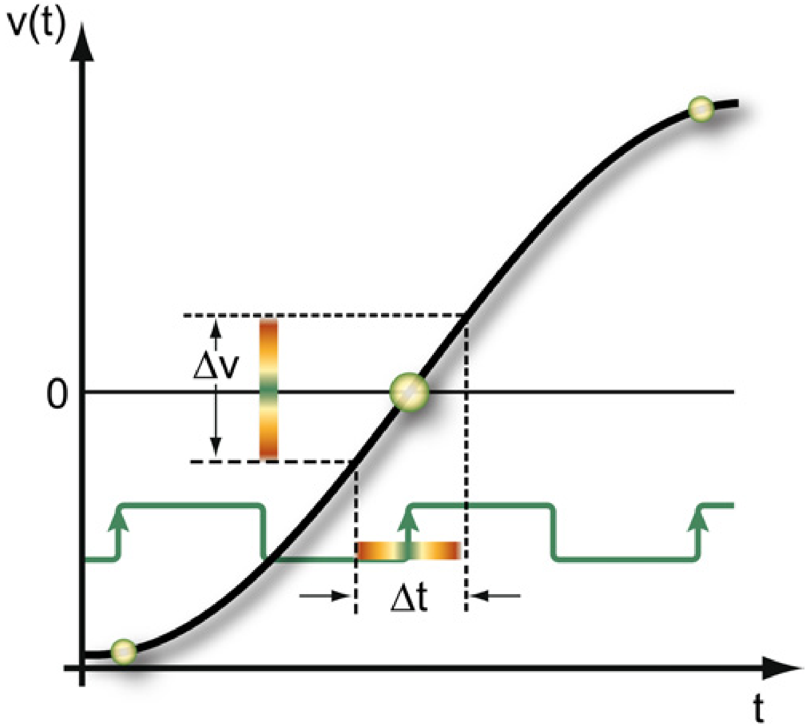

Figure 4.17: Sample time uncertainties result in voltage errors.

The sampling process for the point $\sin(\omega \cdot t) = 0$ is illustrated in Figure 4.17. The slew rate of the signal for a specific point can be calculated with the first derivate as in Equation (4.15).

$$\frac{\mathrm{d}}{\mathrm{d}t} v(t) = A \cdot \omega \cdot \cos(\omega \cdot t) \tag{4.15}$$

The maximum error with the maximum slew rate occurs on $t = 0, \pi$ resulting in $|cos(\omega \cdot t)| = 1$. As a first-order approximation for small values of t it can be said that all $\frac{\mathrm{d}v(t)}{\mathrm{d}t}\Big|_{t=0,\pi} \neq 1$ are erroneous. In this case we can substitute $\mathrm{d}v(t)$ with the error voltage Δv and $\mathrm{d}t$ with the time uncertainty Δt. Therefore we can use Equation (4.17) to calculate the maximum voltage error $(t = 0, \pi)$ occuring at maximum slew rates for a jitter value Δt.

$$\frac{\mathrm{d}v(t)}{\mathrm{d}t} = \frac{\Delta v}{\Delta t} = A \cdot \omega \tag{4.16}$$

$$\Delta v = A \cdot \omega \cdot \Delta t \tag{4.17}$$

This shows that the sampling jitter Δt, an error in time, leads to a voltage error. The error increases with higher signal frequencies caused by higher slew rates.

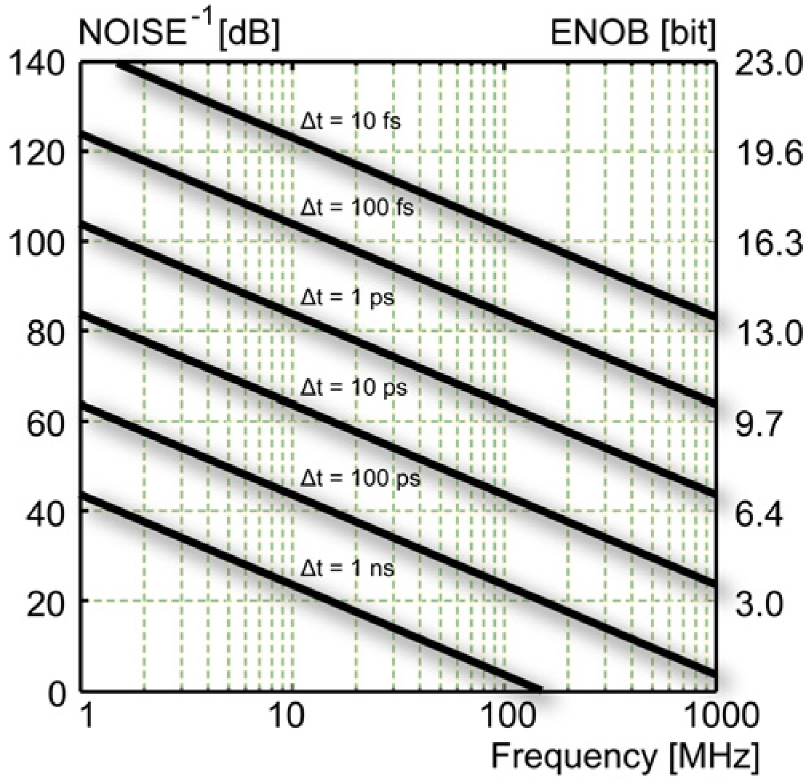

Figure 4.18: Theoretic noise levels depending on timing uncertainties and input frequency.

The theoretical signal-to-noise-ratio (SNR) as limited by timing inaccuracies can be estimated for a standardized sine wave with Equation (4.18).

$$\frac{\Delta v}{A} = 20 \cdot \log(\omega \cdot \Delta t) \text{ dB} \tag{4.18}$$

Figure 4.18 shows the theoretical maximum possible signal-to-noise-ratio (SNR) using Equation (4.18) depending on the input signal frequency f and the timing uncertainty Δt. The diagram applies for full-scale input amplitudes.

An input signal frequency of a maximum of 100 MHz and a noise floor of -80 dB would require sampling jitter of less than 100 fs. This is not easily achievable with current technology standards. Fortunately application specifications lower this requirement where small signal amplitudes are among such factors.

4.2.5.1 Influence of Sampling Clock Jitter for Variable Signal Amplitudes

The influence of sampling jitter varies with the input signal amplitude. The noise level in relation to signal amplitude and sampling jitter for a 50 MHz signal is shown in Figure 4.19 [49; 52]. The y-axis shows the noise relative to the ADC full scale in dB. The x-axis indicates the input signal level normalized to ADC full scale in dB for a fixed signal frequency of 50 MHz. Values for sampling jitter Δt are written above the characteristic lines.

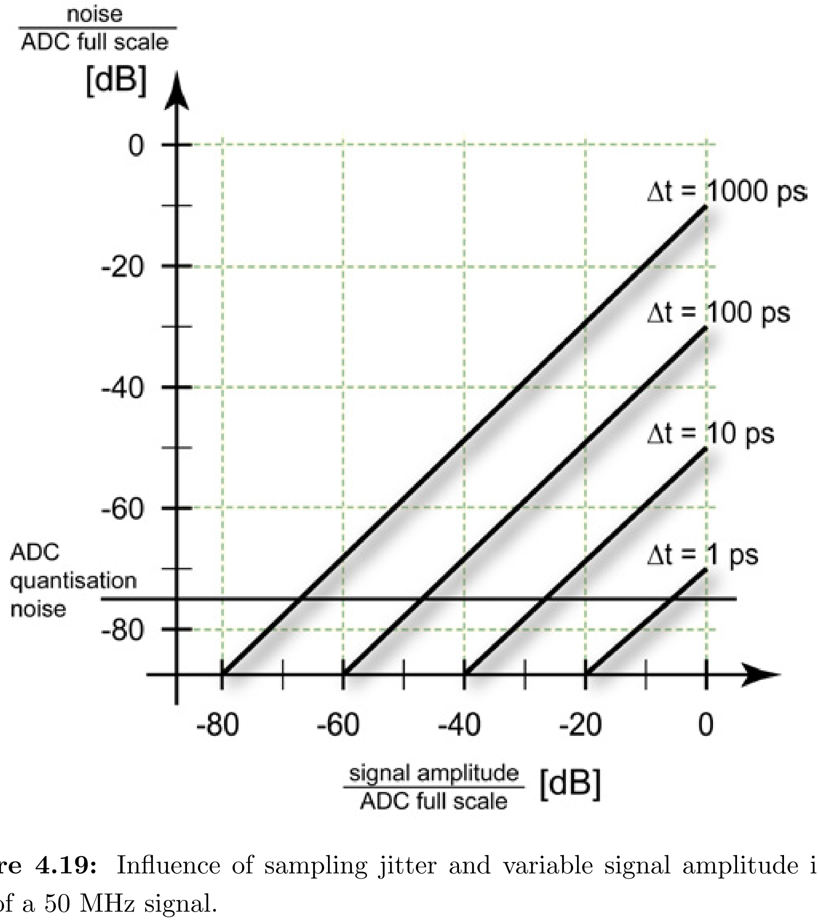

Figure 4.19: Influence of sampling jitter and variable signal amplitude in the case of a 50 MHz signal.

The ADC quantization noise of -75 dB (corresponds to an effective resolution of almost 12 bits) is independent of the signal amplitude (horizontal line), while the sampling jitter produces noise proportional to the signal amplitude (slanted lines). It can be seen that for high signal amplitudes the signal-to-noise ratio is constant and dominated by the sampling jitter. This leads to limited accuracy of the calculated radar echo direction, even for strong echo signals. For low signal amplitudes the ADC quantization noise is the dominant factor in limiting the detectability of weak echo signals. Figure 4.19 illustrates that noise levels are significantly higher for a high sampling clock uncertainty Δt.

4.2.6 Types of Sampling Jitter

One important parameter of analog-to-digital conversion is the influence of sampling related errors. Exact timing is required to achieve low-noise levels. Existing jitter leads to a non-uniform sampling time sequence. This is one of the error sources of analog-digital conversion.

Jitter is the random variation of a waveform, in whole or in part, from the ideal position in time of a periodic signal. Jitter can be converted to phase noise, which is useful when oscillator jitter is considered. The clock jitter or period jitter can be measured as illustrated in Figure 4.20.

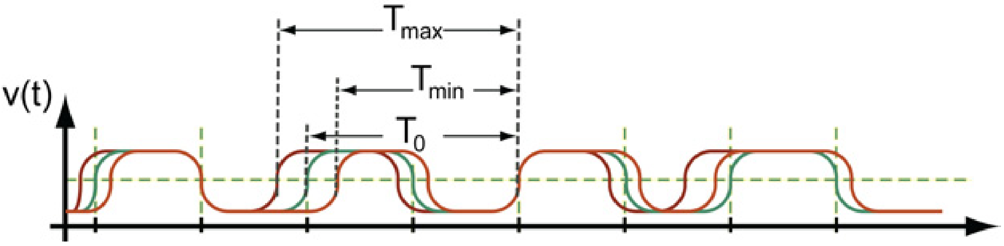

Figure 4.20: Clock jitter measurement.

The clock signal is compared to a reference clock T_0 to measure the clock jitter with $T_{\text{jitter}} = T_{\max} - T_{\min}$.

Besides the different measurement methods, there are two different basic types of jitter. It can be deterministic as in a duty-cycle distortion, asymmetry in rise and fall times or periodic jitter caused by electronic interference. Another form of jitter is random where the source is random noise such as thermal noise. Deterministic jitter is measured as a peak-to-peak value whereas random jitter is measured in terms of a root-mean-square (RMS) value.

4.2.7 Interleaved Sampling Fundamentals

The sampling process of an analog signal is basically a quantized pulse amplitude modulation (PAM) where the analog signal is sampled in equidistant steps. These sampled signals are quantized into the digital domain.

In interleaved sampling systems, several of these measurements are done with the same input signal in an interleaved way. After each interleaving step, the relation of the input signal and sampling signal is shifted in the time domain. The accuracy of this method depends on the accurate repeatability of the input signal and on the precision of the time shifting process. This section will discuss the effects of interleaved sampling timing inaccuracy on the digitalization results.

Several times shifted comb functions, as presented in Equation (4.7), are needed for an interleaved sampling operation to increase the sampling frequency. Thus using an effective comb function with a higher density results in a new effective sampling frequency F_ι. The rule for time shifted signals in the frequency domain is $f(t-t_0) \;\circ\!\!-\!\!\!-\!\!\bullet\; e^{-j\cdot t_0\cdot\Omega}\cdot\mathcal{F}(\Omega)$.

The following equations (4.21) and (4.22) show a sum of shifted comb functions in the time and frequency domain. The value T_k represents the additional interleaved shift of the sampling signal in fractions of the sampling frequency $F_s = \frac{1}{T_s}$ which results in the effective sampling frequency F_ι. The factor ι contains the number of interleaved sampling intervals.

$$F_\iota = \iota \cdot F_s \tag{4.19}$$

$$T_k = \frac{T_s}{\iota} \tag{4.20}$$

$$f_\iota(t) = \sum_{k=0}^{\iota} \sum_{n=-\infty}^{\infty} \delta(t - k\cdot T_k - n\cdot T_s) \tag{4.21}$$

$$\mathcal{F}_\iota(\Omega) = \sum_{k=0}^{\iota} e^{-j\cdot k\cdot T_k\cdot 2\pi\Omega} \cdot \frac{1}{T_s} \sum_{n=-\infty}^{\infty} \delta(\Omega - n\cdot F_s) \tag{4.22}$$

The equations of the sampling signal are illustrated in Figures 4.21 and 4.22 where four interleaved dirac comb functions are used ($\iota = 4$). The shifted separate four comb functions with an individual sampling frequency $F_s = 250$ MHz have to be added in the frequency domain and since the time shifting is ideal it results in an effective sampling rate of $F_\iota = 1000$ MSPS as Illustration 4.23 shows.

In the application of this borehole radar receiver, the representation of a single comb function stays quite accurate because of a relative precise crystal

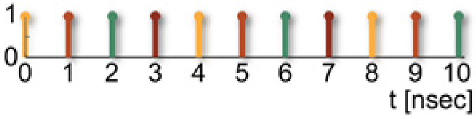

Figure 4.21: Ideal interleaved sampling signal - time domain.

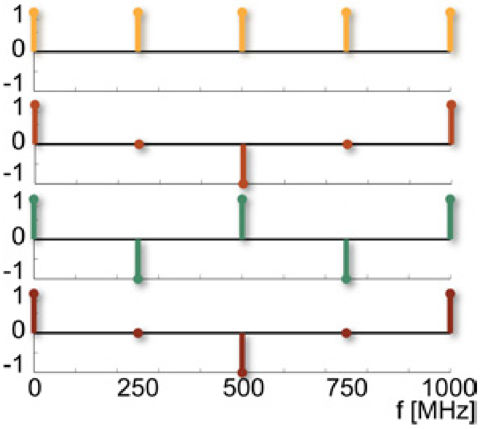

Figure 4.22: Ideal interleaved sampling signal - frequency domain.

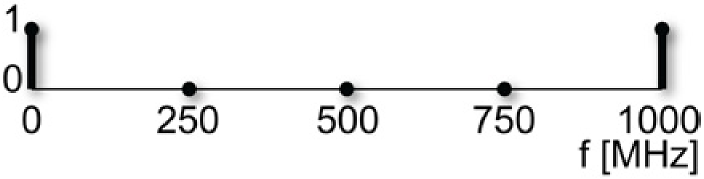

Figure 4.23: Ideal comb function in the frequency domain.

oscillator with low phase noise. Whereas in real interleaved sampling the operation of the shifting process for T_k may be inaccurate due to the elements involved in the process. When using a pulse radar transmitter the time uncertainties of the receiver digitalization circuit are added to the Gaussian jitter of the trigger signal. We will consider these random errors and systematic errors occurring during the sampling process in the next paragraphs.

4.2.8 Interleaved Sampling Errors due to Sample Sequence Inaccuracies

In interleaved sampling, the exact timing and signal level of each of the interleaved A/D converter sweeps is difficult to achieve. The error sources and their weights vary with the interleaved system. The two basic choices of an interleaved system used are illustrated in the block diagrams 4.9 and 4.10. Although the errors are different the effects are similar and after the sampling process it is not easily possible to distinguish minor amplitude errors from small timing errors.

A time uncertainty of a complete interleaved sampling sweep results in a voltage error for every sample. This error can be modeled with a different amplitude of the Dirac comb function, because a timing error results in a voltage error as depicted before in Figure 4.17.

The equations 4.21 and 4.22 can be expanded to include an error time ΔT_k for each interleaved sampling interval k. The trigger time uncertainty of the transmitter is included in the parameter ΔT_k along with jitter in the analog-digital conversion circuit.

$$f_\iota(t) = \sum_{k=0}^{\iota} \sum_{n=-\infty}^{\infty} \delta(t - k \cdot T_k - \Delta T_k - n \cdot T_s) \tag{4.23}$$

$$\mathcal{F}_\iota(\Omega) = \sum_{k=0}^{\iota} e^{-j \cdot \Omega \cdot k \cdot T_k} \cdot e^{-j \cdot \Delta T_k \cdot 2\pi\Omega} \cdot \frac{1}{T_s} \sum_{n=-\infty}^{\infty} \delta(\Omega - n \cdot \Omega_s) \tag{4.24}$$

One extreme deficient situation occurs when one interleaved sampling sweep is missing completely when adding the Dirac comb functions of the sampling sweeps. In cases where there is no timing error ΔT_k and the third ($k = 2$) sampling signal is missing the index k only contains values of $k = 0, 1, 3$ in this example for $\iota = 3$. The resulting sample signal and its spectrum are shown in Figures 4.24 and 4.25.

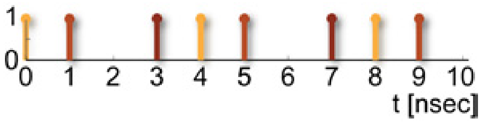

Figure 4.24: Time domain.

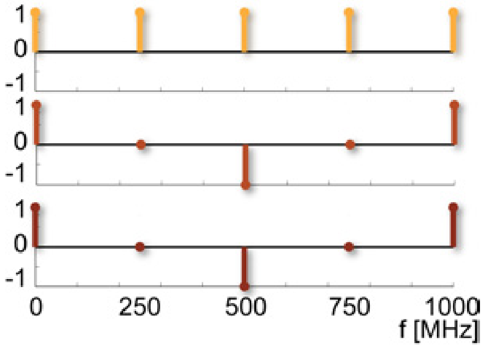

Figure 4.25: Frequency domain.

The interleaved sampling is no longer ideal, because the sum of the separate interleaved sampling signal contains unwanted frequencies as shown in Figure 4.26. A similar result would occur whenever the sum of all single interleaved sampling sweeps contains unwanted signal parts due to amplitude or timing errors. The missing interleaved sampling sweep causes subharmonics in the effective interleaved sample function where the main effective sampling rate remains at 1000 MSPS. Whenever such a signal is used to sample an input signal it is additionally sampled with 250 MSPS, 500 MSPS and 750 MSPS signals.

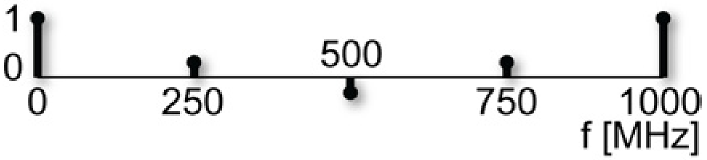

Figure 4.26: Summed inaccurate comb function in the frequency domain.

Equation 4.24 explains the influence of the sampling errors ΔT_k. In the frequency domain this jitter represents subharmonics of the conversion clock. These unwanted additional signals depend on the base sample rate F_s and the number of interleaving sweeps ι. The amount of jitter denoted as ΔT_k influences the signal level of the erroneous image spurs.

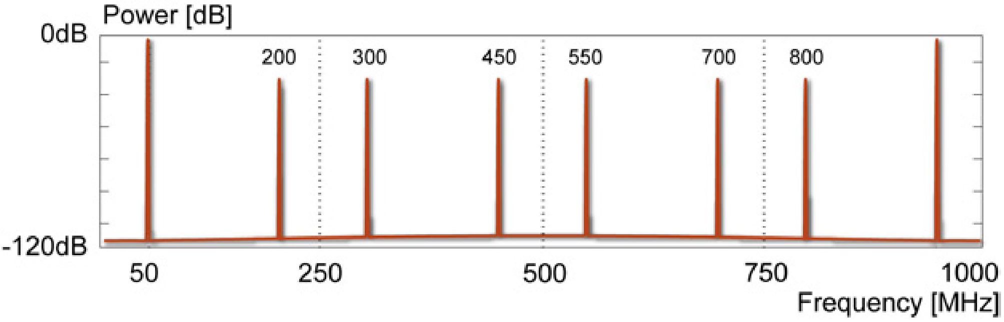

Figure 4.27: Frequency spectrum of an inaccurate sampled 50 MHz input signal with four times interleaved sampling where one interleaved interval is missing.

The resulting spectrum of the sampled input signal contains additional convolution of the original signal spectrum around the subharmonics of the incorrect sampling signals, as illustrated for a 50 MHz sinusoidal input in Figure 4.27. The effect will be explained in detail in regard to the borehole radar receiver application in the next section.

4.2.9 Simulated Measurement Results With Sampling Timing Errors

The effects of different influences of the various sampling errors can be studied further by simulation. In such simulation the digitalization process of the borehole radar receiver can be modeled with its basic elements to analyze different error types.

The core element of the digitalization process is the ADC. Such ADCs are complex electronic parts where each specific converter type has its own specific imperfections. Models of ADCs are supplied among others by Analog Devices [53]. A model for the radar receiver was developed with such a model to test signal sampling with different jitter influences. The analog-to-digital converter AD9246 [54] with a conversion speed of 125 MSPS was chosen in combination with simulated 8 times interleaved sampling resulting in an effective sampling rate of 1000 MSPS. Data stacking is used to reduce the random effects of the added time uncertainties, thus resulting in a better signal quality.

The first simulation compares the effect on the frequency spectrum of sampling clock jitter versus trigger signal jitter during interleaved sampling operation. A single sine wave with a frequency of 50 MHz was used as an input to the sampling process with an effective sampling clock of 1000 MSPS. Additionally a data averaging of 1024 was used to minimize the effect of outliers. This sine input signal is suited to find unwanted erroneous image spurs as for example Figure 4.28 illustrates the errors of the ADC. Moreover, this figure was recorded by using a sampling clock with a very high sampling clock jitter of 1000 ps. Such a high random Gaussian noise results in a low signal-to-noise ratio with an effective number of only 5 bits.

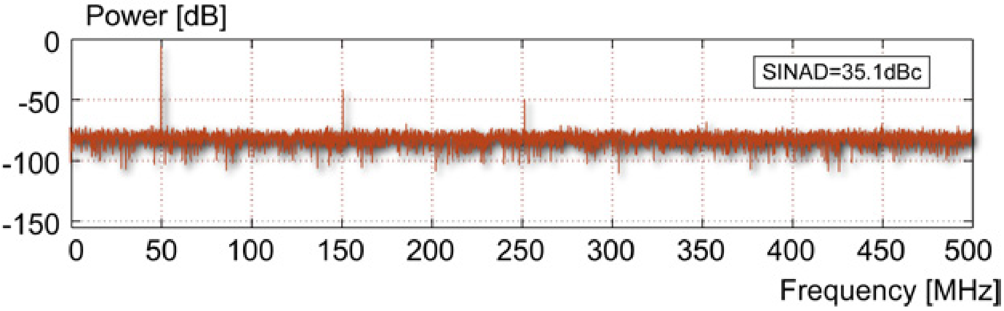

Figure 4.28: Frequency spectrum of a 50 MHz sine wave sampled with a sampling clock with 1000 ps jitter and a sampling rate of 1000 MSPS.

The results of sampling clock jitter can be compared with the effects of trigger jitter in Figure 4.29. The relative systematic error of extensive jitter in the interleaved sampling sweeps causes image spurs additional to the spurs generated by the ADC.

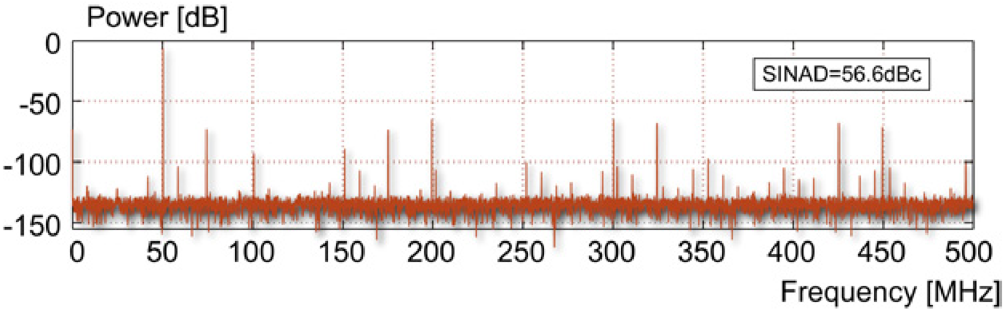

Figure 4.29: Frequency spectrum of a 50 MHz sine wave sampled with a trigger jitter of 1000 ps using 8 times interleaved sampling resulting in an effecting sampling rate of 1000 MSPS.

The simulation clearly shows how advancing ADC technology helps to improve the results of this borehole radar receiver. ADC sampling speeds above 200 MSPS help to reduce errors and remove unwanted signal spurs in the important frequency range. Moreover, averaging can be used to improve the digital signal quality.

A different process to improve measurement result is to calibrate and correct the acquired data where possible. This will be discussed in the next section.

4.3 Calibration and Data Correction

The measurement with a borehole probe is conducted over a time period of several hours. During the data acquisition the probe is moved to different positions in various depths. Regardless, the measurement results have to be independent of the environmental influences like temperature and pressure.

There are several ways to accomplish robust operation. One way is to use a feedback or a regulator circuit to stabilize the receiver electronics. Unfortunately, such methods will damage the noise performance, because closed loop controls add additional noise due to their design.

In order to avoid these effects it is possible to monitor the system characteristics for the different operating conditions. In particular, test signals can be used to measure the system parameters. This alternative allows for parameter optimization and enables correction of the borehole probe data within the data acquisition software.

The angle estimation algorithm relies on the perfect matching of the two loop antenna channels. Additionally the dynamic range extension with the variable gain amplifiers rely on well known relative amplification factors. Carefully selected calibration signals are necessary to obtain the measurement channel parameters which then can be used to match the input channels.

Moreover, a test signal helps to check the condition of the electronics. Regular inspections are important because otherwise faulty measurements might be detected only after several hours. Measurement time is very costly and must be kept to a minimum.

The electrical design uses standard electronic components. All components have specific errors and tolerances. Additionally, systematic distortion and random noise are added to the signals. These errors and tolerances are summarized below:

- input channel mismatch (amplitude, gain, phase, offset)
- interleaved sampling errors due to timing inaccuracies
- antenna tolerances and antenna mismatch
- environmental influences (temperature, moisture)

Most of these error sources cannot be avoided. Errors can be reduced by selecting electronic parts carefully by hand. Such a process is quite time consuming and expensive. Critical parts have to be tested, measured and matched to minimize errors. The matching process is only possible to a certain degree and cannot avoid errors due to a changing operating environment. An easier and more effective method is to measure the errors and correct the measurement results according to the system parameters in the digital domain. The data for error detection and correction can be obtained with adequate test signals.

Additionally, the receiver electronics has different input channels which have to be synchronized in time and amplitude. Test signals help to calibrate such parameters. The antennas can be included in the input channel calibration when an extra antenna is present to transmit the test signal.

The needed calibrations mentioned above have individual requirements for the test signal. As an example signals for ADC testing can be considered. These tests are conducted with sine waves as input signals with frequencies and amplitudes in the low range as well as the high range of the data converter. The next section will discuss a suitable test signal for the borehole radar receiver.

4.3.1 Test and Calibration Signal

Each of the calibration tasks has its own distinctive need on the calibration signal characteristics. Sine waves with different amplification levels and several selectable frequencies are needed to analyze the digitalization process which includes primarily analog-digital-converters and amplifiers. Measurement options similar to a network analyzer seem to be optimal. Unfortunately, the board space is limited and cannot be used for different test generator circuits, nevertheless it is important to find a few test signals to match all the criteria for the correction tasks. As a result, the maximum values for frequency and amplitude of the input channel should be covered by a test sine wave generator as good as possible.

The methods to characterize the digitalization quality depend on sine waves with full scale and low amplitudes. In addition sine waves with different frequencies can determine certain analog-to-digital conversion properties. In order to simplify a test signal only one frequency can already specify enough parameters of the sampling process. Jitter effects can be detected using amplitude differences instead of using several test frequencies.

The estimation of correction parameters to minimize systematic interleaved sampling errors needs a test signal with a known frequency spectrum. Such test signal must be a narrow-band signal in order to be able to find sampling errors in the frequency spectrum. Other parameters of the test signal can be arbitrary.

A signal to determine relative amplification factors has to have a relative exact amplitude. Besides the amplitude the whole dynamic range of the input channels have to be covered as much as possible to allow calibration in the required range.

A simple test signal would consist of several sine waves with amplitudes according to the dynamic range and different frequencies. The frequency of the main calibration signal ω_0 should be approximately in the middle of the appropriate frequency spectrum.

$$v_{\mathrm{sine},i}(t) = A_i \cdot \cos(\omega_0 t) \tag{4.25}$$

The signals $v_{\mathrm{sine},i}(t)$ can be generated with an oscillating circuit connected to a variable amplifier or attenuator. The amplitudes A_i of the test signals shown in Equation (4.25) define how exact the amplification factors can be estimated.

The absolute values for A_i have to be very precise. This is a difficult task, because any error of A_i results in an error when correcting the measurement data proportional to the deviation of the absolute amplitude of the test signal.

It is not possible to have absolute accurate test signal parameters. Therefore these signal parameters need to be determinable after a test measurement.

A more complex calibration signal can be produced by means of a resonance circuit where A is the starting amplitude, τ the time after the signal has decayed to a value of $\frac{1}{e}$ and ω_0 the resonant frequency.

$$v_{\text{damped sine}}(t) = A \cdot e^{-\frac{t}{\tau}} \cdot \cos(\omega_0 t) \tag{4.26}$$

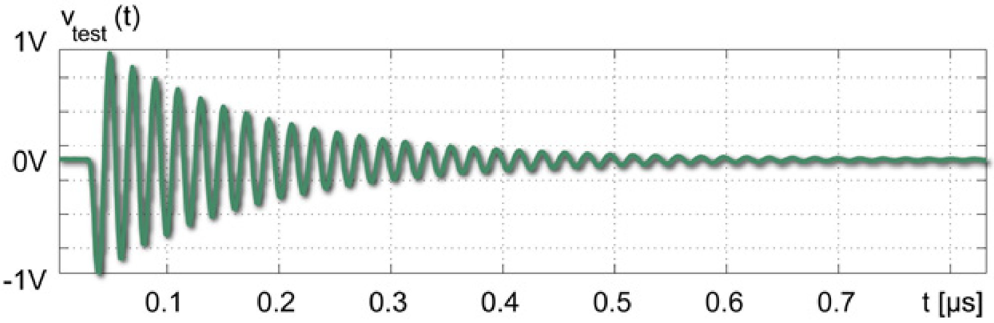

Figure 4.30: Ideal calibration signal $V_{\text{test}}(t)$.

This signal is superior to the signal (4.25) in several ways. The signal in Equation (4.26) has an accurate declining envelope. Figure 4.30 shows such a calibration signal. The declining envelope of the signal passes through the full dynamic range. Therefore it enables a good relative calibration of all three channels with one signal. The advantage to this method is that it relies on relative amplitudes rather than on absolute values, for e.g. Equation (4.25). The parameters A, ω_0 and τ have to be stable only for a relative short calibration measurement for one location. Such stability is comfortably achievable with a measurement time in an order of a few seconds.

The signal generator for a damped sine wave required less parts than an oscillator. Additionally less energy is required to generate these damped signals compared to oscillating signals, which is important to consider in a battery powered device.

The out of range recovery time can be tested using a damped sine wave by setting the starting amplitude A higher than the input range. Such a test is not directly possible when using a sine wave oscillator.

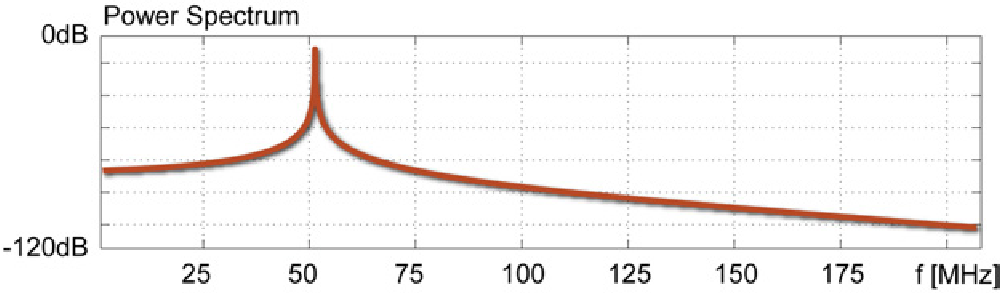

Figure 4.31: Ideal frequency spectrum of calibration signal.

A narrow-band signal is required to detect systematic sampling errors. The signal in Equation (4.26) meets this criteria. The frequency spectrum can be calculated with the Fourier transformation in Equation (4.27). The signal calculated in (4.28) is depicted in Figure 4.31.

$$V_{\text{damped sine}}(\omega) = \frac{1}{\sqrt{2\pi}} \cdot \int_0^\infty v_{\text{damped sine}}(t) \cdot e^{-j\omega t} dt \tag{4.27}$$

$$V_{\text{damped sine}}(\omega) = \frac{A}{\sqrt{2\pi}} \cdot \frac{1/\tau + j\omega}{(1/\tau + j\omega)^2 + \omega_0^2} \tag{4.28}$$

The accuracy of the test signal function needs to be better than the digitalization process for error detection and calibration. In contrast the test signal parameters need only to be stable for a short time while the signal characteristics have to be accurate. Therefore a test signal generator with high signal quality is needed.

4.3.2 Test Signal Generator

The electronics of the calibration signal generator resides together with the receiver data acquisition unit within the antenna where the calibration signal is fed into the measuring channels in parallel. This requires a small energy efficient solution where the signal generator has to produce a signal according to Equation (4.29).

$$v_{\text{test}}(t) = A \cdot \cos(\omega t + \varphi) \cdot e^{-\frac{t}{\tau}} \tag{4.29}$$

4.3.2.1 Electronic Circuit for a Decaying Sine Wave

An efficient circuit is a current source which is used to trigger a parallel resonant circuit. The principle represents a damped harmonic oscillator. This type of oscillator is equivalent to a mechanical spring-mass system.

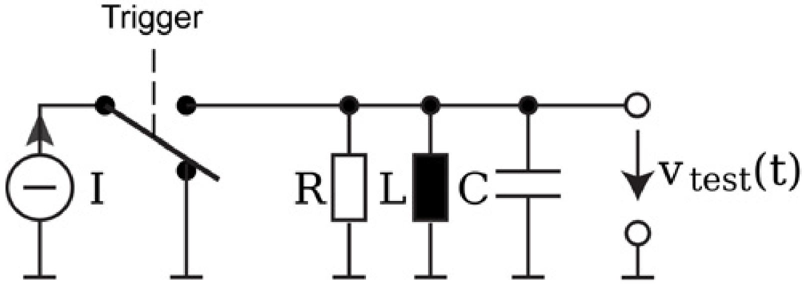

Figure 4.32: Damped harmonic oscillator as calibration signal generator.

The resulting transient voltage of the circuit shown in Illustration 4.32 for switching the current source can be calculated with the homogeneous differential equation noted in (4.30).

$$\ddot{v}_{\mathrm{test}}(t) + \frac{1}{R \cdot C} \cdot \dot{v}_{\mathrm{test}}(t) + \frac{1}{L \cdot C} \cdot v_{\mathrm{test}}(t) = 0 \tag{4.30}$$

In order to simplify the equation we use substitutions (4.31) and (4.32).

$$\omega_0^2 = \frac{1}{L \cdot C} \tag{4.31}$$

$$\tau = 2 \cdot R \cdot C \tag{4.32}$$

The characteristic equation for solving the differential equation is written in (4.33).

$$\lambda^2 + \frac{2}{\tau} + \omega_0^2 = 0 \tag{4.33}$$

The solution to the quadratic Equation (4.33) for λ is shown in Equation (4.34). It is used to solve the homogeneous differential equation.

$$\lambda_{1/2} = -\frac{1}{\tau} \pm \sqrt{\left(\frac{1}{\tau}\right)^2 - \omega_0^2} \tag{4.34}$$

The desired solution of a declining sine wave for the homogeneous differential equation is only valid if the requirement in Equation (4.35) is met. Therefore the solutions $\lambda_{1/2}$ are conjugated complex roots as represented in Equation (4.37) using the substitution (4.36).

$$\frac{1}{\tau} < \omega_0 \tag{4.35}$$

$$\omega_1 = \sqrt{\omega_0^2 - \left(\frac{1}{\tau}\right)^2} \tag{4.36}$$

$$\lambda_{1/2} = -\frac{1}{\tau} \pm j \cdot \omega_1 \tag{4.37}$$

The solution of this equation for a damped oscillator can be found with the above requirement (4.35) where this constraint limits the maximum allowable damping constant. The common solution to the differential equation in this case is (4.38).

$$v_{\text{test}}(t) = (B \cdot \cos(\omega_1 t) - C \cdot \sin(\omega_1 t)) \cdot e^{-\frac{t}{\tau}} \tag{4.38}$$

Now, Equation (4.38) can be rewritten as in Equation (4.39) to match the required form of Equation (4.29).

$$v(t) = A \cdot \cos(\omega_1 t + \varphi) \cdot e^{-\frac{t}{\tau}} \tag{4.39}$$

$$\varphi = \arctan\left(-\frac{C}{B}\right) \tag{4.40}$$

$$A = \sqrt{B^2 + C^2} \tag{4.41}$$

The starting amplitude can be calculated for $t = 0$ with Equation (4.42).

$$A = I * R \tag{4.42}$$

The calculations above provide the foundation to calculate the values for the electronic parts for specific signal parameters in Equation (4.29). The parts have to be chosen according to the requirement mentioned in (4.35). That means the value of resistor R has to fulfill the Relation (4.43) for a given undamped resonance frequency ω_0.

$$R \cdot C < \frac{1}{2 \cdot \omega_0} \tag{4.43}$$

The interrelationship of the parameters in Equation (4.29) and the electrical components are summarized below.

$$\omega = \sqrt{\frac{1}{L \cdot C} - \frac{1}{\tau^2}} \approx \frac{1}{\sqrt{L \cdot C}} \tag{4.44}$$

$$\tau = 2 \cdot R \cdot C \tag{4.45}$$

$$A = I \cdot R \tag{4.46}$$

Temperature changes and other environmental influences change the amplitude and the frequency of the generator circuit to a certain degree. These changes occur relatively slow over time in different probe positions. This resulting absolute error can be tolerated because only short time stability is needed to match measurement results for one position and all channels.

4.3.3 Algorithm for Obtaining Test Signal Parameters

The four parameters of Equation (4.29) and a possible signal offset can be calculated by using measured data using the input channels of the digitizing unit. A method for reliable parameter calculation is introduced below.

4.3.3.1 Test Signal Parameter Estimation

Estimated test signal parameters provide an efficient method for a fast test of the radar receiver requiring only few microprocessor resources. As a first step the parameter estimation provides starting values for an iterative algorithm. Thereafter the exact signal parameters can be iteratively calculated.

The data correction process is based on the parameters of the test signal in Equation (4.29). The five parameters A, ω, φ, τ and DC can be calculated from the recorded digitalized data. A common method is represented by parameter fitting as used for ADC testing in IEEE standard 1241 [55] or IEEE standard 1057 [56]. These sine wave fitting algorithms can be extended or modified to model a decaying sine wave.

A basic method for parameter estimation for a damped sine wave is presented in [57]. This estimation is one option to calculate starting values for a nonlinear fitting algorithm. A step-by-step calculation for four of the parameters is developed below to show the principle. A robust implementation is important - especially if the digitalization is not adjusted well.

A Fourier transformation can be used to find the fundamental frequency of the signal. Alternatively the frequency of the test signal can be estimated by measuring the time and number of zero crossings between two points of the signal. Both methods are illustrated in Figure 4.33 where the counting of zero crossings is described mathematically in equations (4.47) and (4.48) where DC(t) represents an slowly with time varying erroneous offset voltage with small amplitude.

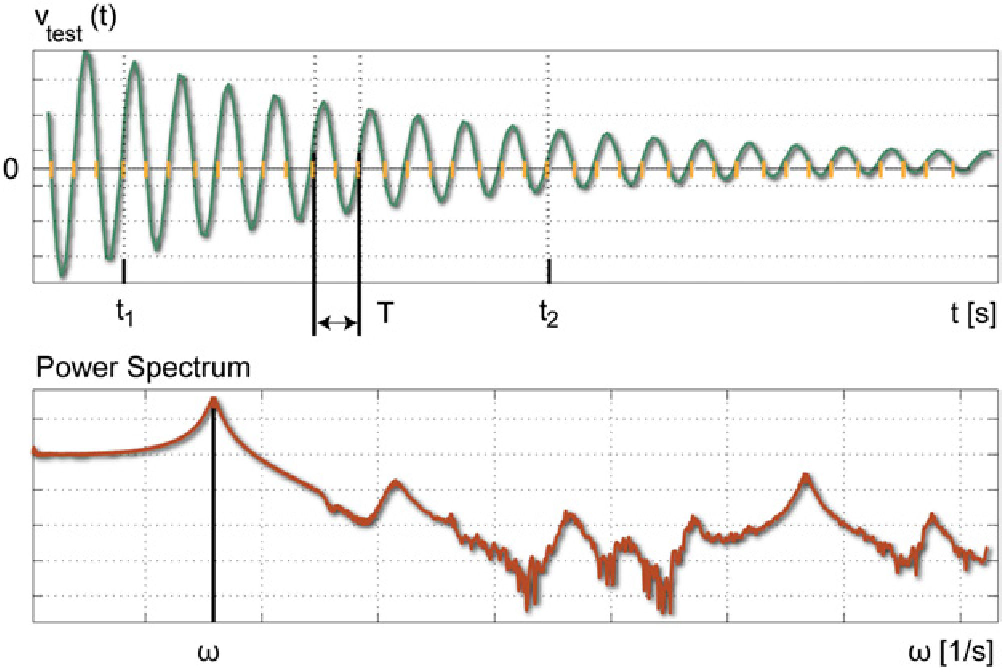

Figure 4.33: Frequency estimation by examining zero-crossings (upper graph) and fourier transformation (lower graph).

$$V_{\text{test}}(t_1) = A \cdot \cos(\omega \cdot t_1 + \varphi) \cdot e^{-\frac{t_1}{\tau}} + \text{DC}(t_1) = 0 \tag{4.47}$$

$$V_{\text{test}}(t_2) = A \cdot \cos(\omega \cdot t_2 + \varphi) \cdot e^{-\frac{t_2}{\tau}} + \text{DC}(t_2) = 0 \tag{4.48}$$

The angular frequency ω can be calculated by counting the number of zero crossings n_0 between t_1 and t_2 as shown in Equation (4.49) where averaging can be used to achieve more exact results. This method works quite well for $\mathrm{DC}(t) = 0$ where the zero crossings contain no varying offset.

$$\omega = \frac{\pi \cdot n_0}{t_2 - t_1} \tag{4.49}$$

Although averaging can be used for counting the zero crossings, this process is very sensitive to any variable offset $\mathrm{DC}(t)$ which can contain very low frequencies. Therefore the method using a frequency spectrum for the estimation of ω can be considered as more robust and hence the preferred choice to estimate the parameter ω. The accuracy can be increases further by interpolation [58].

Knowing the approximate frequency of the test signal leads to the computation of the phase φ by counting the zero crossings n_0 from a reference point with $t_1 = 0$ whereas the result of Equation (4.50) has to be corrected by adding 180° if the signal direction of the first zero crossing is negative.

$$\varphi = (\frac{\omega}{2\pi} t_2 - \frac{n_0}{2}) \cdot 180^\circ \tag{4.50}$$

Two maxima or minima t_1 and t_2 of the test signal are used to calculate the time constant τ by comparing the amplitude as in (4.51).

$$\frac{v_{\text{test}}(t_1)}{v_{\text{test}}(t_2)} = \frac{A \cdot \sin(\omega_0 t_1 + \varphi) \cdot e^{-\frac{t_1}{\tau}}}{A \cdot \sin(\omega_0 t_2 + \varphi) \cdot e^{-\frac{t_2}{\tau}}} \tag{4.51}$$

The equation above can be solved for τ:

$$\frac{v_{\text{test}}(t_1) \cdot \cos(\omega_0 t_2 + \varphi)}{v_{\text{test}}(t_2) \cdot \sin(\omega_0 t_1 + \varphi)} = e^{\frac{t_2 - t_1}{\tau}} \tag{4.52}$$

$$\tau = \ln \frac{v_{\text{test}}(t_2) \cdot \cos(\omega_0 t_1 + \varphi)}{v_{\text{test}}(t_1) \cdot \sin(\omega_0 t_2 + \varphi)} \cdot (t_2 - t_1) \tag{4.53}$$

Equation (4.53) can be simplified when using maxima and minima of the signal which results in $\sin(\omega_0 t + \varphi) = \pm 1$. This calculation is illustrated in Figure 4.34.

$$\tau = \ln \frac{v_{\text{test}}(t_2)}{v_{\text{test}}(t_1)} \cdot (t_2 - t_1) \tag{4.54}$$

The average value for τ can be estimated by calculating a value for each maximum and minimum in reference to a start value at t_1. The result of

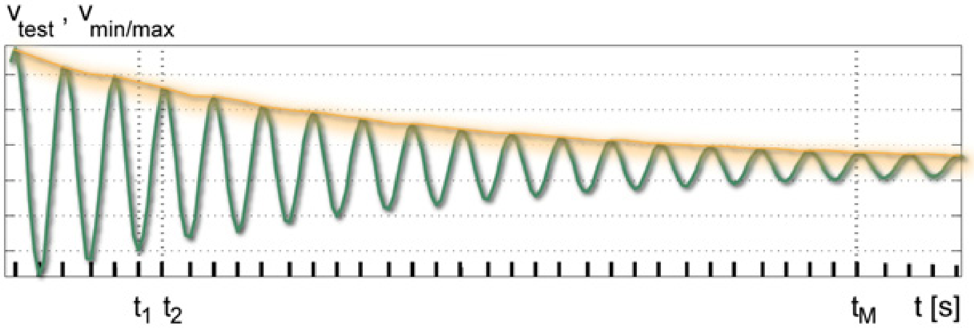

Figure 4.34: Principle of parameter estimation for τ.

Equation (4.55) is used as an estimated start value τ_0 for further processing later on.

$$\tau_0 = \frac{1}{M-1} \sum_{n=2}^{M} \ln \frac{v_{\text{test}}(t_n)}{v_{\text{test}}(t_1)} \cdot (t_n - t_1) \tag{4.55}$$

The amplitude A is the last parameter to be estimated. It can be estimated with the other parameters at a given point in time t_1 where averaging should be used to achieve better results.

$$A = \frac{V_{\text{test}}(t_1)}{\cos(\omega t_1 + \varphi)} \cdot e^{\frac{t_1}{\tau}} \tag{4.56}$$

Another method to calculate the parameters of the amplitude A, angle φ and offset DC uses a least-square fit of a linear combination as suggested in the IEEE standard 1241 [55]. This method minimizes the function (4.57) to fit the parameters $a_1 \dots a_m$ by subtracting the measured signal samples v_n from a model function $u(t_i, a_1 \dots a_m)$. The parameter t_i of the model function (4.57) is the time of the sample depending on the index i and can be calculated with the sampling interval T_s and sample number n with $t_i = n \cdot T_s$.

$$\sum_{n=1}^{M} (v_n - u(t_i; a_1 \dots a_m))^2 \tag{4.57}$$

The estimation process solves a system of equations where the model function in (4.58) has to be rewritten using the relation in (4.59). This modification replaces the term for $\cos(\omega t_1 + \varphi)$ to result in a linear combination for the parameters to be fitted.

$$u(t) = A \cdot \cos(\omega t + \varphi) \cdot e^{-\frac{t}{\tau}} + \text{DC} \tag{4.58}$$

$$A \cdot \cos(\omega t + \varphi) = A \cos(\omega t) \cos\varphi - A \sin(\omega t) \sin\varphi \tag{4.59}$$

The parameter A and φ can be substituted by two new parameters B and C as written in the following equations:

$$B = A \cdot \cos\varphi \tag{4.60}$$

$$C = -A \cdot \sin\varphi \tag{4.61}$$

The parameter substitution results in the new model (4.62) which can be solved for B, C and DC by means of least-square fitting with a linear combination for a fixed value for ω.

$$u(t) = B \cdot \cos(\omega t) \cdot e^{-\frac{t}{\tau}} + C \cdot \sin(\omega t) \cdot e^{-\frac{t}{\tau}} + \mathrm{DC} \tag{4.62}$$

The design matrix D_0 for least-square fitting is written out in (4.63).

$$D_0 = \begin{bmatrix} \cos(\omega \cdot t_1) \cdot e^{-\frac{t}{\tau}} & \sin(\omega_0 \cdot t_1) \cdot e^{-\frac{t}{\tau}} & 1 \\ \cos(\omega \cdot t_2) \cdot e^{-\frac{t}{\tau}} & \sin(\omega_0 \cdot t_2) \cdot e^{-\frac{t}{\tau}} & 1 \\ \vdots & \vdots & \vdots \\ \cos(\omega \cdot t_M) \cdot e^{-\frac{t}{\tau}} & \sin(\omega_0 \cdot t_M) \cdot e^{-\frac{t}{\tau}} & 1 \end{bmatrix} \tag{4.63}$$

The vector $\vec{v}$ represents the measured digital sampled data of the test signal whereas the vector $\vec{x}_0$ contains the parameters the equation system is solved for.

$$\vec{v} = \begin{bmatrix} v_1 \\ v_2 \\ \vdots \\ v_M \end{bmatrix} \quad , \quad \vec{x}_0 = \begin{bmatrix} B_0 \\ C_0 \\ \mathrm{DC}_0 \end{bmatrix} \tag{4.64}$$

The linear equation system $D_0 \cdot \vec{x}_0 = \vec{v}$ as noted in Equation (4.65) can be solved for x_0 with Equation (4.66).

$$\begin{bmatrix} \cos(\omega \cdot t_1) \cdot e^{-\frac{t}{\tau}} & \sin(\omega \cdot t_1) \cdot e^{-\frac{t}{\tau}} & 1 \\ \cos(\omega \cdot t_2) \cdot e^{-\frac{t}{\tau}} & \sin(\omega \cdot t_2) \cdot e^{-\frac{t}{\tau}} & 1 \\ \vdots & \vdots & \vdots \\ \cos(\omega \cdot t_M) \cdot e^{-\frac{t}{\tau}} & \sin(\omega \cdot t_M) \cdot e^{-\frac{t}{\tau}} & 1 \end{bmatrix} \cdot \begin{bmatrix} B_0 \\ C_0 \\ \mathrm{DC}_0 \end{bmatrix} = \begin{bmatrix} v_1 \\ v_2 \\ \vdots \\ v_M \end{bmatrix} \tag{4.65}$$

However, the matrix inversion in (4.66) is in some cases numerical not stable, therefore it is recommended to replace it by a Gaussian elimination process or matrix factorization algorithm [58; 59].

$$\vec{x}_0 = (D_0^T \cdot D_0)^{-1} \cdot D_0^T \cdot \vec{v} \tag{4.66}$$

Now these estimated parameters of the test signal in vector x_0 can be used with a nonlinear least-square fitting algorithm to achieve a best fitted result. There are many different non-linear least-square fitting algorithm as included in the software package MATLAB as function lsqcurvefit() or algorithms provided as C/C++ source code [59]. In the following, an iterative algorithm is presented which can accomplish the parameter fitting with a linear least-square fitting algorithm.

4.3.3.2 Iterative Algorithm for Test Signal Parameter Fitting

The above estimated test signal parameters B_0, C_0, DC_0 and τ_0 are needed for a fitting algorithm to serve as start values for an iterative process. The fitting algorithm according to IEEE 1241 contains Equation (4.67) as a model function.

$$u(t) = B \cdot \cos(\omega t) + C \cdot \sin(\omega t) + \mathrm{DC} \tag{4.67}$$

A closer look to the IEEE standard 1241 for ADC testing reveals that this method can be modified to match a decaying sine wave which is described by Equation (4.62). As in the last section, this model is used to fit the damped sine wave function and can be used then to compute the least square fit as shown in Equation (4.68).

$$\sum_{n=1}^{M} (v_n - B_i \cdot \cos(\omega_i t) \cdot e^{-\frac{t}{\tau}} - C_i \cdot \sin(\omega_i t) \cdot e^{-\frac{t}{\tau}} - \mathrm{DC}_i)^2 \tag{4.68}$$

The parameters ω and τ are non-linear parameters which can not be estimated by a basic least square fitting algorithm using an overestimated system of linear equations. The model can be extended by a first order Taylor series expansion around the initial estimate as shown in the following equations.

$$\widetilde{u}(\vec{x}, \omega)|_{\omega_i} \approx u(\vec{x}, \omega_i) + \frac{\partial u(\vec{x}, \omega_i)}{\partial \omega} \cdot \overbrace{(\omega - \omega_i)}^{\Delta\omega_i} \tag{4.69}$$

with

$$\vec{x} = \left[B_i, C_i, \mathrm{DC}_i\right]^T \tag{4.70}$$

$$\Delta\omega_i = \omega - \omega_{0,i} \tag{4.71}$$

The derivative of Equation (4.62) in ω is written in Equation (4.72).

$$\frac{\partial u(t)}{\partial \omega} = -B \cdot t \cdot \sin(\omega t) \cdot e^{-\frac{t}{\tau}} + C \cdot t \cdot \cos(\omega t) \cdot e^{-\frac{t}{\tau}} \tag{4.72}$$

The function to be minimized with the method of the least squares contains an error term $\Delta\omega$ which is small due to the initial estimated value ω_0. The parameters of the following equation can be estimated by a standard least square fitting algorithm by assuming linearity in ω for small errors $\Delta\omega$ resulting in $\Delta\omega_i \approx 0$. The equation below requires the result of the initial parameters or previous iteration results for parameters B_{i-1} and C_{i-1}.

$$\begin{aligned} \widetilde{u}_i \approx{}& B_i \cdot \cos(\omega_i t) \cdot e^{-\frac{t}{\tau}} + C_i \cdot \sin(\omega_i t) \cdot e^{-\frac{t}{\tau}} + \mathrm{DC}_i \\ & - \Delta\omega_i \cdot B_{i-1} \cdot t \cdot \sin(\omega t) \cdot e^{-\frac{t}{\tau}} + \Delta\omega_i \cdot C_{i-1} \cdot t \cdot \cos(\omega t) \cdot e^{-\frac{t}{\tau}} \end{aligned} \tag{4.73}$$

The least square fitting algorithm is similar to the set of linear equations used for parameter estimation earlier in Equation (4.65) where the new parameter $\Delta\omega$ for the iterative adjustment of ω is added. The modified linear equation system used for the iteration process can be found in Equations (4.74) to (4.76).

$$D_i = \begin{bmatrix} \cos(\omega t_1)e^{-\frac{t}{\tau}} & \sin(\omega t_1)e^{-\frac{t}{\tau}} & 1 & -B_{i-1}t_1 \sin(\omega t)e^{-\frac{t}{\tau}} + C_{i-1}t_1 \cos(\omega t)e^{-\frac{t}{\tau}} \\ \cos(\omega t_2)e^{-\frac{t}{\tau}} & \sin(\omega t_2)e^{-\frac{t}{\tau}} & 1 & -B_{i-1}t_2 \sin(\omega t)e^{-\frac{t}{\tau}} + C_{i-1}t_2 \cos(\omega t)e^{-\frac{t}{\tau}} \\ \vdots & \vdots & \vdots & \vdots \\ \cos(\omega t_M)e^{-\frac{t}{\tau}} & \sin(\omega t_M)e^{-\frac{t}{\tau}} & 1 & -B_{i-1}t_M \sin(\omega t)e^{-\frac{t}{\tau}} + C_{i-1}t_M \cos(\omega t)e^{-\frac{t}{\tau}} \end{bmatrix} \tag{4.74}$$

$$\vec{v} = \begin{bmatrix} v_1 \\ v_2 \\ \vdots \\ v_M \end{bmatrix} \quad , \quad \vec{x}_i = \begin{bmatrix} B_i \\ C_i \\ \mathrm{DC}_i \\ \Delta\omega_i \end{bmatrix} \tag{4.75}$$

$$D_i \cdot \vec{x} = \vec{v} \tag{4.76}$$

The iteration process has to be prepared by setting the vector x_i to the default values calculated earlier by setting $\vec{x}_i = \vec{x}_0$, $\tau = \tau_0$, $\Delta\omega_0 = 0$ and resetting the index counter $i = 0$. The iteration process itself involves the following steps:

1. $i = i + 1$
2. update ω_i with $\omega_i = \omega_{i-1} + \Delta\omega_{i-1}$
3. compute the least square solution $\vec{x}_i = (D_i^T \cdot D_i)^{-1} \cdot D_i^T \cdot \vec{v}$
4. stop iteration, if the changes in frequency $\Delta\omega$ are small according to the required accuracy

The fitted parameters are stored in $\vec{x}_i$ and are needed for further processing. The last parameter left to be improved is τ. The fitting of τ is accomplished by using a standard least-square fitting algorithm using a modified model function as with estimating parameter ω. An error term for the parameter τ can be added to the previous defined model Function (4.62) by utilizing a Taylor series expansion around τ_i as written in Equation (4.77).

$$\widetilde{u}(\vec{x}, \tau)|_{\tau_i} \approx u(\vec{x}, \tau_i) + \frac{\partial u(\vec{x}, \tau_i)}{\partial \tau} \cdot \overbrace{(\tau - \tau_i)}^{\Delta\tau_i} \tag{4.77}$$

with

$$\vec{x} = \left[B_i, C_i, \mathrm{DC}_i\right]^T \tag{4.78}$$

$$\Delta\tau_i = \tau - \tau_{0,i} \tag{4.79}$$

The derivative of Equation (4.62) in τ is written in Equation (4.80).

$$\frac{\partial u(t)}{\partial \tau} = -B \cdot \frac{t}{\tau^2} \cdot \sin(\omega t) \cdot e^{-\frac{t}{\tau}} - C \cdot \frac{t}{\tau^2} \cdot \cos(\omega t) \cdot e^{-\frac{t}{\tau}} \tag{4.80}$$

The error term $\Delta\tau$ is small because of the initial estimated value resulting in $\Delta\tau_i \approx 0$. Therefore linearity can be assumed for the fitting algorithm and the parameters can be estimated again by a standard linear least square fitting algorithm. The model function is written in Equation (4.81).

$$\begin{aligned}\widetilde{u}_i \approx\ & B_i \cdot \cos(\omega_i t) \cdot e^{-\frac{t}{\tau}} + C_i \cdot \sin(\omega_i t) \cdot e^{-\frac{t}{\tau}} + \mathrm{DC}_i \\ & - \Delta\tau_i \cdot B_{i-1} \cdot \frac{t}{\tau^2} \cdot \sin(\omega t) \cdot e^{-\frac{t}{\tau}} - \Delta\tau_i \cdot C_{i-1} \cdot \frac{t}{\tau^2} \cdot \cos(\omega t) \cdot e^{-\frac{t}{\tau}}\end{aligned} \tag{4.81}$$

The modified linear equation system used for the iteration can be found in Equations (4.82) to (4.84).

$$D_i = \begin{bmatrix} \cos(\omega t_1)e^{-\frac{t}{\tau}} & \sin(\omega t_1)e^{-\frac{t}{\tau}} & 1 & -B_{i-1}\frac{t_1}{\tau^2}\sin(\omega t)e^{-\frac{t}{\tau}} - C_{i-1}\frac{t_1}{\tau^2}\cos(\omega t)e^{-\frac{t}{\tau}} \\ \cos(\omega t_2)e^{-\frac{t}{\tau}} & \sin(\omega t_2)e^{-\frac{t}{\tau}} & 1 & -B_{i-1}\frac{t_2}{\tau^2}\sin(\omega t)e^{-\frac{t}{\tau}} - C_{i-1}\frac{t_2}{\tau^2}\cos(\omega t)e^{-\frac{t}{\tau}} \\ \vdots & \vdots & \vdots & \vdots \\ \cos(\omega t_M)e^{-\frac{t}{\tau}} & \sin(\omega t_M)e^{-\frac{t}{\tau}} & 1 & -B_{i-M}\frac{t_1}{\tau^2}\sin(\omega t)e^{-\frac{t}{\tau}} + C_{i-1}\frac{t_M}{\tau^2}\cos(\omega t)e^{-\frac{t}{\tau}} \end{bmatrix} \tag{4.82}$$

$$\vec{v} = \begin{bmatrix} v_1 \\ v_2 \\ \vdots \\ v_M \end{bmatrix} \quad , \quad \vec{x}_i = \begin{bmatrix} B_i \\ C_i \\ \mathrm{DC}_i \\ \Delta\tau_i \end{bmatrix} \tag{4.83}$$

$$D_i \cdot \vec{x} = \vec{v} \tag{4.84}$$

The iteration process is the same as for the frequency estimation explained earlier. The process is initialized by resetting the index counter $i = 0$ and using the values calculated earlier for $\vec{x}_i$, $\tau_i = \tau_0$. The iteration process itself involves the following steps:

1. $i = i + 1$
2. update τ_i with $\tau_i = \tau_{i-1} - \Delta\tau_{i-1}$
3. compute the least square solution $\vec{x}_i = (D_i^T \cdot D_i)^{-1} \cdot D_i^T \cdot \vec{v}$
4. stop iteration, if the changes in $\Delta\tau$ are small according to the required accuracy

The fitted parameter for the amplitudes B_i and C_i can be used to calculate the amplitude A and the angle φ as written in (4.85) and (4.86). The relationship of the two models and the parameters is explained in equations (4.58) and (4.59).

$$A = \sqrt{B_i^2 + C_i^2} \tag{4.85}$$

$$\varphi = \arctan(-C_i/B_i) \quad \forall\ B_i > 0 \tag{4.86}$$

$$\varphi = \frac{3}{2} \cdot \pi \quad \forall\ B_i = 0\ \&\ \ C_i \geq 0 \tag{4.87}$$

$$\varphi = \frac{1}{2} \cdot \pi \quad \forall\ B_i = 0\ \&\ \ C_i < 0 \tag{4.88}$$

$$\varphi = \arctan(-C_i/B_i) + \pi \quad \forall\ B_i < 0 \tag{4.89}$$

$$u(t) = A \cdot \cos(\omega t + \varphi) \cdot e^{-\frac{t}{\tau}} + \mathrm{DC} \tag{4.90}$$

After data processing all the parameters of the test signal (4.90) are defined. As an example the amplitude parameter A can be used to match the different input channels and assemble radar echoes recorded with different amplifier settings. Moreover, these numbers allow for checking and specifying the digitalization process.

4.3.3.3 Residual Calculation and Signal Comparison

The calculated parameters of the test signal can be used to test for a correct receiver operation. An error free ideal test signal can be reconstructed with the signal parameters of the decaying sine wave. This ideal signal can be compared to the measured signal.

The residuals $r(t)$ specify the difference between the measured signal $v(t)$ and the model $u(t)$ which can be calculated with (4.91).

$$r(t) = v(t) - A \cdot \cos(\omega t + \varphi) \cdot e^{-\frac{t}{\tau}} - \mathrm{DC} \tag{4.91}$$

The overall error as root-mean-square value can be calculated with the residuals $r(t)$ and describes the total noise e_{RMS} in Equation (4.92).

$$e_{\mathrm{RMS}} = \sqrt{\frac{1}{M} \sum_{n=1}^{M} r(n \cdot T_s)^2} \tag{4.92}$$

The sampling process can be monitored further when comparing the errors of the separate interleaved sampling sweeps. The residual calculation (4.91) and the computing of the error value can be modified to include only one interleaved sampling interval k out of the total number of sampling intervals ι as shown in Equation (4.93).

$$e_{k,\mathrm{RMS}} = \sqrt{\frac{1}{M} \sum_{n=1+k}^{M} r(\iota \cdot n \cdot T_s)^2} \tag{4.93}$$

The error terms $e_{k,\mathrm{RMS}}$ can be compared for every interleaved sampling interval k. Consequently abnormalities in certain intervals can be detected and adjusted by sample time corrections.

The calculated parameter e_{RMS} can serve as a basis to calculate the digitalization specification parameters SINAD, ENOB and jitter as discussed next.

4.3.4 Receiver Self-Test and Specification of the Digitalization Accuracy

The manufacturers of analog-to-digital converters specify the characteristics in various parameters. Such parameters are most likely to differ from the parameters of the data converter in a specific application where the conversion process is more complex. This is the case in this borehole radar system.

A radar receiver has to cope with a high dynamic range where strong direct signals can cause occurrences of overmodulation. Such events affect the amplifiers as well as the analog-to-digital converters. The recovery from such overmodulation is described by the out-of-range recovery time. The recovery time can be measured with a test signal with a variable amplitude and adequate high dynamic range as the decaying sine wave signal in Equation (4.26).

The quality of the data conversion depend on all the components of the conversion. The overall accuracy can be determined similar to single ADC integrated circuits. Analog-to-digital converter testing is performed with several well defined input signals like sine waves to calculate parameters to characterize the overall sampling quality. In a radar application parameters as signal-to-noise ratio (SNR/SINAD), effective number of bits (ENOB) and out-of-range recovery are of importance. Examples and procedures for such parameters are defined among others in the IEEE standard 1241 [55].

A basic parameter of every data acquisition system is noise in the sense of total noise. Total noise is any deviation between the acquired signal and ideal expected input signal. A computation of the total noise of the digitizing system helps to distinguish between noise and wanted signal. This way the lowest detectable valid signal amplitudes can be defined.

Random noise errors can be measured by two subsequent measurements resulting in signals $\vec{v}$ and $\vec{w}$ containing each M number of samples. Both signals are subtracted and then the RMS value is calculated to result in the noise variance σ^2. The noise variance represents the random noise, because the ADCs fixed-pattern errors are eliminated. This data can be used for post-processing.

$$\sigma^2 = \frac{1}{2 \cdot M} \sum_{n=0}^{M} (v_n - w_n)^2 \tag{4.94}$$

The signal-to-noise and distortion ratio (SINAD) describes the ratio of the signal to the total noise of the conversion. The total noise $N_{\text{RMS,total}}$ can be calculated with the residuals of the recorded test signal, which involves subtracting the measured values $\vec{v}$ from the reconstructed ideal samples $\vec{u}$ in the time domain. The number of available samples is represented by M. The input amplitude of $\vec{v}$ is preferably close to the maximum of the input channel that means near full-scale to determine the effects of noise mechanisms such as slew rate limitations and digital ground noise.

$$N_{\text{RMS,total}} = \sqrt{\frac{1}{M} \cdot \sum_{n=0}^{M} (v_n - u_n)^2} \tag{4.95}$$

$$u_{\text{RMS}} = \sqrt{\frac{1}{M} \cdot \sum_{n=0}^{M} (u_n)^2} \tag{4.96}$$

$$\text{SINAD} = \frac{u_{\text{RMS}}}{N_{\text{RMS,total}}} \tag{4.97}$$

$$\text{SINAD}_{\text{dB}} = 20 \cdot \log\left(\text{SINAD}\right) \tag{4.98}$$

The effective number of bits (ENOB) compares the amount of noise produced by digitalization and an ideal analog-to-digital conversion process. The value for ENOB can be calculated from the SINAD value when using a full scale input signal with Equation (4.99).

$$\text{ENOB} = \log_2\left(\frac{\text{full scale range}}{\text{noise}_{\text{rms}} \cdot \sqrt{12}}\right) \tag{4.99}$$

An adjustment is needed for signal amplitudes below the full input scale [55]. The adjustment noted in Equation (4.100) as ENOB′ adds ENOB bits of the difference of input amplitude and full scale input without considering noise. As a result, the ENOB′ value is mostly higher the lower the signal amplitude is due to decreasing conversion errors.

$$\mathrm{ENOB}' = \log_2(\mathrm{SINAD}) - \frac{\log_2(1.5)}{2} - \log_2\left(\frac{\text{input signal amplitude}}{\text{full scale amplitude}/2}\right) \tag{4.100}$$

A method to measure sampling jitter presented in an application note [48] uses two signal frequencies. The first sine wave with a low frequency is used to measure the average differential nonlinearity (DNL) including other minor noise sources and thereafter a high frequency sine wave is used to calculate the aperture uncertainty in reference to the DNL error. As a result, the degraded data conversion quality due to the difference in signal frequency is measured. Such errors can be combined as sampling jitter.

The equation for the calculation is based on Equation (4.18) where a term for differential nonlinearity e_{DNL} is added as noted in Equation (4.101). The resolution of the converter in bits is represented by Z and the test signal frequency by $\omega = 2 \cdot \pi \cdot f$.

$$\mathrm{SNR}_{\mathrm{dB}} = -20 \cdot \log\left(\sqrt{(\omega \cdot \Delta t_{\mathrm{RMS}})^2 + \left(\frac{1 + e_{\mathrm{DNL}}}{2^Z}\right)^2}\right) \tag{4.101}$$

This method also can be used using test signal with different amplitudes, because a lower amplitude has a lower slew rate consequently resulting in less noise caused by aperture uncertainty (Figure 4.17). The first measurement with a low amplitude is the reference measurement where the SNR value is calculated without the harmonics of the test signal. Moreover, it is assumed that there are no additional errors due to sampling jitter effects. The value for e_{DNL} can then be calculated as shown in Equation (4.102).

$$e_{\mathrm{DNL}} = 2^Z \cdot 10^{-\frac{\mathrm{SNR}_{\text{low amplitude}}}{20}} - 1 \tag{4.102}$$

The next measurement is conducted with the same test signal with an amplitude close to the maximum range of the converter. This will result in higher noise due to increased sampling jitter effects. The SNR is calculated again without the harmonics of the test signal. The sampling jitter Δt_{RMS} can be calculated with the measured SNR and value for e_{DNL} as in Equation (4.103)

$$\Delta t_{\text{RMS}} = \frac{1}{\omega} \cdot \sqrt{\left(10^{\frac{-\text{SNR}_{\text{high amplitude}}}{20}}\right)^2 + \left(\frac{1 + e_{\text{DNL}}}{2^Z}\right)^2} \tag{4.103}$$

The equation above can be rewritten as in Equation (4.104) including two measured SNR values. The first first $\text{SNR}_{\text{high amplitude}}$ value is calculated for the beginning of the test signal, resulting in higher jitter related errors. In contrary the second value $\text{SNR}_{\text{low amplitude}}$ is computed for low amplitudes including only the last samples of the test signal containing only little jitter errors.

$$\Delta t_{\text{RMS}} = \frac{1}{\omega} \cdot \sqrt{\left(10^{-\frac{\text{SNR}_{\text{low amplitude}}}{20}}\right)^2 + \left(10^{-\frac{\text{SNR}_{\text{high amplitude}}}{20}}\right)^2} \tag{4.104}$$

The precision of the presented method depends primarily on the computed SNR values. After all, this measured parameter gives a good estimation and can be used to compare different versions of the radar receiver under different conditions.

The specification of the digitalization is one application for the test signal generator. Moreover, it is used for calibration to improve measurement results. In general these calibration processes can be basically classified into a couple of methods.

4.3.5 Receiver Calibration Methods

Two basic calibration principles are “offline” and “online” correction methods. When performing an “online” calibration the correction parameters are modified before the actual measurement. After completing the correction parameter adjustments, the radar measurements can be performed.

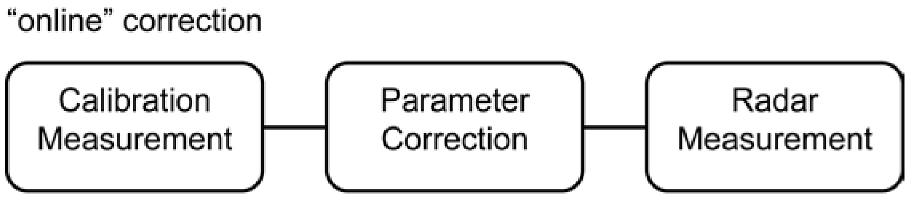

Figure 4.35: “Online” calibration.

Data correction can be accomplished after the actual radar measurement when calibration data is available. This correction method is an "offline" procedure. The data adjustment can be made at a convenient time with software on any computer with sufficient computer power. In particular, such method gives more flexibility than "online" correction.

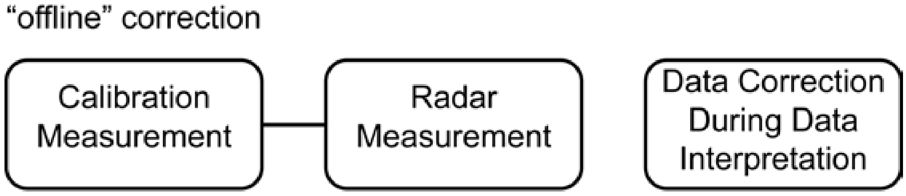

Figure 4.36: "Offline" calibration.

The decision to either use "online" or "offline" correction depends on the particular calibration task. The two major calibration tasks are

- correction of systematic sampling errors
- gain factor matching for all channels

The channel matching calibration task adjusts primarily amplitudes. A scaling factor has to be assigned to each channel. This can be achieved simply in an "offline" calibration when calibration data is available for all channels.

Interleaved sampling errors lead to non equidistant sample intervals. These intervals could be measured and added as correction parameters to the measurement data. This type of "offline" correction is not very practical because it is difficult to process data with non equidistant distributed samples. Furthermore the measurement of these systematic timing errors is a difficult task. Therefore an "online" correction for systematic interleaved sampling errors is required.

4.3.5.1 Detection and Correction of Systematic Interleaved Sampling Errors

Aperture uncertainty, clock jitter and transmitter timing uncertainties causes sampling errors in the analog-to-digital conversion process. These linked error sources result in additional data conversion noise. The noise levels are significantly higher for high sampling clock uncertainties Δt like illustrated in Figure 4.19.

In an interleaved sampling system, such time-base instability can contain systematic errors additional to other noise sources like Gaussian random noise. A well defined narrowband test signal helps to detect these sampling related systematic errors in the time domain or frequency domain. When using the frequency domain, sampling clock problems are indicated by subharmonic sidebands in relation to the sampling clock as shown in the next example.

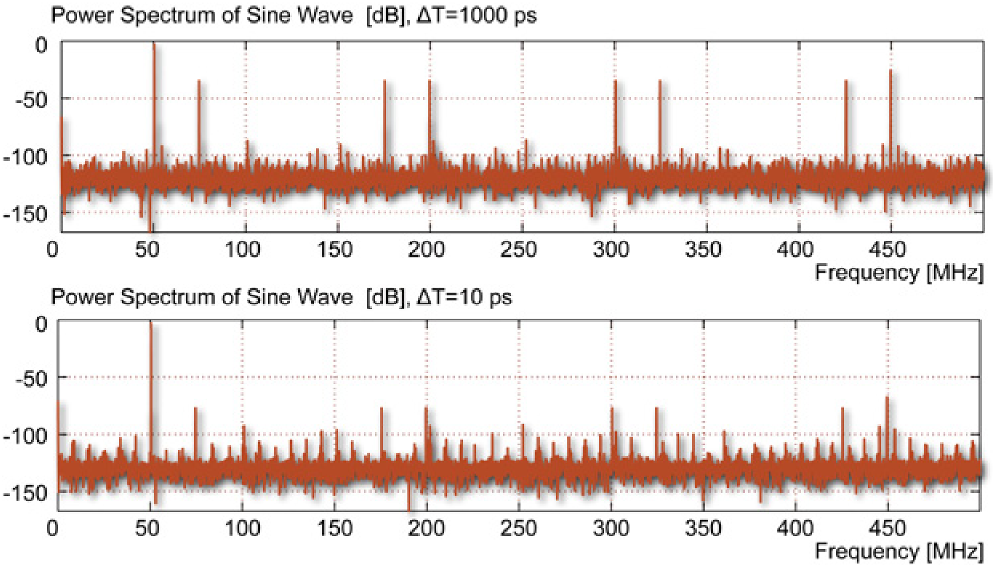

Figure 4.37: Simulated frequency spectrum of a sine wave with systematic interleaved sampling errors (top) and minimized errors (bottom).

Figure 4.37 compares a sampled signal containing exceeding systematic sampling errors ΔT against a signal with minimal systematic time uncertainties. In both simulations a $f_{\text{test signal}} = 50$ Mhz sine wave was used as an input signal. The effective sampling rate is 1000 MSPS with 8 interleaved sampling sweeps with a sampling clock of $f_{s,\text{ADC}} = 125$ MSPS. The simulated data converter is an AD9246 [54].

The systematic interleaved sampling sweep errors effect every trigger signal. It results in subharmonics sidebands of the effective sampling clock frequency. This effect looks similar to the consequence of sub-sampling. Figure 4.37 contains distinct characteristic spurs which are listed along with the calculation in Table 4.3.

The process of minimizing sampling errors reduces unwanted spurs in the frequency spectrum of the test signal. This optimizing can be performed by an online calibration process where the parameters of the digitalization process

Signal Spur	**Spur Origin**
75 MHz	$1 \cdot f_{s,\mathrm{ADC}} - f_{\mathrm{testsignal}}$
175 MHz	$1 \cdot f_{s,\mathrm{ADC}} + f_{\mathrm{testsignal}}$
200 MHz	$2 \cdot f_{s,\mathrm{ADC}} - f_{\mathrm{testsignal}}$
300 MHz	$2 \cdot f_{s,\mathrm{ADC}} + f_{\mathrm{testsignal}}$
325 MHz	$3 \cdot f_{s,\mathrm{ADC}} - f_{\mathrm{testsignal}}$
425 MHz	$3 \cdot f_{s,\mathrm{ADC}} + f_{\mathrm{testsignal}}$
450 MHz	$4 \cdot f_{s,\mathrm{ADC}} - f_{\mathrm{testsignal}}$
$\geq$ 550 MHz	spurs not in displayed range

Table 4.3: Unwanted frequency spurs caused by systematic trigger errors.

are corrected through fine adjusting the transmitter trigger pulse delay before the actual measurement data is recorded. The trigger delay for each interleaved sampling interval has to be fine adjusted in regard to the sampling clock for minimal errors.

This calibration process can be performed manually by correcting every single interleaved sampling sweep trigger delay value and verifying the result in the measured signal spectrum. Another possibility is to implement an algorithm to compute the parameters of a test signal by successive approximation. Such an algorithm has to be similar to the manual process where the unwanted signals in the frequency spectrum are measured and the adjustment is made accordingly.

Another important calibration task is to obtain the relative amplitudes of the three input channels for different amplifier settings.

4.3.5.2 Calibration of Different Amplifier Settings

The calibration signal has to be suited to match signals measured with different amplification settings. Additionally, the gain variations of the different input channels can be corrected. This is an important process because the absolute gain error is in a range of a few decibels whereas the channel-to-channel matching of a variable gain amplifier like the AD8332 [35] is in a range of ±1 dB. Moreover, the error of the digital-analog-converter which is used to control the gain control voltage is added to the amplifier tolerances.

The relative gain levels can be defined by measuring the same reference signal at the same time at the three input channels. A sine wave with a fixed amplitude and frequency in the input range is sufficient. In a case of a more complex digitalization circuit and complex input signals, the accuracy differs with the signal level and frequency as was further explained in section 4.3.4. Therefore a suited test signal has to supply a reference for the whole dynamic range of the input channel for suitable accuracy.

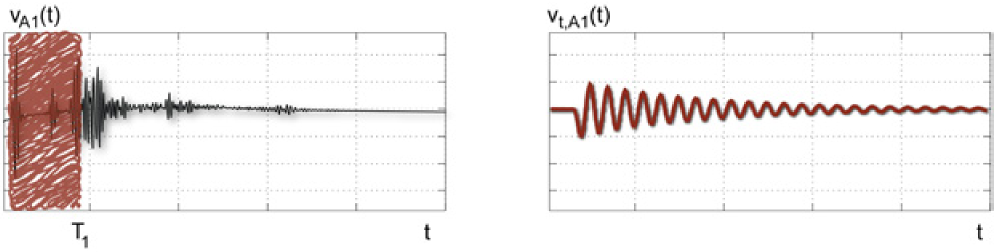

Figure 4.38: Radar and calibration measurement with low gain setting A_1.

The process of gain calibration involves that each measurement is conducted with a signal from the antenna and additionally, from the calibration signal generator. Adaption parameters can be calculated with the help of the calibration measurements and thereafter it is possible to assemble a new signal from multiple measurements recorded with different amplification settings.

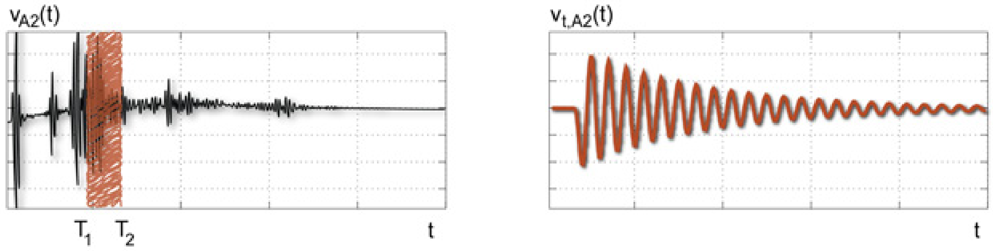

Figure 4.39: Radar and calibration measurement with medium gain setting A_2.

The first measurement in this example is conducted with a low gain setting and is depicted in Figure 4.38. The left side shows the radar measurement and the right side shows the test signal measurement with the same settings. The next measurement window in Figure 4.39 uses a medium gain value.

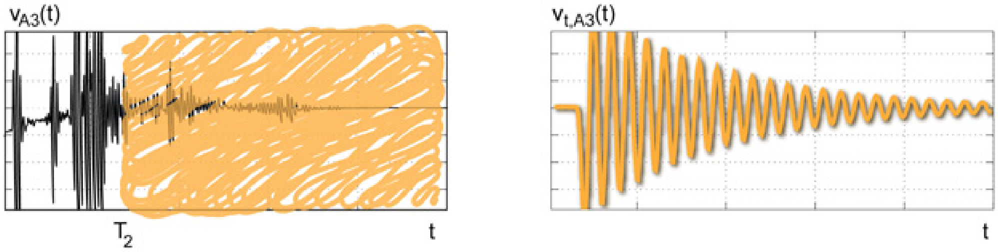

Figure 4.40: Radar and calibration measurement with high gain setting A_3.

High gain values lead to overmodulation and consequently the signal is invalid until the signal is in the input channel range and the receiver is recovered as it is shown in Figure 4.40. The valid part of the signal which can be used is marked. The relative amplification factor can be calculated with the suggested test signal shown on the right side.

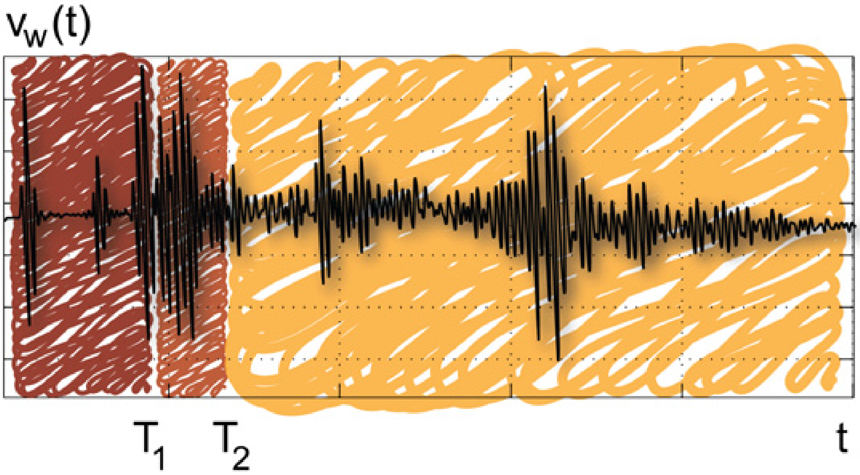

Figure 4.41: Assembled radar trace with calibration signal parameter fitting.

The fitted result $v_w(t)$ is assembled with the estimated test signal amplitudes A_1, A_2 and A_3.

$$v_w(t) = \begin{cases} v_{A1}(t)/A_1, & \forall\, t \leq \mathrm{T1} \\ v_{A2}(t)/A_2, & \forall\, \mathrm{T1} < t \leq \mathrm{T2} \\ v_{A3}(t)/A_3, & \forall\, t > \mathrm{T2} \end{cases} \tag{4.105}$$

The result of assembling the three separate measurements by parameter fitting is illustrated in Figure 4.41. Different sections from the three separate measurements with different amplifier settings are exactly matched. This windowing technique helps to avoid amplifier overdrive in relevant signal sections expanding the dynamic range.

4.3.5.3 Calibration Improves Direction Estimation

The two loop antenna channels are used to estimate the direction of the incoming echoes. The accuracy of the calculated angle depends on the loop channel matching. The angle of the incoming echo signal φ can be in principle calculated with the voltages of the loop channels v_{loop1} and v_{loop2}:

$$\varphi = \arctan\left(\frac{v_{\text{loop1}}}{v_{\text{loop2}}}\right) \cdot \frac{180}{\pi} \tag{4.106}$$

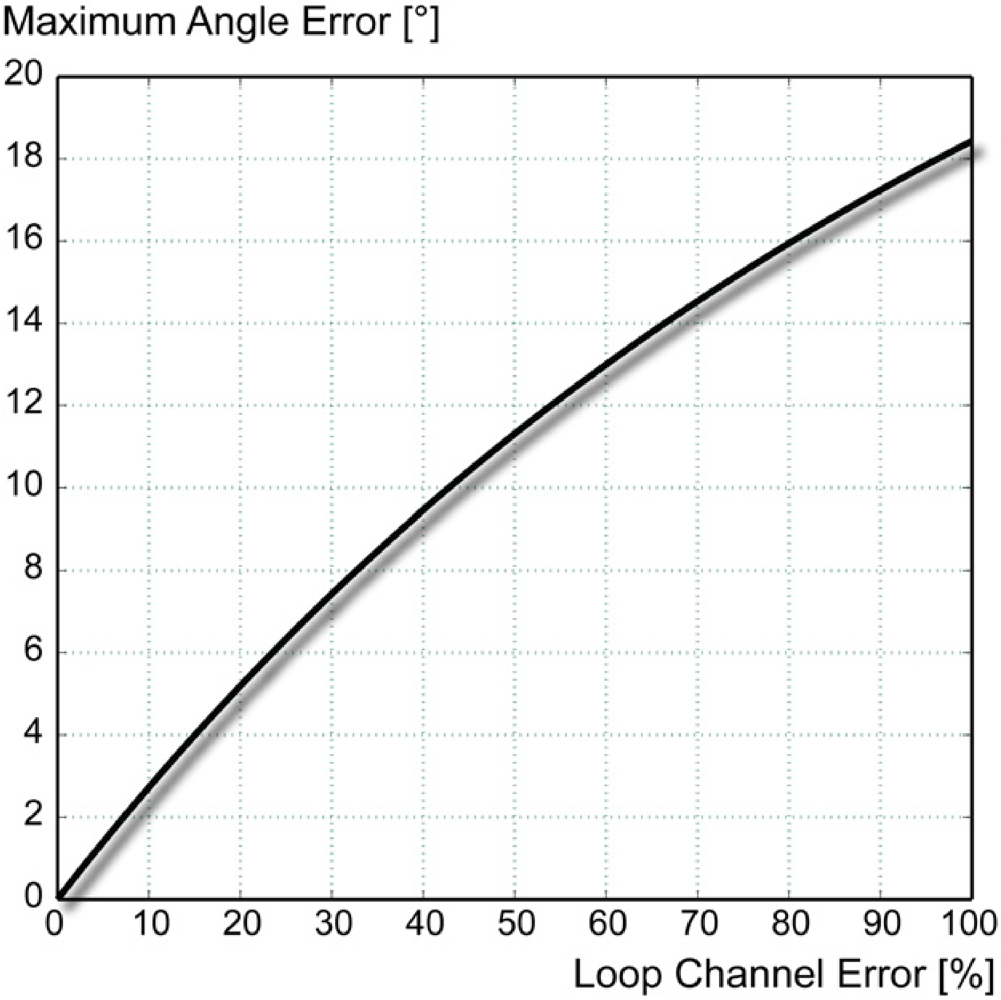

Figure 4.42: Maximum angle error depending on the error between the loop channels in percent of the amplitude.

The error in one channel is in a maximum for $v_{\text{loop1}} = v_{\text{loop2}}$. A variation in one channel causes an error in the detected angle φ as shown in Figure 4.42 for an error expressed in percent of channel v_{loop1}.

In conclusion we can say that relatively small expected channels errors in an uncalibrated system cause angle errors of 0.25° per % error. A calibration of the loop channels including the amplifiers and antennas can reduce this error.

The considerations and research contained in this chapter was put into an electronic design of a borehole receiver which is presented in the next chapter.

The introduced methods and test signals are used to specify the sampling quality of the designed borehole radar and will be put into practice when discussing the measurement results.

5

Receiver Implementation

A borehole radar system was implemented according to the conclusions of the previous chapters, with primary focus on the radar receiver. This section presents the hardware design beginning with the overall receiver design. Thereafter selected core blocks are discussed in more detail.

5.1 Borehole Radar Receiver Overview

The borehole radar receiver electronics consists of several blocks and processes as discussed in section 3.2 and illustrated in the block diagram 5.1.

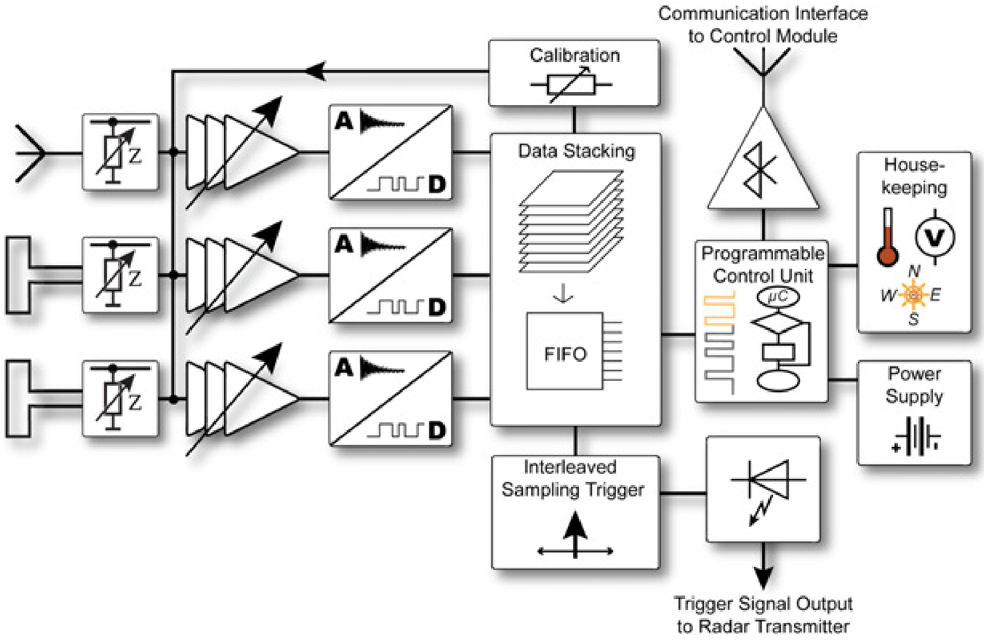

Figure 5.1: Borehole radar receiver block diagram.

Each receiving antenna is connected to one separate input channel. Accordingly all three channels are recorded in parallel at the same time, thus reducing measurement time. Such an input channel contains an antenna matching circuit and a variable gain amplifier with good clamping capabilities. The output of each amplifier is connected to an ADC.

The acquired digital data is stored and averaged by a data stacking block to improve the signal quality and dynamic range. The data stacking unit is located inside a field programmable gate array (FPGA) and includes the measurement state machine which controls the interleaved sampling to achieve the best possible synchronization. The trigger signal is generated by the interleaved sampling control and sent to the transmitter unit via fiber optic cable, providing required electrical isolation.

A microcontroller is used as a programmable control unit supervising the receiver electronics. The advantage of a microcontroller controlling the receiver instead of an existing FPGA is the much lower power requirement and simple deployment. Consequently it is used to switch components off and on in order to control the receivers electrical power consumption. Moreover, the microcontroller reads internal temperature sensors, condition of the power supply, data from the orientation module and communicates with the FPGA.

This microcontroller communicates with the control module located a few meters away by Bluetooth, in order to avoid any interfering conductive cables as discussed in detail in section 4.1. In contrast, the frequency range of the Bluetooth transceiver does not interfere with the input bandwidth of the radar receiver. The advantage of the wireless connection over an optical link is the convenience that no susceptible connectors are needed.

The theoretic overall dynamic range can be estimated with the properties of the components in the antenna signal path. The ADC [44] has a range of 72.4 dB, the amplifier of 55.5 dB [35] and 1000 times stacking can add another 30 dB (Equation (4.6)). These numbers result in a theoretic dynamic range of 157 dB.

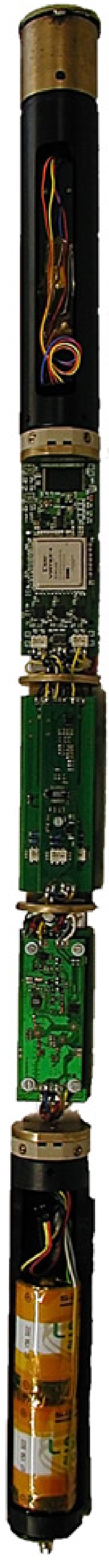

Figure 5.2: Receiver core.

In the practical application the dynamic range is by factors as the noise floor present and limited usable amplifier gain.

The digitalization unit, as designed in the previous chapter, used to sample the antenna signals consists of the ADCs, data stacking block and the interleaved sampling trigger control. These core blocks for receiving and processing the ADC data are implemented inside the FPGA.

5.2 Digitalization Structure

The digitalization subsystem is based on a field programmable gate array (FPGA) to retrieve and process the ADC data. Such an approach saves board space and keeps the design flexible, because the digital logic inside the FPGA can be easily reprogrammed. Moreover the critical sampling timing of the trigger output is controlled by the FPGA containing a digital clock manager (DCM). A low noise clock oscillator provides the time base for the ADCs and the FPGA as depicted in the block diagram 5.3.

The implemented interleaved sampling operation requires an adjustable phase shift of the radar signal and ADC clock. This can be achieved by finely adjusting the ADC clock or using an adjustable trigger delay. However, to minimize the jitter influence of the DCM unit the phase shift is implemented with the trigger signal output.

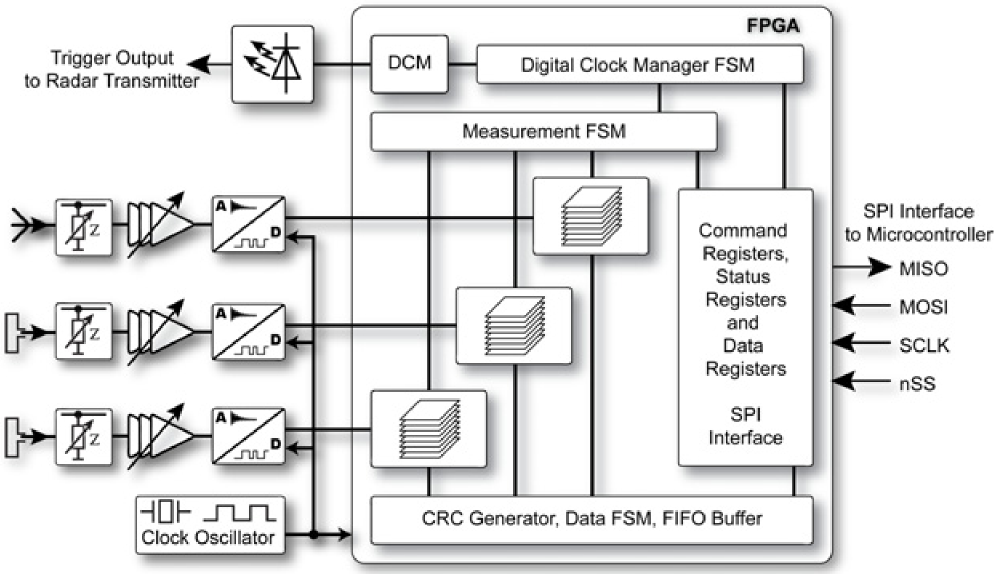

Figure 5.3: Digitalization and FPGA block diagram.

The digital clock manager inside the Xilinx FPGA [50] contains a delay-locked loop (DLL) to eliminate clock distribution delays. Additionally, an integrated programmable delay line provides fine-grained phase-shifting of up to 10 ns with a resolution of $\pm\frac{1}{256} \cdot T_{\text{clock}}$ where T_{clock} is the FPGA input clock. Possible temperature changes and voltage variations are calibrated for delay tap timing internally.

Unfortunately an extra amount of jitter is added by the DCM to the trigger signal. The added jitter is according to the Xilinx Virtex-4 datasheet 250 $\text{psec}_{\text{peak-to-peak}}$ [50]. This added jitter is insignificant compared to the jitter of the pulse transmitter which equals approximately 5000 $\text{psec}_{\text{peak-to-peak}}$, according to the measurement data in Figure 4.13.

The digital clock manager is able to shift the transmitter trigger signal in steps of $\frac{1}{256} \cdot T_{\text{clock}} = \frac{1}{256 \cdot 125\ \text{MHz}} = 31.25$ psec relative to the system clock that equals the ADC clock. Each ADC is connected to an individual stacking memory used for data averaging. These internal memories are implemented as first in, first out (FIFO) memory controlled by a state machine for coordinating the measurements. During readout of these memories, checksum and channel identification words are added while data is transmitted to the microcontroller.

The communication between FPGA and microcontroller uses a serial peripheral interface (SPI) with data rates of up to 10 Mbit/sec to access the internal control, data and status registers.

The FPGA registers are used to configure the measurement parameters and execute commands. Each individual measurement receives the data of one interleaved sampling interval where the relation of trigger signal and ADC clock is set by a timing parameter. Therefore the number of individual measurements per position depends on the configured effective sampling rate in the measurement software. The full control of the digital sampling process is implemented in the PC software connected to the probe.

The FPGA can be loaded with different configurations in between measurements to allow alternative measurement methods and multiple radar techniques. The number of the selectable configurations by the microcontroller is up to four, depending on the PROM connected to the FPGA. This option creates a flexible platform for different signal processing options.

The digitalization quality can change in different environmental conditions. Therefore the calibration unit includes a test signal generator to monitor and correct sampling results.

5.3 Test Signal Generator and Calibration Module

The calibration unit contains the test generator and signal switches to include the options proposed earlier, such as the test of the digitalization process or channel matching. The basic circuit used to generate the test signal is a parallel resonant circuit containing a capacitor, an inductor and a resistor. This resonant circuit generates the test signal according to Equation (4.90) when triggered by a current source. The signal quality is of importance and therefore signal overshoots and switching noise have to be avoided. Moreover short term stability of the test signal during the measurement a single probe location, including the calibration process, is necessary.

The parallel resonant circuit needs to be excited by a stable current source. In order to prevent transient effects, the current source needs to be powered well before a test signal is triggered. Therefore a selector switch is needed to either bypass the current source to ground or connect it to the resonant circuit (Figure 4.32). Such a current switch has to be designed for preventing signal overshoots and switching noise.

5.3.1 Current Switch Design to Prevent Switching Transients

The switch circuit design, along with the type of electronic parts, affect the switch characteristic. The required switch consists of one input signal and two controlled signal paths.

One of the major sources of switching noise is parasitic capacitance. Consequently the switch structure and selected parts have to have a low parasitic capacitance between the input control signal and the controlled signal path.

An examination of datasheets of several different FET and bipolar transistors helps to decide for the parts with lower capacitance. The capacitance between the control input (gate or base connection) and output channel (drain-source or collector-emitter) causes switching crosstalk. The capacitance of field effect transistors between gate input and output channel is in a range of 100 pF depending on the technology and size of the channel. On the contrary bipolar transistors for high frequency applications have only parasitic capacities of below 1 pF (e.g. transistor BFT92 [60]: $C_{\mathrm{BC}} = 0.75$ pF, $C_{\mathrm{BE}} = 0.8$ pF).

The electrical current flowing through these parasitic capacitors causes unwanted transients. Generally this switching noise can be calculated when considering the slew rate of the switch input signal V_s. Equation (5.1) shows that an increase in a capacity of 100 results in a same factor higher electrical current.

$$I_C = C \cdot \frac{\mathrm{d}\ V_s(t)}{\mathrm{d}\ t} \tag{5.1}$$

For this reason it is important to keep parasitic capacitances low. Nevertheless the required input switch voltages must be limited as well. Assuming a capacity of 1 pF and an input signal slew rate of 1 $\frac{\mathrm{V}}{\mathrm{nsec}}$ the resulting crosstalk current is 1 mA as noted in Equation (5.2). This current cannot be ignored, because it is in the order of the current source $I_0 \approx 1.2$ mA.

$$I_C = 1\mathrm{pF} \cdot 1\frac{\mathrm{V}}{\mathrm{nsec}} = 1\ \mathrm{mA} \tag{5.2}$$

The advantage of bipolar transistors despite the lower capacity values is their structure. There are only two parasitic capacitors: one between base and collector and another one between base and emitter. In contrary, a FET has three parasitic capacitors, one more than a bipolar transistor. The extra capacity results from the directly coupled drain and source connections. As a result bipolar transistors will be used in the design of the current switch.

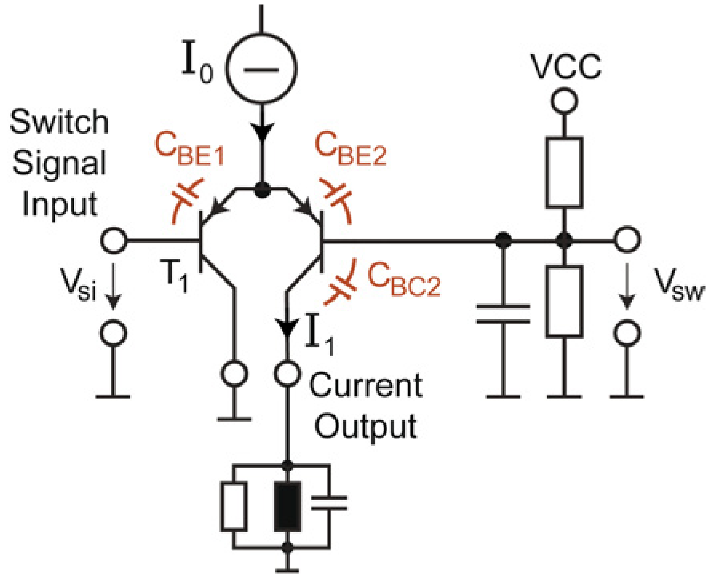

Figure 5.4: Transistor configuration for a current switch.

The implemented differential switch is illustrated in Figure 5.4. The differential amplifier is used to switch the current I_0 between ground and the resonant circuit. As soon as the differential voltage $V_{\mathrm{si}} - V_{\mathrm{sw}}$ is higher than 5 V_T the current is switched to the resonant circuit where V_T is the temperature voltage of the transistor at room temperature. The switch voltage level V_{sw} in regard to the switch input signal is set by a buffered voltage divider.

The first advantage of this structure is the low differential voltage required for switching of a minimum of approximately $5\ V_T \approx 100$ mV [61]. Consequently a low voltage can produce only low switching noise. The second advantage is a long signal path of the switching noise which includes the parasitic capacitors C_{BE1} and C_{BE2}. Thereafter the switching noise is bypassed by the voltage divider and the additional capacitor.

The current switch is a critical component in the test generator as well as the decoupling of the test signal from the resonant circuit to feed the signal to the input channels.

5.3.2 Resonant Circuit Signal Coupling

The resonant circuit has to be decoupled by an amplifier with high input impedance to achieve least influence of the resonant circuit itself. Additionally, the resonant circuit is loaded by a voltage divider made up of two resistors. The circuit reduces the quality factor Q resulting in a higher damping factor causing a shorter oscillation.

The quality factor Q is the ratio of the energy stored divided by the energy lost in the resonant circuit. It determines the length of the oscillation which has to be limited to the available data recording time. Another benefit of the resonant circuit load is that an amplifier with high impedance has no influence on the relative low impedance of the connected load.

The quality factor Q can be calculated for a parallel resonant circuit with Equation (5.3).

$$Q = R \cdot \sqrt{\frac{C}{L}} \tag{5.3}$$

A test signal frequency of approximately 50 MHz can be generated by using a parallel resonant circuit with $L = 150$ nH, $C = 68$ pF and total $R = 670\ \Omega$. The resulting oscillation is damped and meets the constraint of Equation (4.35) as shown below in Equation (5.4).

$$Q = 670\ \Omega \cdot \sqrt{\frac{68\ \text{pF}}{150\ \text{nH}}} = 14.3 \tag{5.4}$$

The parameter τ can be calculated using equations (4.32), (5.3) and (5.5).

$$\tau = 2 \cdot Q^2 \cdot \frac{L}{R} = 2 \cdot 14.3^2 \cdot \frac{150\ \text{nH}}{670\ \Omega} = 91 \cdot 10^{-9}\ \text{sec} \tag{5.5}$$

$$\omega_0 = \sqrt{\frac{1}{L \cdot C}} = \sqrt{\frac{1}{150\ \text{nH} \cdot 68\ \text{pF}}} = 313.1 \cdot 10^6\ \frac{1}{\text{sec}} \tag{5.6}$$

The above numbers show that the constraint $\frac{1}{\tau} < \omega_0$ for a damped oscillation resulting in

$$11 \cdot 10^6 \frac{1}{\text{sec}} < 313 \cdot 10^6 \frac{1}{\text{sec}} \tag{5.7}$$

is met.

The components analyzed above are embedded in the test generator which is explained further in the following section.

5.3.3 Test Signal Generator Block Diagram

The entire test generator itself has several functional components as illustrated in Figure 5.5 whereas a more detailed schematic is provided in the Appendix A.

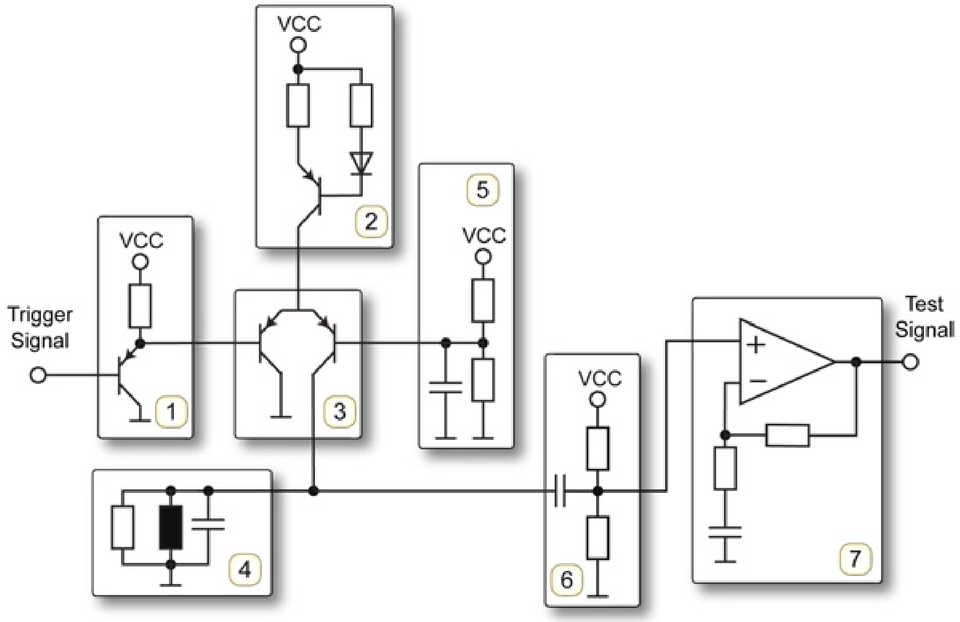

Figure 5.5: Test signal generator block diagram.

The trigger signal coming from the FPGA is connected to an impedance converter (1) providing a high input impedance and adding the basis-collector voltage of the transistor as an offset voltage. A current source (2) feeds the parallel resonant circuit (4) which is used to produce the test signal. This current source can be switched between ground and the resonant circuit (4) using a differential amplifier (3) where the switching voltage is controlled by the offset of the voltage divider (5). The transient test signal is generated whenever the constant current source (2) is switched to or from the parallel resonant circuit (4).

The resonant circuit (4) is decoupled by a capacitor and voltage divider (6) which provides additional damping of the resonant circuit. The resulting voltage swing around the offset voltage (6) is amplified and filtered by an operational amplifier (7). The amplifier is configured as non-inverting with high pass filtering.

The short term stability is achieved by using no additional frequency sensitive parts in the signal path of the constant current source and resonant circuit. Nevertheless the parameters of the test signal may change over time where the time is in an order of minutes or hours. Consequently these relative long term changes can be monitored with a test signal which is stable for a short term.

The test signal can be selectively switched to the antennas for additional calibration and test possibilities.

5.3.4 Test Signal Switch Options

The test and calibration process should acquire as much information about the receiver electronics and antenna properties as possible. These capabilities are implemented by using switches for different test signal connections as illustrated in Figure 5.6.

The switch signal SW1 is used to connect the loop antennas to the test signal generator and decouple the dipole antenna from the data acquisition input channel. The switch controlled by SW2 connects the test signal to the dipole amplifier input. Additionally, attenuators are added to the test signal path to set different signal levels for the dipole channel and loop antenna inputs.

The test signal can be switched to the dipole antenna while the loop antennas receive the test signal transmitted by the dipole antenna setting SW1=off

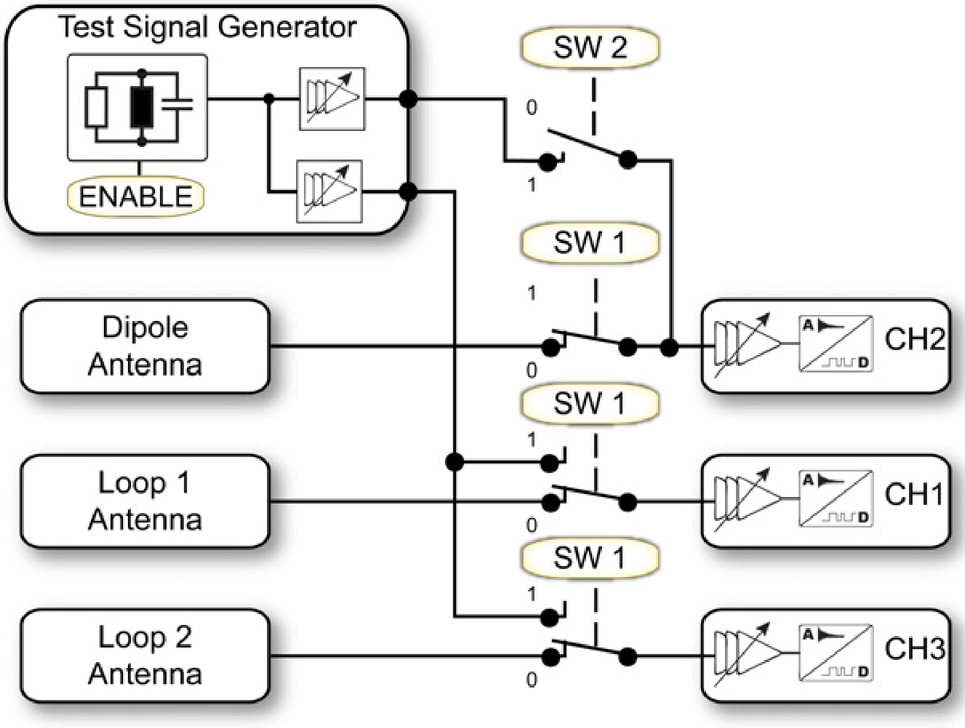

Figure 5.6: Connection options for the test signal generator.

and SW2=on. This feature enables channel symmetry testing and data correction with the same test signal generator. Moreover, the environmental dependent antennas properties can be analyzed and calibration data can be obtained.

The test signal generator can be switched off entirely by the microcontroller to save energy using the ENABLE signal. The different available power modes are activated by the data acquisition software. Such an option keeps the receiver flexible although it requires fast data transmission speeds over a relative long distance.

5.4 Data Transmission and User Interface

The borehole radar receiver is connected to the control computer over a wireline logging cable with a length of up to a few kilometers where the cable quality is low in most cases. Consequently data transmissions speeds are generally low. At the same time this receiver is controlled by the data acquisition software on the control computer and therefore requires fast data transmission speeds to achieve short measurement times. Accordingly, the communication link has to provide low latency times along with a high data rate while using electrical low quality transmission lines.

5.4.1 Data Transmission

The data transmission from the receiver to the data acquisition software involves several components as depicted in Figure 5.7. The acquired data is transmitted over a wireless Bluetooth connection to the control module. This link doesn't interfere with the measurement, because it operates with 2.4 GHz well above the radar receiver frequency bandwidth. The advantage of a wireless link is the simple handling of the separate borehole probe modules without any connectors as needed with an optical link. After all, such connectors are susceptible to dirt and mechanical damage.

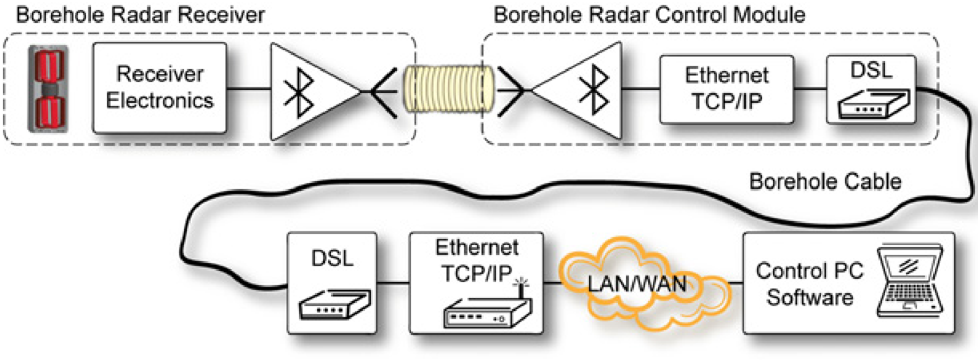

Figure 5.7: Receiver communication link to the data acquisition computer.

The control module contains an interface to connect the Bluetooth 1.2 transceiver [62] to an Ethernet adapter with TCP/IP networking functions. A pair DSL (digital subscriber line) modems provide a fast and reliable link over the borehole cable to the local network. The local network in turn provides the connection of data acquisition computer to the borehole probe. The use of the TCP/IP network protocol enables access to the borehole probe over the Internet. The Internet connectivity makes collaborate measurements together with remote diagnostics possible. Accordingly further development and radar probe deployment can safe time with this technology.

The data transmission speed over DSL modems can be as fast as 1 to 2 MBit/sec whereas the Bluetooth connection transfers data at a rate of about 500 kBit/sec. In fact, the Bluetooth link reduces the overall data transmission rate. Moreover the transfer protocol overhead of approximately 20 % adds extra data. In the end the transfer time for one interleaved sampling sweep of 1024 data words with a data width of 24 Bit can be calculated as in Equation (5.8).

$$T = 1024 \cdot 24 \text{ Bit} \cdot \left(500 \, \frac{\text{kBit}}{\text{sec}}\right)^{-1} \cdot 1.2 = 0.6 \text{ sec} \tag{5.8}$$

Consequently, the total time from starting the measurement until the data is available at the operators user interface is several seconds depending on the measurement options selected.

5.4.2 User Interface

The user interface for the borehole radar receiver is implemented in a computer running Linux or a Microsoft Windows operating system. The command interface to the probe requires only a few steps to acquire the measurement data. Therefore it was possible to develop two different software programs to control the borehole probe. The first operating software uses the software package Matlab and specialized software for the probe communication whereas the second software is a native application.

5.4.3 Software for Test Signal Parameter Estimation

A software module was designed to evaluate the test signal and provide a characterization of the digitalization process. The test signal parameter computation contains several steps as illustrated in Figure 5.8. At first, the provided signal is analyzed and the test signal is detected. Then the frequency is estimated by using the frequency spectrum. Thereafter the decaying constant τ is estimated. Next, the other three parameters amplitude, phase and DC offset are computed using a linear fitting algorithm. These estimated parameters are start values for an iterative fitting algorithm where the frequency ω is iterated and the parameters A, ω, φ and DC are calculated. As a last step the parameter τ is determined by using non-linear least square fitting.

The fitted parameters of the test signal compare the measured signal with an ideal test signal. This comparison results in the residuals which can detect functional errors in the receiver.

The parameter fitting algorithm was implemented in the software package Matlab with the possibility to rewrite the algorithm in a different programming language like C/C++. The source code is included in appendix A.

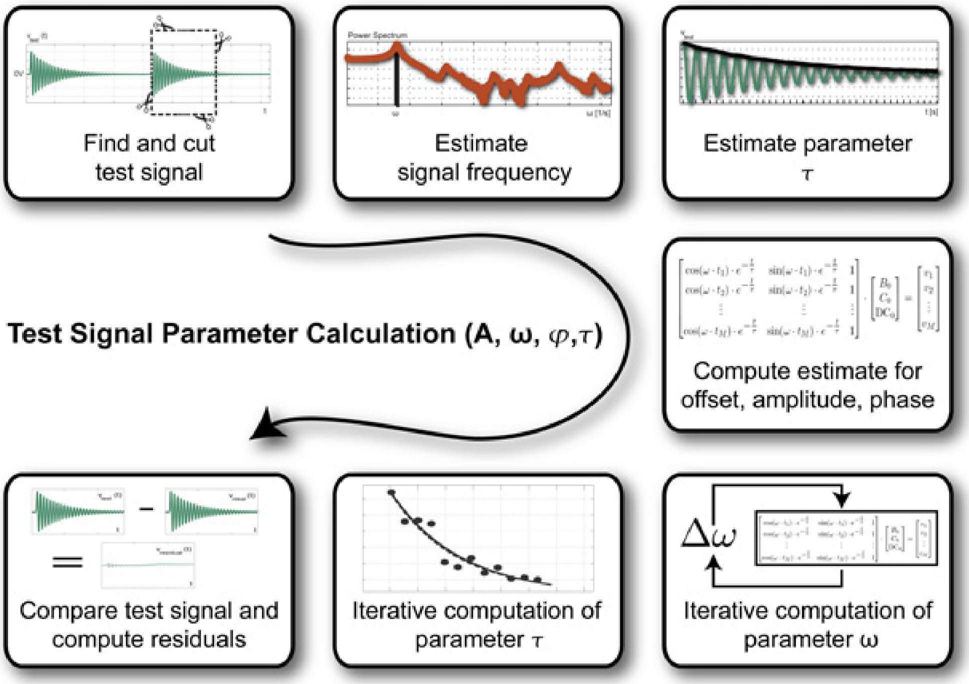

Figure 5.8: Block diagram of test signal parameter estimation.

5.5 Electrical Power Requirements of Radar Receiver

The low power requirements of the receiver are important to ensure a long operating time with one set of batteries. In order to minimize the power consumption the components have to be evaluated as illustrated in block diagram 5.9. Some of the component are vital for communication and system functions whereas others modules are only needed during measurements or calibrations.

The microcontroller as programmable control unit and supervisor controls the power modes and therefore cannot be switched off at any time. Moreover the communication to the control module, using a Bluetooth link, has to be available to access the receiver at all times. In contrast, the amplifiers, FPGA, test signal generator and some system monitoring devices can be switched off when not needed. Further analysis for power on and power off cycle times is needed to plan power on cycles and calculate an average power requirement.

Table 5.1 lists the power consumption of the components along with the time to power each individual module.

The time needed to power up some of the components like FPGA or the orientation module is rather long where at the same time other components

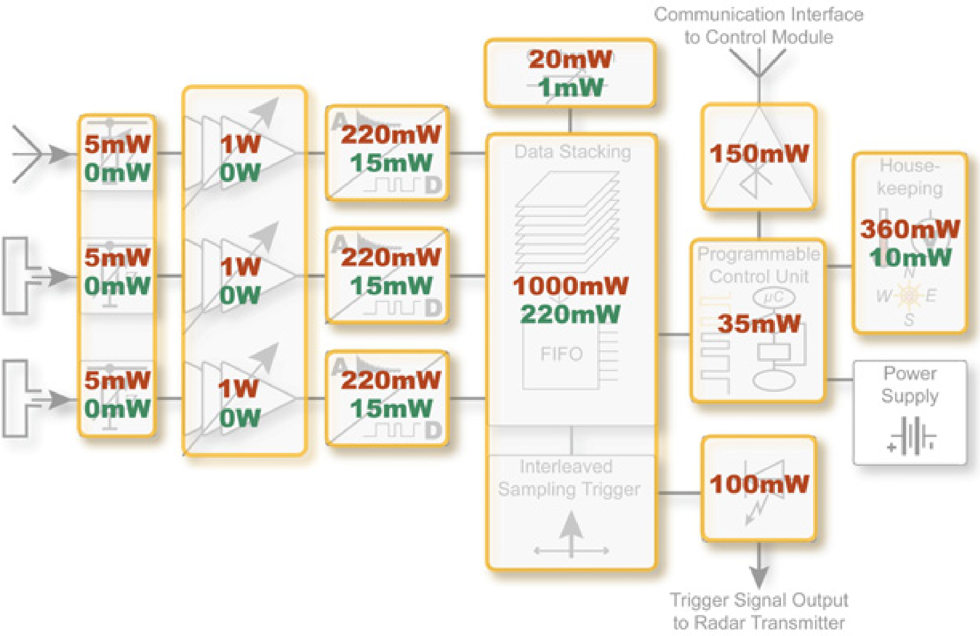

Figure 5.9: Power requirements of individual receiver components.

Component	**Power Up**	**Power Down**	**Power Up Time**
Antenna Adaption	5 mW	0 mW	10 msec
Amplifier Block	3000 mW	0 mW	10 msec
A/D-Converters	660 mW	45 mW	1 μsec
Bluetooth Module	150 mW	0 mW	500 msec
FPGA	1000 mW	220 mW	500 msec
Orientation Module	350 mW	0 mW	>1 sec
Test Generator	20 mW	0 mW	1 μsec

Table 5.1: Power requirements for receiver components in power up/down modes.

can be turned off and back on quite fast. The timings need to be considered when designing the different power modes of the receiver. Components with similar wake up times can be combined together resulting in three different power operating modes:

1. deep sleep mode - wake up time in order of seconds
2. power down mode - wake up time in order of milliseconds
3. power up mode - all systems are powered for measurement operation

The most energy is obviously needed in “power up” mode during measurements. The opposite is true for the “deep sleep mode” where only the essential communication blocks and main control unit need to be powered. Again, more energy can be conserved by switching to the “power down mode” between interleaved measurements. These three modes are listed in Table 5.2 along with their average power requirements.

Mode	**Power**	**Power Up Time**	**Sequence**	**Seq. Time**
Deep Sleep	561 mW	> 1 sec	probe transport	6 sec
Power Down	1690 mW	> 100 μsec	data transmission	5 sec
Power Up	5340 mW	-	measurement	0.250 sec

Table 5.2: Power requirements for different operating modes and their average sequence time during normal measurement operation in one position.

The average power requirement for one measurement position including several seconds for transport can be calculated with the numbers listed in Table 5.2. As a result the average required power is 1170 mW.

Lithium-Ion batteries can be used as a long-lasting energy source. Batteries with a voltage of 3.6 V and a capacity of 13 Ah are available in a suitable size for this borehole probe [39]. Two of the batteries can be switched in series to supply voltages of 3.6 V and 7.6 V for the receiver. Assuming 60% voltage converter efficiency, these batteries can power the borehole radar receiver in normal measurement cycles for approximately 30 hours. As a result, the requirement minimum of operating time defined in section 3.1 is exceeded by a factor of three.

Another requirement is the flexibility of the choice of different radar technologies. The open concept of the implementation of the receiver are summarized in the next section.

5.6 Adaptable Borehole Radar Receiver Platform

The introduction showed that there is no ideal borehole radar system with just one radar technology or a fixed center frequency. Moreover the available radar technologies have specific advantages and disadvantages. Accordingly this receiver was designed for adaptable options in hardware as well as in software.

The bandwidth and center frequency has certain limits due to the antenna design and the coupling in the antenna feed-point. The influence of this limitation is reduced by the connected flexible antenna adaption network. Despite the antenna defined input bandwidth the amplification and digitalization has a broad input bandwidth.

This wide bandwidth can be used for different radar technologies. However these technologies have other requirements for data processing which has to be incorporated into the FPGA. The flexibility of the different configurations is implemented in hardware and the configurations are selectable by software.

Although the room inside the receiver is limited, the hardware can be extended by reserved space for additional components. These additional electronic boards can be used to expand the receiver features. One of the possible add-ons is an external trigger detection circuit board to synchronize the data acquisition process with external events.

The flexible hardware is supported by a communication interface which enables the data acquisition computer running Linux or Microsoft Windows operating systems to access and control all the receiver components. Therefore not only the configuration is controlled by software, but the measurement sequence as well.

Further possibilities are added by choosing the TCP/IP protocol with Ethernet as communication interface. This widens the options on the location of the measurement software, because the TCP/IP can be used on the Internet over a wide area network (WAN) or local area network (LAN). Measurements are typically using a LAN connection whereas during the development stage of the probe or for troubleshooting a WAN is helpful to connect to the probe from anywhere in the world.

The probe presented in this chapter was evaluated conducting several measurements in a salt mine. The measurement results follow.

6

Measurement Results

The implemented receiver was evaluated in numerous field tests. These recorded measurement results are presented in this chapter. In particular the measurement data is analyzed and tested with the proposed methods according to the previous chapters.

First the receiver is tested for self-induced errors which can occur with clocked digital circuitry within the scope of the sensitive antennas. The next measurements analyze the probe features and give calibration examples by using the proposed test signals. Finally application specific measurements show the practical results achieved.

The receiver is designed for low-noise. Consequently the receiver electronics can only be analyzed in an electrical low-noise or if possible, a noise free environment. Unfortunately in a normal laboratory environment radio stations and other transmitters create a very noisy environment in the receivers frequency range. In contrast, the electrical noise underground is, in the case of most applications, practically non existent because it is absorbed by the soil.

As a result, all measurements in this chapter were conducted in salt mines at a depth of 400 m or more below the Earth's surface where the only disturbing electrical noise can come from mine equipment and local two-way radios. However these disturbances are only temporary and most of the time shielded sufficiently from the borehole radar system.

First it is important to analyze if the measurement data is distorted by the internal clocked circuits.

6.1 Self-Induced Errors and Noise Reduction With Data Stacking

In a low-noise receiver the antenna and the measurement process are very sensitive to any noise produced by active electronics in close proximity. Therefore it was a critical experiment to place the clocked receiver electronics in the middle of the antennas. A method to analyze and find self-induced errors are multiple measurements.

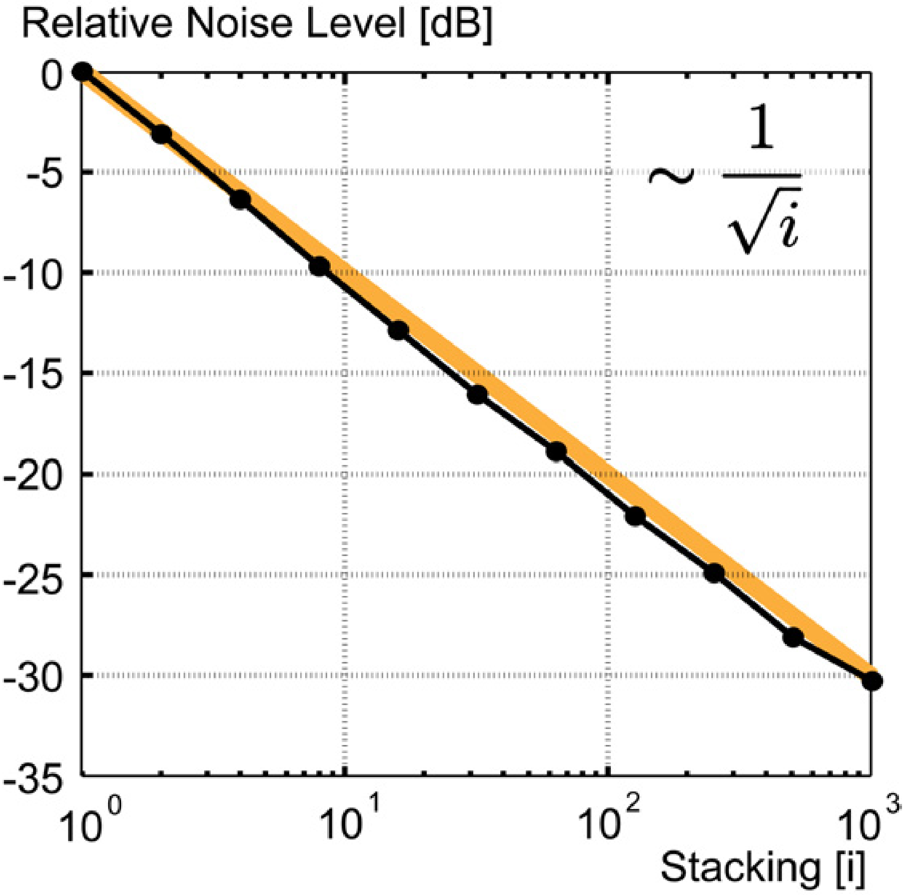

Figure 6.1: Noise level reduction as a function of data stacking (black: measured data, yellow: theoretic characteristics).

Multiple repeated measurements can be used for averaging or in other words data stacking. Data stacking improves the signal-to-noise ratio which leads to higher resolution. The gain measured in dB is calculated using Equation (6.1) with the index i representing the number of averagings.

$$\text{Relative Noise Level} = 20 \cdot \log_{10}\left(\frac{\text{Noise}_{1,\text{RMS}}}{\text{Noise}_{i,\text{RMS}}}\right) \tag{6.1}$$

Data stacking reduces the effects of random noise, however systematic errors are persistent. These systematic errors are related to the ADC clock and other recurrent system events. This fact is used to analyze the receiver for any self-induced noise.

The theoretic results of Equation (4.5) can be compared with the field measurements where noise was recorded with eight times interleaved sampling resulting in an effective sampling rate of 1000 MSPS and a number of 8192 samples. The measurement data follow the equation only if there are no additional systematic self-induced errors. The result calculated with Equation (6.1) is shown in Figure 6.1 in a log scale. It demonstrates that the measured noise figure follows the equation. The diagram indicates that there are no dominant systematic errors. Therefore the stacking reduces the random noise by a factor of $1/\sqrt{i}$. The presented measurement result demonstrates that further stacking can improve data results at the cost of excessive measurement time. The increased number of data stacking i lowers the noise as long it follows the theoretic graph. At some point the noise will not decrease with more stacking anymore due to systematic errors.

Another option to improve the signal quality by averaging is selecting a high sampling rate to acquire more data.

6.2 Influence of the Effective Sampling Rate on Measurement Data

The effective sampling rate can be changed in multiples of the fundamental analog-to-digital conversion rate $F_{s,v_1} = 125$ MSPS by changing the interleaved sampling factor ι. The measurement result for different sampling rates is shown in Figure 6.2. The measurement data was recorded during a tomography set-up where the transmitter and receiver were located in separate boreholes approximately 30 m apart. The first pulse at $t \approx 40$ nsec in the diagram represents the direct pulse of the transmitter.

The advantage of lower sampling rates is faster data processing and less energy consumption. On the other hand, echoes can be detected better if more sample points are available at the rising edges of the echoes. Additionally, the

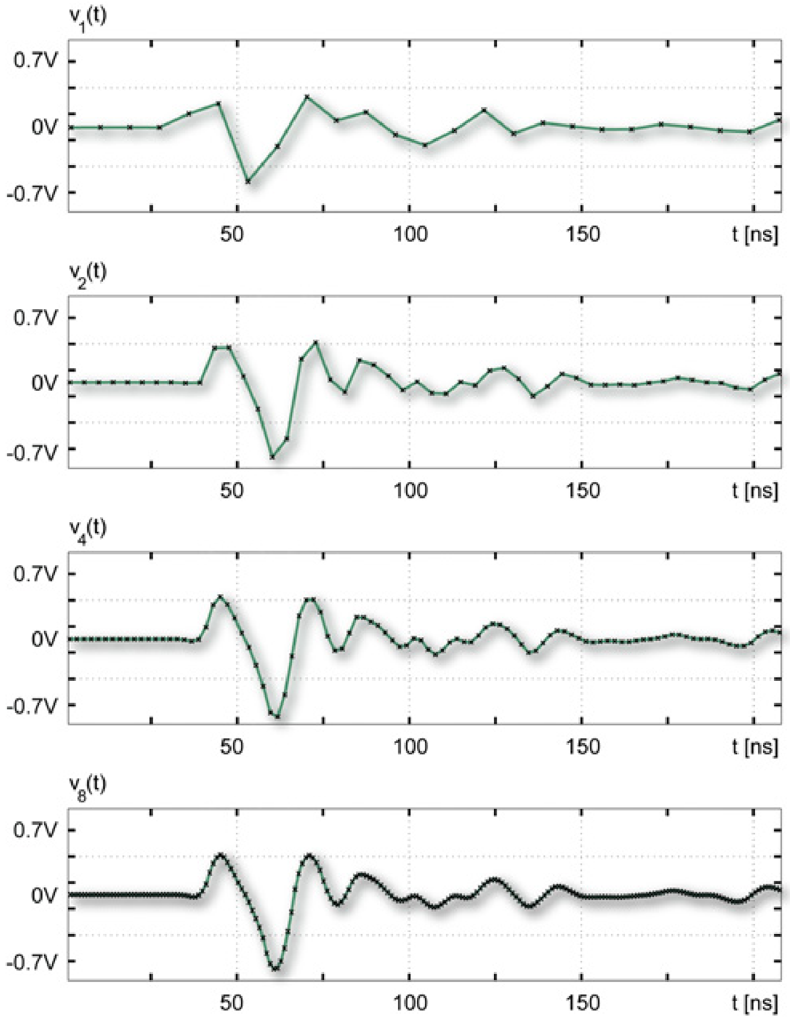

Figure 6.2: Comparison of different interleaved sampling measurements: $F_{s,v_1} =$ 125 MSPS, $F_{s,v_2} = 250$ MSPS, $F_{s,v_4} = 500$ MSPS, $F_{s,v_8} = 1000$ MSPS.

signal quality increases with higher sampling rates. In such cases where enough data for averaging is available, filtering of the recorded signals reduces noise.

The next measurement task is to estimate the parameters of the introduced test signal before analyzing the applications specific properties.

6.3 Test Signal Parameter Computation

During the field tests, the calibration signal generator was tested in the low-noise environment of a salt mine. The calibration test signal generator signal circuit designed earlier was used (Section 5.3 and Appendix A).

The first step before applying channel matching calibration or increasing the dynamic range by signal windowing is to record test signal measurement data. Thereafter the four parameters of the test signal A, τ, ω, and φ are estimated for further data processing.

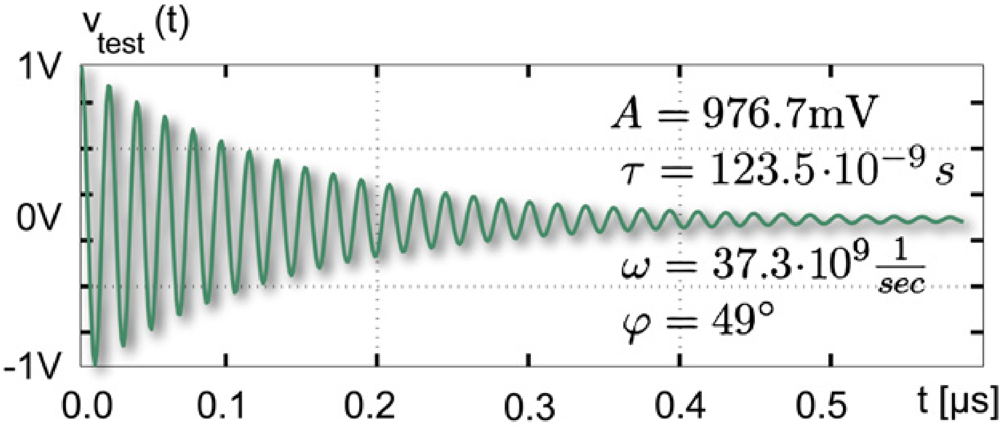

Figure 6.3: Parameter calculation for a test signal.

The parameter fitting presented in section 4.3.3 was used to calculate the parameters in Figure 6.3 for 548 samples. An ideal damped sine wave can be constructed using the parameters. Thereafter the difference of the measured test signal $v_{\text{test}(t)}$ and the ideal signal represents the present error. These residuals are illustrated in Figure 6.4.

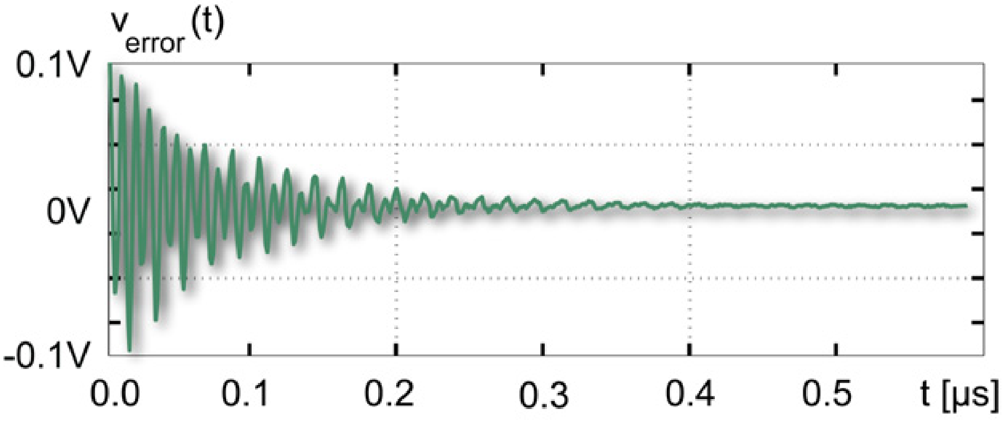

Figure 6.4: Difference of the measured test signal and reconstructed ideal signal.

The periodic error voltage $v_{\text{error}}(t)$ shows the limitations of the signal fitting process. Although this is true, the measurement results prove to be well-suited for the proposed data processing operations.

6.4 Receiver Sensitivity and Dynamic Range

The dynamic range describes the range of the lowest detectable signals to the maximum allowable input signal levels. The lowest signal level is represented by the noise floor which determines the receivers sensitivity. The dynamic range can be calculated in general with the ratio of the full-scale signal and the measured noise as in Equation (6.2).

$$\mathrm{DR} = 20 \cdot \log_{10}\left(\frac{Z_{\mathrm{FS,ADC,RMS}}}{Z_{\mathrm{Noise,RMS}}}\right) \tag{6.2}$$

The maximum input signal level is determined by the ADC full scale value $Z_{\mathrm{FS,ADC,RMS}}$. It depends on the resolution $\mathrm{ADC}_{\mathrm{bits}}$ and therefore can be calculated for a 14 Bit data converter with

$$Z_{\mathrm{FS,ADC,RMS}} = \pm\frac{2^{\mathrm{ADC}_{\mathrm{bits}}-1}}{\sqrt{2}} = \pm 5792.62 \tag{6.3}$$

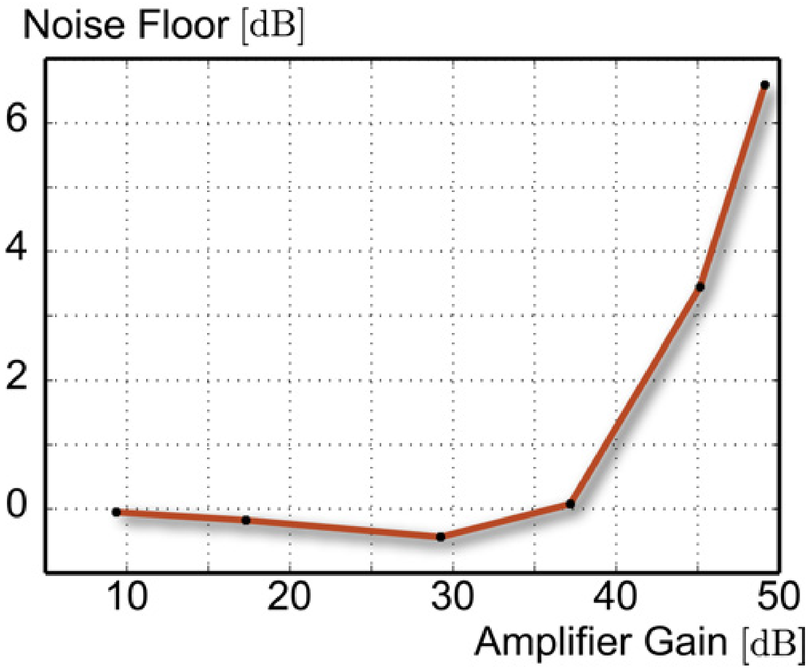

Figure 6.5: Noise floor depending on selected amplifier gain.

The noise floor $Z_{\mathrm{Noise,RMS}}$ describes the output referred noise of the input channel at the ADC setting the lower limit for the input scale. The noise of the receiver $Z_{\mathrm{Noise,RMS}}$ was measured with the fully assembled borehole probe located in a borehole. It was recorded for different amplifier gain settings as illustrated in the measurement result in Figure 6.5. The increased noise floor with higher amplifier gain corresponds well with the data sheet of the variable gain amplifier [35].

The increased amplifier noise with higher gains degrades the dynamic range. The valid input range can be illustrated in connection with the gain factors as in Figure 6.6. The first part of the graph is limited by the ADC performance whereas the latter part for a gain of more than 35 dB is degraded by the increased amplifier noise.

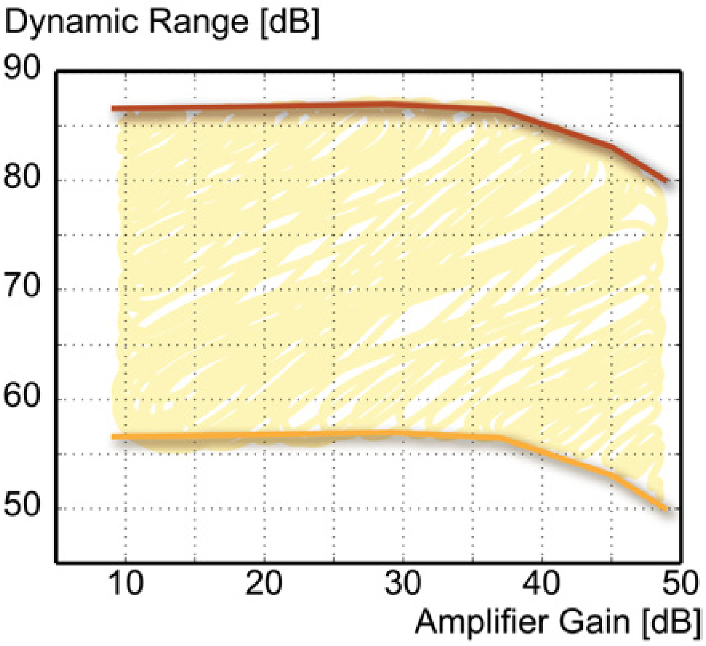

Figure 6.6: Dynamic range depending on the gain setting. The effective noise without stacking is represented by the lower graph whereas the equivalent to 1024 times stacking is depicted by the upper curve.

The boundaries of the input scale calculated in Equation (6.2) and Figure 6.5 determine the dynamic range of the receiver. Additionally, the overall maximum dynamic range $\mathrm{DR}_{\mathrm{RX}}$ of the receiver needs to consider the maximum practicable amplifier setting $\mathrm{Gain}_{\mathrm{dB,max}} = 49$ dB. Finally the dynamic range can be further enhanced by stacking of up to $\mathrm{Stack}_{\mathrm{dB}} = 30$ dB as verified earlier.

The amplifier gain is set to the highest level to detect small echo signals. As the previous measurement results showed the noise increases in such cases by up to almost 7 dB decreasing the dynamic range by the same number. Accordingly the resulting dynamic range can be calculated with Equation(6.4) considering these additional parameters.

$$
\begin{aligned}
\mathrm{DR_{RX}} &= 20 \cdot \log_{10}\left(\frac{Z_{\mathrm{FS,ADC,RMS}}}{Z_{\mathrm{Noise,RMS,min}}}\right) + \mathrm{Gain_{dB,max}} - \mathrm{Noise_{dB}} + \mathrm{Stack_{dB}} && (6.4)\\
&= 56.8\ \mathrm{dB} + 49\ \mathrm{dB} - 7\ \mathrm{dB} + 30\ \mathrm{dB} && (6.5)\\
&= 128.8\ \mathrm{dB} && (6.6)
\end{aligned}
$$

According to the above reasoning, the overall dynamic range of the receiver is 128.8 dB for a bandwidth of 100 MHz. The dynamic range benefits from a stable behavior during overmodulation events. Such receiver input overload occurs especially when high amplification levels are selected to magnify small radar echoes.

6.5 Recovery from Overmodulation

In a system with high dynamic range, overmodulation can occur quite frequently. Especially in the case of pulse radar systems the direct signal and first echo signals are quite strong causing excessive overmodulation with higher amplifier gain. Consequently the receiver is designed to handle such overmodulation quite good. The measurement results show an unnoticeable recovery time as illustrated in Figure 6.7.

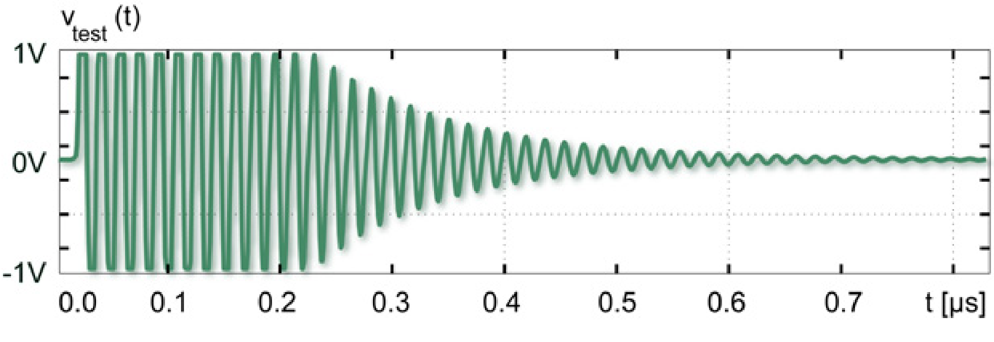

Figure 6.7: An over-modulated test signal was sampled at an effective sampling rate of 1000 MSPS.

There are several measures to prevent exorbitant distortion and to provide a stable behavior. First, the amplifier [35] provides extra clamping capabilities to prevent input overload to the subsequent ADC. Second, the ADC in turn has the ability to clip high input levels to a certain extent.

Overmodulation causes unwanted spurs in the frequency spectrum. The same is true for sampling timing errors. These timing errors can be calibrated as shown next.

6.6 Calibration of Systematic Interleaved Sampling Timing Errors

The path of the trigger signal and the accuracy of the selectable delay times are vital for a stable interleaved sampling operation of the receiver. The trigger signal is generated inside the FPGA, where routing and logic gates can cause systematic variations depending on the selected delay. Such systematic errors can be detected by recording the built-in test signal.

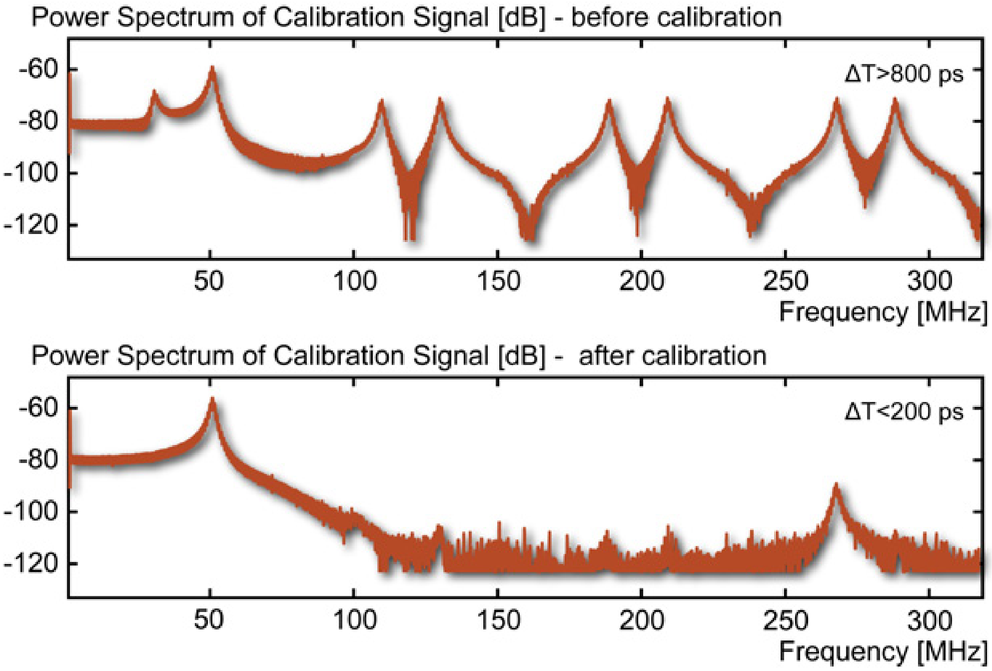

Figure 6.8: Frequency spectrum of interleave sampled calibration signal recorded with 256 times stacking. The upper graph is recorded with high sample time errors whereas the lower diagram shows the result after calibration.

The calibration signal has a frequency of approximately 50 MHz. The corresponding frequency spectrum is shown in Figure 6.8 before and after calibration [52; 63]. The effective sampling rate is $f_s = 640$ MSPS which is achieved by using an ADC with $f_{s,\mathrm{ADC}} = 80$ MSPS and 8 time interleaved sampling. The upper frequency spectrum contains systematic sampling errors. The lower part of Figure 6.8 represents the signal spectrum after calibration. The errors are much lower although some sampling errors can be still detected due to a remaining trigger time error of $\Delta T < 200$ psec which effects every of the 8 sampling sweeps. This remaining error is well below the jitter of the radar transmitter.

Sampling clock errors and jitter causes subharmonics in sidebands of the effective sampling clock frequency. The effect of these errors look similar to the consequence of sub-sampling. Figure 6.8 contains distinct characteristic spurs at 190 MHz, 210 MHz and 270 MHz. These spurs can be calculated as $3 \cdot f_{s,\mathrm{ADC}} - f_{\text{test signal}} = 190$ MHz, $2 \cdot f_{s,\mathrm{ADC}} + f_{\text{test signal}} = 210$ MHz and $4 \cdot f_{s,\mathrm{ADC}} - f_{\text{test signal}} = 270$ MHz. The quality of the interleaved sampling can be checked with the energy contained in these spurs. The frequency spectrum above tells us that the interleaved sampling can be further improved by a shift of the sampling pulses. A correction can be performed by an online calibration process where the parameters of the digitalization process are corrected through fine adjusting the transmitter trigger pulse delay. Thereafter the actual measurement data is recorded. The trigger pulse delay for each interleaved sampling interval has to be fine adjusted relative to the sampling clock for minimal errors.

The correction process can be visualized by writing the equation of the interleaved sampling signal dirac comb function $f_\iota(t)$ as in Equation (6.8), where ι is the number of interleaved sampling intervals, $F_s = \frac{1}{T_s}$ is the fundamental sampling rate of every single interleaved sweep and ΔT_k includes the sum of the correction and time error value of the delayed trigger pulse.

$$T_k = \frac{1}{\iota \cdot F_s} \tag{6.7}$$

$$f_\iota(t) = \sum_{k=0}^{\iota} \sum_{n=-\infty}^{\infty} \delta(t - k \cdot T_k - n \cdot T_s - \Delta T_k) \tag{6.8}$$

One option is to perform the calibration process manually by correcting every single interleaved sampling sweep trigger delay value ΔT_k. Afterward a test measurement result can be verified in the signal frequency spectrum. Another possibility is to implement a successive approximation algorithm for automated calibration.

An additional application for the test signal is a windowing technique with different amplification settings. It is based on the relative gain levels of consecutive measurements.

6.7 Signal Windowing Technique

The dynamic range of the receiver is extended by variable amplifiers which are connected to the analog-to-digital converters. Low amplification settings allow to record the strong direct signals from the transmitter without distortion. Distant echoes are detected by high gain settings which lead to overmodulation at the beginning of the radar trace. These separate measurements are combined to a single signal with higher dynamic range.

The variable amplifier settings should not be changed during the measurement to avoid signal distortion. Therefore different settings are applied in consecutive measurements. Such separate measurements are assembled together by defining windows for each sequence. The transitions from window to window are specified in time. This principle is well-suited for ground penetration systems because the evaluated echo signals coming from the same distance arrive at the same time with amplitudes in the same range.

The number of different amplifier settings required varies with the environment. In some cases two different amplification settings might be sufficient where as in other situations three or more are necessary. These gain settings have only limited accuracy and require a calibration measurement.

The high dynamic signal traces are recorded with multiple of the following steps per position:

1. adjust amplifier settings for measurement window
2. record radar trace with triggering radar transmitter
3. calibration measurement with all three input channels switched to test generator; the transmitter is turned off

Before the measurement signal can be assembled the parameters of the test signals, in particular the amplitudes, have to be computed by the signal fitting algorithm.

Table 6.1 shows the estimated test signal parameters for the examples below. The amplitude parameters can be used to compare the relative amplifier gain settings to the measured relative gain with Equation (6.9).

$$\Delta\mathrm{DR} = \mathrm{Gain}_{\mathrm{Win3}} - \mathrm{Gain}_{\mathrm{Win2}} - 20 \cdot \log_{10}\left(\frac{A_3}{A_2}\right) = -1.9\ \mathrm{dB} \tag{6.9}$$

Signal Parameter	**Window 1**	**Window 2**	**Window 3**
Gain Setting	12 dB	24 dB	45 dB
Amplitude A	2799.5	11512.0	161621.0
ω	$373.62 \cdot 10^6 \ \frac{1}{s}$	$373.15 \cdot 10^6 \ \frac{1}{s}$	$372.96 \cdot 10^6 \ \frac{1}{s}$
τ	$1.1992 \cdot 10^{-7} \ s$	$1.2469 \cdot 10^{-7} \ s$	$1.2089 \cdot 10^{-7} \ s$
ϕ	-1.9084 rad	-1.8767 rad	-1.7489 rad

Table 6.1: Test signal parameters for three different measurement windows.

The result in Equation (6.9) shows the importance to estimate the amplitudes of the test signals for accurate measurement performance. An additional reason is the variance of the error ΔDR as it changes with the ambient temperature.

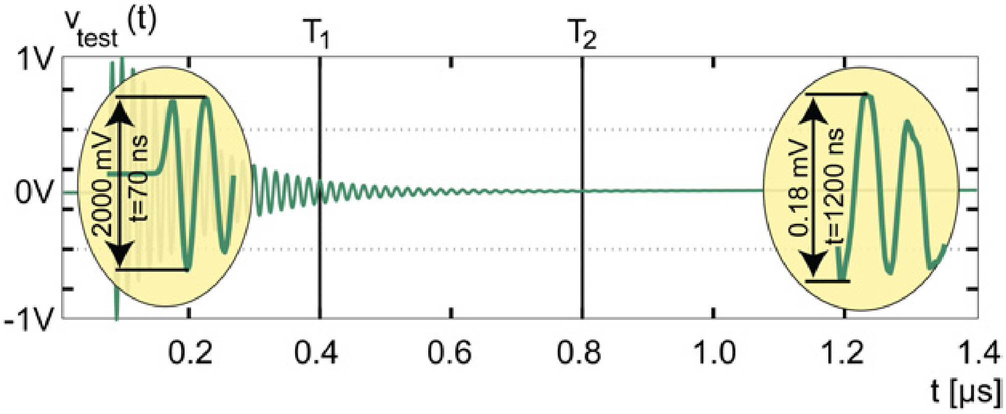

Figure 6.9: Acquired test signal with three gain windows measured with an effective sampling rate of 1000 MSPS and 512 times averaging.

The amplitude parameters are used to assemble the measurement windows with different gain settings. The implementation is demonstrated by using the internal test signal. The sequence in Figure 6.9 was recorded using three windows with transitions at T1 = 400 ns and T2 = 800 ns. The fitting process for the combined signal $v_{\text{test}}(t)$ is written in Equation (6.10). The calculation is based on the previous estimated test signal amplitudes A_1, A_2 and A_3.

$$v_{\text{test}}(t) = \begin{cases} v_{A1}(t)/A_1, & \forall\, t \leq \mathrm{T1} \\ v_{A2}(t)/A_2, & \forall\, \mathrm{T1} < t \leq \mathrm{T2} \\ v_{A3}(t)/A_3, & \forall\, t > \mathrm{T2} \end{cases} \tag{6.10}$$

The amplitude range of the test signal is measured at the beginning and the end. The resulting signal dynamics can be calculated with the maximum peak-to-peak amplitude and the minimum peak-to-peak amplitude as written in Equation (6.11).

$$\mathrm{DR}_{\text{measured, 70 ns to 1200 ns}} = 20 \cdot \log_{10}\left(\frac{2000\ \mathrm{mV}}{0.18\ \mathrm{mV}}\right) = 81\ \mathrm{dB} \tag{6.11}$$

The signal envelope for the given window can be validated with the estimated value of the declining test signal $\tau \approx 1.2 \cdot 10^{-7}\ s$. The amplitude of the test signal for the given time $T = 1130$ nsec is suppose to decline to a certain level resulting in a signal dynamics calculated in Equation (6.12).

$$\mathrm{DR}_{\text{theoretic}} = 20 \cdot \log_{10}\left(e^{\frac{T}{\tau}}\right) = 82\ \mathrm{dB} \tag{6.12}$$

The comparison of the theoretic and measured signal range of the test signal within the given window shows only a small difference of 1 dB. It proves the validity of the test signal whereby the relative small variance can be explained by parameter matching inaccuracies.

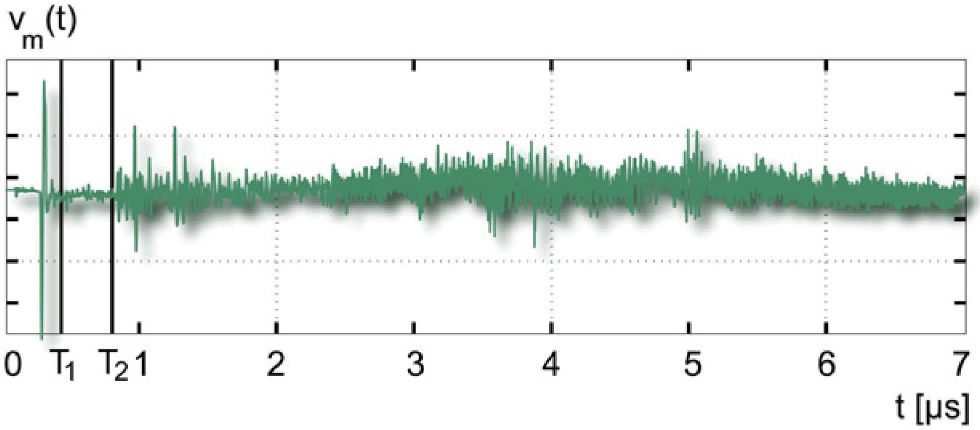

Figure 6.10: Received radar trace combined from 3 measurement windows. The effective sampling rate is 1000 MSPS with 512 times averaging.

A radar measurement was conducted using the windowing technique. The assembled result is shown in Figure 6.10. The window transitions are found, as in the previous example, at 400 nsec and 800 nsec. Additionally a smoothing function intensifies weak signals. Other methods to find distant echoes include bandpass filtering and automatic gain control. In a radargram where many radar traces are placed closely together makes it possible to identify distant echoes more reliably.

Another practical application of the test signal parameters is to detect differences of the input channels with the option to match the signals.

6.8 Channel Matching

The matching of the two loop channel is of importance to estimate the angle of the received echoes correctly. Table 6.2 shows the computed test signal parameters for an amplification of 25 dB which leads to a signal level close to the full-scale amplitude of the ADC.

Signal Parameter	**Loop 1**	**Loop 2**	$\mathbf{\Delta L_{12}}$	**Dipole**
DC offset	8237.6	8270.8	0.2 %	8319.6
Amplitude A	11037	11349	1.4 %	13179
ω	$373.68 \cdot 10^6 \ \frac{1}{s}$	$373.84 \cdot 10^6 \ \frac{1}{s}$	0.02 %	$374.27 \cdot 10^6 \ \frac{1}{s}$
τ	$1.2118 \cdot 10^{-7} \ s$	$1.2025 \cdot 10^{-7} \ s$	0.4 %	$1.1712 \cdot 10^{-7} \ s$
φ	-1.7841 rad	-1.7870 rad	0.08 %	-1.8808 rad

Table 6.2: Test signal parameters of all three input channel recorded during a test measurement with an effective sampling rate of 1000 MSPS, data stacking of 512 and an amplification of approximately 25 dB for all channels.

The test signal parameters of both loop channels and the dipole signal differ in greater amount than the loop channels among each other. This obvious difference is caused by the amplifiers as the loop signals are amplified by a dual VGA and the dipole by a single VGA. These differences in amplitude and phase can be balanced by means of the estimated test signal parameters.

The deviation of the loop channels ΔL_{12} from their average was calculated with Equation (6.13). The value is given in %. These variations are not only caused by channel mismatch but by parameter estimation due to the limited fitting accuracy.

$$\Delta L_{12} = \left| \frac{|x_1 - x_2| + |x_2 - x_1|}{2 \cdot (x_1 + x_2)} \right| \cdot 100; \tag{6.13}$$

The channel mismatch can cause noticable angle estimation errors. According to Figure 4.42 a channel mismatch of 4% leads to an angle inaccuricy of 1°. The channel matching can be extended to include the antennas itself as the next section explains.

6.9 Off-Center Detection and Antenna Symmetry Calibration

Figure 6.11: Off-center measurement in borehole EMR5 at test site Asse II.

The placement of the borehole radar receiver influences the measurement result, because the antenna properties change with the surrounding media. This is the case when the location of the antenna and the material under investigation is not symmetrical. Such an off-center position without mounted centralizers is shown in picture 6.11 [52; 63]. The data was recorded at the Asse Research Mine operated by the GSF (National Research Center for Environment and Health) [64].

An off-center position inside the borehole results in unbalanced antennas and the measurement result are affected. These effects can be detected with the test signal generator.

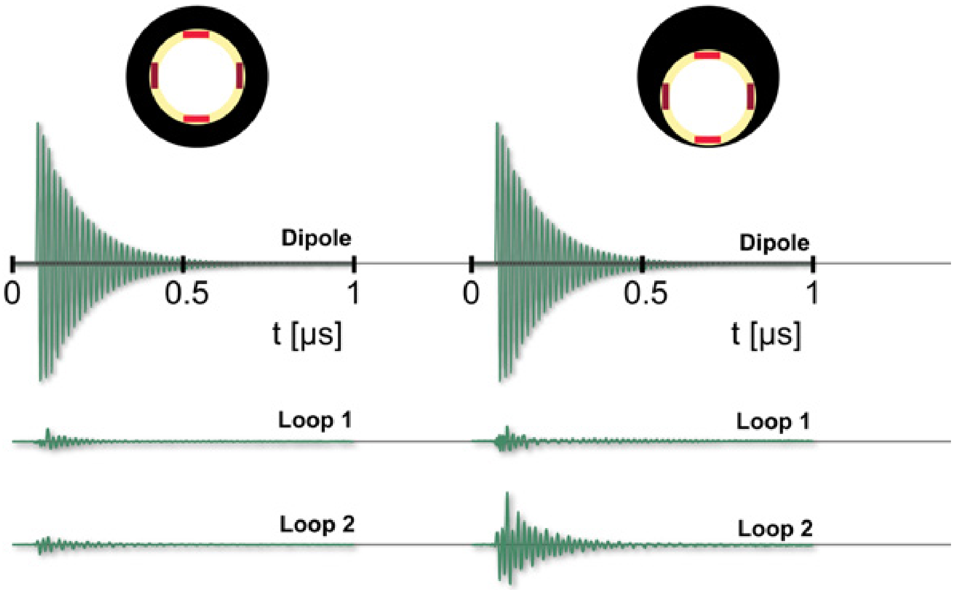

Figure 6.12: Off-center measurement data.

The test generator has the option to transmit the test signal via the dipole antenna. At the same time both loop antennas can record the received signal. This mode can be used to test the symmetry of the two loop antenna input channels. If one loop antenna has different parameters this unbalance will show in the measurement result. The antenna properties change in different media, therefore the antenna has a different characteristic when it is placed near the borehole rim.

A test measurement proves this fact as presented in Figure 6.12. Further research is required to investigate the reliability and possibilities of these measurements.

6.10 Measuring Time per Probe Position

The single measurement time determines the length of the entire measurement campaign. In turn the length of a single measurement depends on the measurement options chosen. In the following the practical achieved speeds are given by means of basic equations for the tested pulse radar transmitter.

The available pulse radar transmitter transmits pulses at a rate of up to 10 kHz or $T_{\mathrm{PRF}} = 100\ \mu$sec. The radar transmitter is triggered as often as stacking i and number of interleaving intervals ι are requested. The total measurement time T_{TMT} can be calculated with Equation (6.14) where the time for data transfer and processing is included.

$$T_{\mathrm{TMT}} = (i \cdot T_{\mathrm{PRF}} + T_{\text{data transfer}}) \cdot \iota + T_{\text{data processing}} \tag{6.14}$$

During the last measurement campaign the average overall measuring time for 8 times interleaved sampling ($\iota = 8$) and 256 times stacking ($i = 256$) was $T_{\mathrm{TMT}} = 10$ seconds. The time fraction for transferring 1024 data words is according to Equation (5.8) approximately 0.6 sec. Consequently the data processing time is calculated by Equation (6.15):

$$T_{\text{data processing}} = T_{\mathrm{TMT}} - (i \cdot T_{\mathrm{PRF}} + T_{\text{data transfer}}) \cdot \iota = 5 \text{ sec} \tag{6.15}$$

The time for data processing is the only parameter where optimization in software can be performed. It contains the setting of configuration data and among others checksum calculation. Equation (6.15) reveals that such optimization is practicable because $T_{\text{data processing}}$ is in the range of the core measurement and data transmission time.

The measurement time is an important aspect for the practical application. Faster measurements lead to reduced working hours or more radar data can be acquired. The next few sections will show measurement data of typical use of the borehole radar system.

6.11 Echo Direction Estimation

Figure 6.13: Probe setup to determine the rotational characteristics at test site Asse II, borehole EMR3.

Directivity is one of the features of this borehole radar receiver. The directivity can be analyzed by using a fixed reflector while the radar probe is turned in 5° angle steps. The angle of the reflector is known and can be compared to the angle calculated with the acquired antenna signals. A photo of a test measurement setup is shown in Illustration 6.13. The manual goniometer helps to estimate the angle whereas the internal precise angular orientation sensor [65] data is compared against the directional receiver data.

The error of the angle is evaluated by the difference of the direction determined by the two loop antenna channels and the angle of the orientation sensor $\varphi_{\text{orientation sensor}}$ as noted in Equation (6.16).

$$\Delta\varphi = \arctan\left(\frac{v_{\text{loop1}}}{v_{\text{loop2}}}\right) \cdot \frac{180}{\pi} - \varphi_{\text{orientation sensor}} \tag{6.16}$$

The recorded measurement data is visualized in Figure 6.14 for one specific reflector. The data follows the theoretic characteristic shown in Figure 3.2

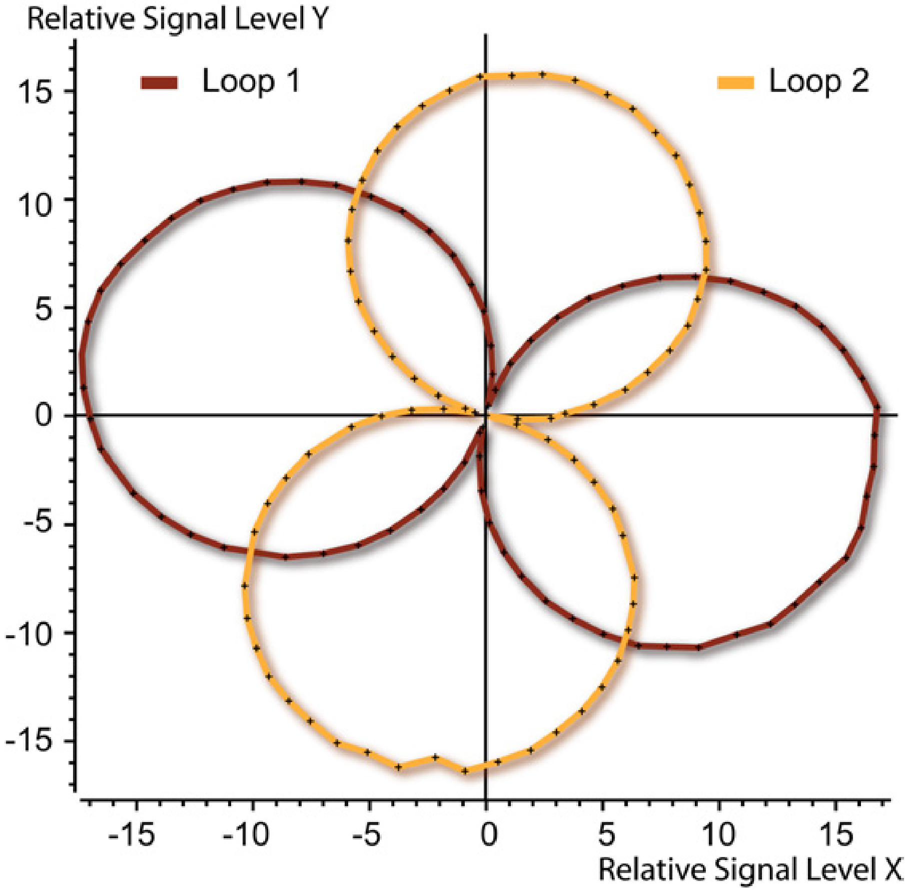

Figure 6.14: Measurement results of rotational characteristic recorded at a test site K+S, Philipsthal, Germany.

before. The angle inaccuracies primarily are caused by the antennas and their location inside the borehole.

Another measurement specific to the borehole radar application is a profile measurement.

6.12 Profile Measurement

A reflection profile measurement is recorded along the borehole. The single radar traces acquired at equidistant positions are placed closely together forming a so-called radargram. One axis of the radargram contains the distance along the borehole (z) whereas the other axis (r) represents the time. Again, the time axis can be converted into distance using the average wave propagation velocity inside the medium. In salt the velocity can be assumed with $v = 0.13\frac{\text{m}}{\text{nsec}}$ resulting in a two-way distance of 65 m per microsecond.

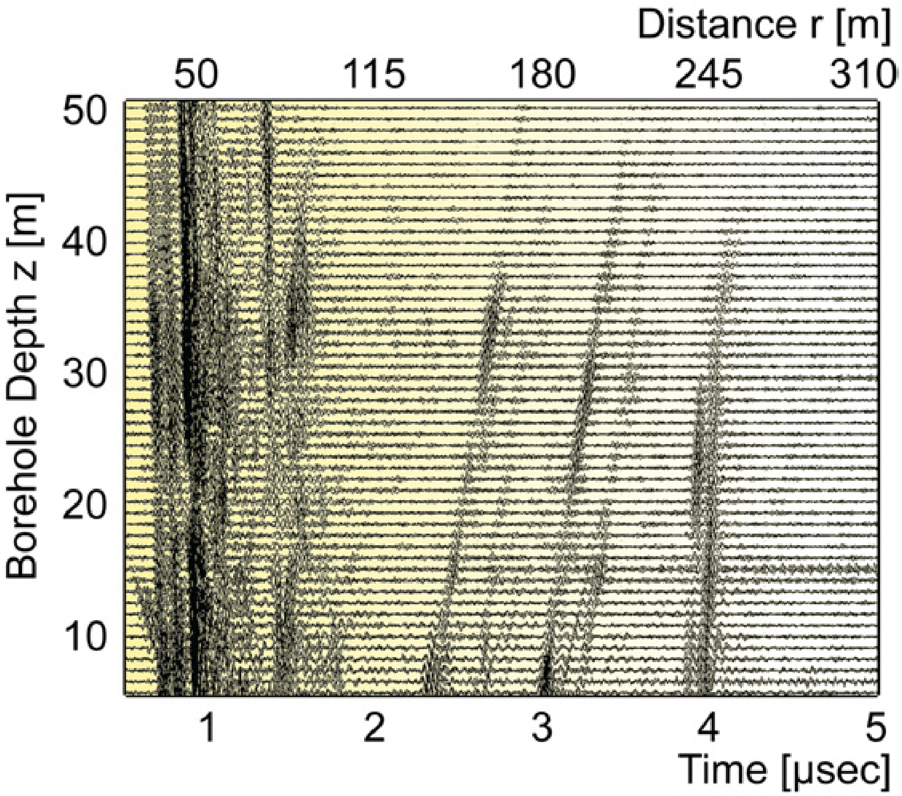

Figure 6.15: Profile measurement taken at a K+S test site, Philipsthal, Germany.

A measurement result of the dipole antenna is presented in Figure 6.15. It covers an area of 50 m in z direction and about an equivalent of 310 m in r direction. The measurement data was acquired with an effective sampling rate of 1000 MSPS and 256 stackings. The presented radargram contains clear distinct echoes up to more than 250 m with the option to extend the range by improved data processing. Such radargrams are analyzed by experts, like geophysicists, to find and map the echoes.

The achieved measurement methods and results are reviewed along with an outlook on continued work in the following concluding chapter.

7

Summary and Conclusion

Borehole radars continue to emerge as valuable electromagnetic measurement tools for geophysicists and particular the mining industry. In specific directional borehole radar systems are of interest because of the directional information. Especially in unknown areas it is difficult to locate the echo direction with omni-directional data. Such data, recorded with dipole antennas only, require extensive knowledge about the surrounding.

The highly demanded research topics of today include the secure storage of toxic and nuclear waste. In some countries like Germany, there are efforts to provide such storage in underground salt mines. These mines need to be mapped reliably. One of the research tools is a borehole ground penetrating radar.

Similar receiver designs were developed more than 10 years ago. Since then technology and research have advanced. Moreover, previous theoretical analysis showed that the implementation of a low-noise receiver in combination with calibration brings benefits, resulting in improved measurement data. Among the goals for the new probe were faster data acquisition speeds, further extended radar range and a low-power design in a compact module.

The analysis of the application showed the limitations and methods to overcome some of the challenges. A low noise design with short signal paths results in high sensitivity. On the other hand such a circuit has only limited accuracy. The relative accuracy is of special importance for the receiver antenna paths used for direction detection. Therefore one of the main research points is receiver calibration which leads to several benefits. First of all, the included test signal generator can ensure correct functionality and analyze the calibration quality at the same time. Second, the measurement data can be calibrated 'online' and 'offline' to improve the overall results. These enhancements were proved by the presented measurement results.

An algorithm for determining the test signal parameters was developed as a basis for calibration tasks. It enables monitoring of the digitalization quality as well as the channel synchronization. Moreover a windowing technique with its different amplifier gain settings, relies on the fitting of measurement signals with the test signal parameters.

Additionally an increased dynamic range is achieved by the windowing technique with test signal parameters calculation. The dynamic range is further increased by up to 30 dB with data averaging (section 6.1). As a result, a total dynamic range of 129 dB (or effective 21 Bits) at a bandwidth of 100 MHz is possible (section 6.4).

In particular it was found that echo direction detection benefits from increased accuracy with calibrated antenna channels. One of the calibration modes enables antenna calibration to a certain extent by transmitting a test signal over the antennas dipole mode. Such a calibration option can be beneficial for situations where the borehole probe is located in an off-center position in the borehole. The calibration improves the accuracy of the direction calculation.

The small size of the electronics along with the low-power requirements lead to a light weight design where no intensive cooling is required. In particular, various power-safe modes reduce the energy consumption resulting in longer continuous operation times of up to 30 hours (section 5.5) for one set of batteries.

The borehole probe uses a high speed communication with a minimum transmission rate of 0.5 MBit/sec to connect to the control software over a standard wireline logging cable. The cable can be several kilometers in length. As a result, the measurement data can be directly evaluated at the control computer located outside the borehole. In addition the implemented TCP/IP protocol enables full probe control over the Internet.

The first radar system implemented is a fully functional pulse radar. All measurements were conducted with an available borehole pulse radar transmitter. The achieved average measurement time with the pulse radar system is 10 seconds per position (section 6.10) with the potential to lower the required time to approximately 6 seconds. Such optimization would include the data transmission protocol as well as data processing.

The flexibility of the receiver opens opportunities for further work and research. The configurable electronics can be readily modified in software by means of different FPGA and microcontroller firmware. A commercial borehole probe will be built on the basis of this research where the proposed methods and findings are implemented.

Appendix A

Test Generator Schematic

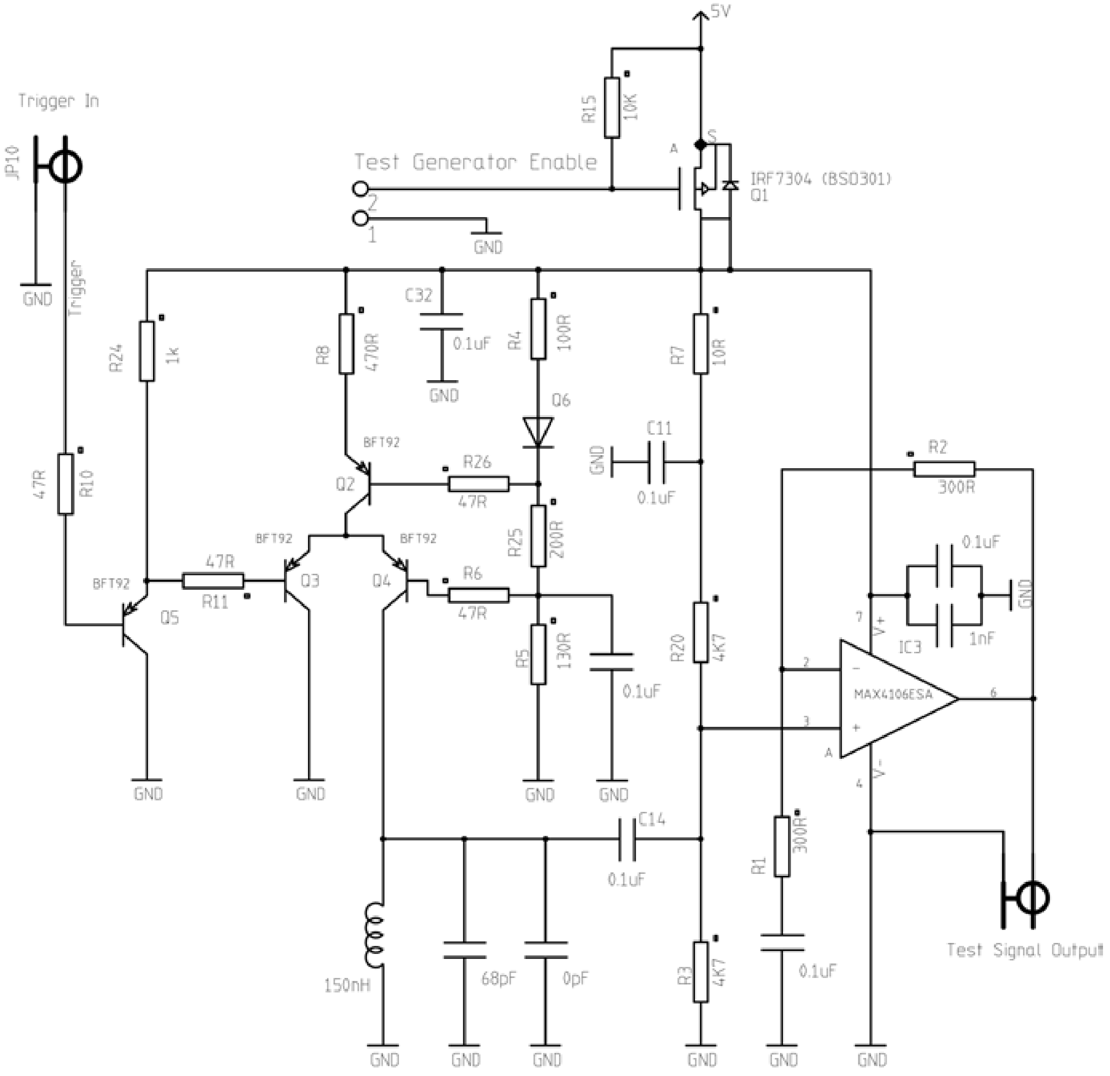

Appendix B

Test Signal Parameter Fitting Algorithm

```
function [X, Rn, Sn]=calsigpar(y,varargin)
% CALSIGPAR  five parameter fit of a decaying sine wave.
% Program for software package MATLAB
% the first 16 samples have to be on noise level
% [X,Rn,Sn]=calsigpar(y,'DW',DW, 'DTAU',DTAU, 'ADCMAX',ADCMAX,
%           'TS',TS, 'MAXCYCLE',MAXCYCLE, 'YMIN',YMIN, 'YMAX',YMAX)
%
% Input arguments:
% y: vector of measured samples, one dimension
% TS1: sampling time
% optional parameters
% YMAX: maximum input amplitude 0.1 − 1.0
% YMIN: minimum input amplitude 0.1 − 1.0
% DW:   maximum change in w during last iteration step
% DTAU: maximum change in tau during last iteration step
% MAXCYCLE − the maximum number of iterating cycle
%%
% Output arguments:
%   X: structure of  DC + A * sin(w*TVECT1 + phi) * exp(−t / tau)
%   DC   − DC level
%       A    − amplitude of the fitted sine
%       w    − radian frequency of the fitted sine
%       phi  − phase of the fitted cosine
%       tau  − decay time constant
%       erms − error amplitude, RMS value
%       srms − signal amplitude, RMS value
%  Rn: the residual vector, the difference between the data and the fitted sine−wave
%  Sn: ideal signal


% DW
if exist('DW','var')
   if (DW==0) error('DW is zero');end
```

```
   if (DW<0)  error('DW is negative');end
else
   DW=1e−15;  %DW default
end
% DTAU
if exist('DTAU','var')
   if (DW==0) error('DTAU is zero');end
   if (DW<0)  error('DTAU is negative');end
else
   DTAU=1e−15;  %DTAU default
end
% minimum test signal level [%]
if exist('YMIN','var')
   if (YMIN≤0) error('YMIN is negative or zero'); end
else
   YMIN = 0.05;   % default minimum signal level
end
% maximum test signal level [%]
if exist('YMAX','var')
   if (YMAX≤YMIN) error('YMAX is smaller or equal than YMIN'); end
else
    YMAX = 1;      % default maximum signal level
end
% set maximum of iteration cycles
if exist('MAXCYCLE','var')
   if (MAXCYCLE<1) error('maxCyc is non−positive');end
else
   MAXCYCLE=128; %MAXCYCLE default
end
% maximum ADC value
if exist('ADCMAX','var')
   if (ADCMAX<1) error('ADCMAX is non−positive');end
else
   ADCMAX = 2ˆ14 / 2; %default
end
% time base
if exist('TS1','var')
   if (TS1≤0) error('TS1 is not positive');end;
   if (TS1≥1) error('TS1 is probably the sample rate'); end;
else
   TS1=1e−9;
end

%%%%%%%%%%%%%%%%%%%%%%%%%%%%%%%%%%%%%%%%%%%%%%%%%%%%%%%%%%%%%%%%%%%%%%%%%%%%%%%%
%% (1) subtract mean value and remove second test signal, if found
%%%%%%%%%%%%%%%%%%%%%%%%%%%%%%%%%%%%%%%%%%%%%%%%%%%%%%%%%%%%%%%%%%%%%%%%%%%%%%%%
y=y(:); %force column vector for sample data
dc1 = mean(y);
y = y − dc1;
dc2 = mean(y(1:16));
y = y − dc2;
X.DC = dc1 + dc2;
silence_rms = sqrt(1/12*y(1:12)'*y(1:12))/2;
% search second test sginal and remove it, if needed
n0 = find(y==max(y));        % find maximum
```

```
Y1 = medfilt1(abs(y(n0(1):length(y))),12);
n1 = find(Y1<(silence_rms));    % find silence
Y1 = medfilt1(abs(y(n1(1):length(y))),12);
n2 = find(Y1>(silence_rms*24)); % find signal
if (length(n2)<2)
    n3 = length(y);         % no second signal
else
    n3 = n0(1)+n1(1)+n2(1);
    n3 = n3 - n0(1)-12;
end;
Y1 = y(1:n3);                     % cut signal
TVECT1=(TS1*(0:length(Y1)-1));  % time base
%%%%%%%%%%%%%%%%%%%%%%%%%%%%%%%%%%%%%%%%%%%%%%%%%%%%%%%%%%%%%%%%%%%%%%%%%%%%%%%

%%%%%%%%%%%%%%%%%%%%%%%%%%%%%%%%%%%%%%%%%%%%%%%%%%%%%%%%%%%%%%%%%%%%%%%%%%%%%%%
%% (2) search and cut signal to be fitted,
%%     signal level has to be above noise level
%%%%%%%%%%%%%%%%%%%%%%%%%%%%%%%%%%%%%%%%%%%%%%%%%%%%%%%%%%%%%%%%%%%%%%%%%%%%%%%
 n_start = 0;
 n_end   = 0;
 % find start point - first sine wave after first maximum
 if(YMAX<1)
    n_start = find(Y1>(max(Y1)*YMAX)); % find first correct amplitude
 else
    n_start = find(Y1==max(Y1));      % find first maximum
    if(length(n_start)>1)
      disp('warning: test signal overmodulation occured');
    end;
 end;
 overmod=length(n_start);       % number of overmodulated periods !=1
 n_maxmin=n_start(1);           % fist maximum
 % calculate invalid time because of overmodulation
 X.overmod_time = (n_start(length(n_start)) - n_maxmin +1) * TS1;
 if(overmod>1) % check for overmodulation
    n0 = n_start(length(n_start));
    n1 = find( Y1(n0+1:length(Y1)) == max(Y1(n0+1:length(Y1)))); % find next maximum
    n_start = n0 + n1;
 end;
 if(n_start<16) error('test signal start point not found'); end

 % find last valid rising/falling edge above noise level - zero crossings
 Y2 = Y1(n_start:length(Y1));           % cut signal
 yn = find((Y2./circshift(Y2,1))<0);    % position of zero crossings
 % start value for search, minimum number of zero crossings
 k = 4;
 if((max(Y1)*YMIN) > silence_rms)
     sigthresh = max(Y1)*YMIN;
 else
     sigthresh = silence_rms;
 end;
 while(k<(length(yn)-2))&((abs(Y2(yn(k)+2))>sigthresh)|(abs(Y2(yn(k+1)))>sigthresh))
        k = k+1;
 end;
 n_end=n_start+yn(k)+2;
 if( mod((n_end-n_start), 2) == 0) n_end = n_end + 1; end;
```

```
 if(n_end≤0) error('test signal end point not found'); end;

 %% cut signal
 Y2     = Y1(n_start:n_end);
 TVECT2 = TVECT1(n_start:n_end) - TVECT1(n_start);
 TS2    = TS1;
 N2     = length(Y2);
%%%%%%%%%%%%%%%%%%%%%%%%%%%%%%%%%%%%%%%%%%%%%%%%%%%%%%%%%%%%%%%%%%%%%%%%%%%%%%%%

%%%%%%%%%%%%%%%%%%%%%%%%%%%%%%%%%%%%%%%%%%%%%%%%%%%%%%%%%%%%%%%%%%%%%%%%%%%%%%%%
%% (3) estimate frequency by using maximum of PSD
%%%%%%%%%%%%%%%%%%%%%%%%%%%%%%%%%%%%%%%%%%%%%%%%%%%%%%%%%%%%%%%%%%%%%%%%%%%%%%%%
   F=abs(fft(Y2));
   [Mfft,w]=max(F(2:round(length(Y2)/2)));
   w=2*pi* w / length(Y2) / TS2;
   if((w<(2*pi*10e6)) | (w>(2*pi*100e6)))
      error('frequency estimation error.');
   end;
   % minimum length is 1.5 signal periods
   if((n_end-n_start)<(3*pi/w/TS2)) error('test signal too short'); end;
%%%%%%%%%%%%%%%%%%%%%%%%%%%%%%%%%%%%%%%%%%%%%%%%%%%%%%%%%%%%%%%%%%%%%%%%%%%%%%%%

%%%%%%%%%%%%%%%%%%%%%%%%%%%%%%%%%%%%%%%%%%%%%%%%%%%%%%%%%%%%%%%%%%%%%%%%%%%%%%%%
%% (4) estimate tau
%%%%%%%%%%%%%%%%%%%%%%%%%%%%%%%%%%%%%%%%%%%%%%%%%%%%%%%%%%%%%%%%%%%%%%%%%%%%%%%%
y1a = circshift(Y2,1);                                % shift forward
y1b = circshift(Y2,-1);                               % shift backward
y1maxminl = ((Y2>y1a & Y2>y1b) | (Y2<y1a & Y2<y1b));  % maximum/minimum points
y1maxmint = find(y1maxminl)*TS1;                      % time points for maxima and minima
y1maxmin  = abs(Y2(find(y1maxminl)));                 % search max/min values

tautest = 0;
kstart=1; k=1;
while (k<(length(y1maxmin)-kstart))
    tautest(k) = (y1maxmint(k+kstart)-y1maxmint(kstart));
    tautest(k) = tautest(k) / log(y1maxmin(kstart)/y1maxmin(k+kstart));
    k=k+1;
end
tautest= tautest(round(length(tautest)/4):round(3*length(tautest)/4));
tau0 = sum(tautest) / length(tautest);
tau1 = sqrt(1/length(tautest)*tautest*tautest');
tau  = tau0;
%%%%%%%%%%%%%%%%%%%%%%%%%%%%%%%%%%%%%%%%%%%%%%%%%%%%%%%%%%%%%%%%%%%%%%%%%%%%%%%%

%%%%%%%%%%%%%%%%%%%%%%%%%%%%%%%%%%%%%%%%%%%%%%%%%%%%%%%%%%%%%%%%%%%%%%%%%%%%%%%%
%% (5)  three parameters fitting - linear fitting,
%%      compute start parameters for four parameter fitting
%%      alternative: x0 = lsqr(D0,Y2,1.e-12,12)
%%%%%%%%%%%%%%%%%%%%%%%%%%%%%%%%%%%%%%%%%%%%%%%%%%%%%%%%%%%%%%%%%%%%%%%%%%%%%%%%
D0=[cos(w*TVECT2).*exp(-TVECT2/tau);sin(w*TVECT2).*exp(-TVECT2/tau);ones(1,N2)]';
x0=D0\Y2;
x0(4)=0;
%%%%%%%%%%%%%%%%%%%%%%%%%%%%%%%%%%%%%%%%%%%%%%%%%%%%%%%%%%%%%%%%%%%%%%%%%%%%%%%%
```

```
%%%%%%%%%%%%%%%%%%%%%%%%%%%%%%%%%%%%%%%%%%%%%%%%%%%%%%%%%%%%%%%%%%%%%%%%%%%%%%%
%% (6a) four parameter fitting (least square/gauß-newton) - iterate frequency
%%%%%%%%%%%%%%%%%%%%%%%%%%%%%%%%%%%%%%%%%%%%%%%%%%%%%%%%%%%%%%%%%%%%%%%%%%%%%%%
iteration=0;
while (iteration≤MAXCYCLE)
 iteration=iteration+1;
 D0=[cos(w*TVECT2).*exp(-TVECT2./tau);
 sin(w*TVECT2).*exp(-TVECT2./tau);
 ones(1,N2);
 -x0(1)*TVECT2.*sin(w*TVECT2).*exp(-TVECT2./tau)+x0(2)*TVECT2.*cos(w*TVECT2).*exp(-TVECT2./tau)
 ]';
 x0=D0\Y2;
 w=w+x0(4);                           % adjust w
 if (abs(x0(4))<(DW/TS1)) break; end  % end if accuracy is ok
end;
%%%%%%%%%%%%%%%%%%%%%%%%%%%%%%%%%%%%%%%%%%%%%%%%%%%%%%%%%%%%%%%%%%%%%%%%%%%%%%%

%%%%%%%%%%%%%%%%%%%%%%%%%%%%%%%%%%%%%%%%%%%%%%%%%%%%%%%%%%%%%%%%%%%%%%%%%%%%%%%
%% (6b) parameter fitting (least square/gauß-newton)- iterate tau
%%%%%%%%%%%%%%%%%%%%%%%%%%%%%%%%%%%%%%%%%%%%%%%%%%%%%%%%%%%%%%%%%%%%%%%%%%%%%%%
iteration=0;
while (iteration≤MAXCYCLE)
 iteration=iteration+1;
 D0=[cos(w*TVECT2).*exp(-TVECT2./tau);
 sin(w*TVECT2).*exp(-TVECT2./tau);
 ones(1,N2);
 x0(1)*TVECT2.*cos(w*TVECT2)/tau^2.*exp(-TVECT2./tau)+x0(2)*TVECT2.*sin(w*TVECT2)/tau^2.*exp(-TVECT2./t
 ]';
 x0=D0\Y2;                             % solve equations
 tau=tau+x0(4);                        % adjust tau
 if (abs(x0(4))<(tau*DTAU)) break; end % end if accuracy is ok
end;
%%%%%%%%%%%%%%%%%%%%%%%%%%%%%%%%%%%%%%%%%%%%%%%%%%%%%%%%%%%%%%%%%%%%%%%%%%%%%%%

%%%%%%%%%%%%%%%%%%%%%%%%%%%%%%%%%%%%%%%%%%%%%%%%%%%%%%%%%%%%%%%%%%%%%%%%%%%%%%%
%% (7)  compose values for model
%%       X.A*cos(X.w*TVECT2+X.phi).*exp(-TVECT2/X.tau)+X.DC
%%%%%%%%%%%%%%%%%%%%%%%%%%%%%%%%%%%%%%%%%%%%%%%%%%%%%%%%%%%%%%%%%%%%%%%%%%%%%%%
 X.DC=X.DC+x0(3);
 X.A=sqrt(x0(1)^2+x0(2)^2);
 X.w=w;
 X.tau=tau;
 if (x0(1)>0)
   X.phi=atan(-x0(2)/x0(1));
 elseif (x0(1)<0)
   X.phi=atan(-x0(2)/x0(1))+pi;
 else %x0(1)==0
   if x0(2)<0, X.phi=pi/2;
   else X.phi=3*pi/2;
   end;
 end;
 X.freq=w/2/pi;
%%%%%%%%%%%%%%%%%%%%%%%%%%%%%%%%%%%%%%%%%%%%%%%%%%%%%%%%%%%%%%%%%%%%%%%%%%%%%%%

%%%%%%%%%%%%%%%%%%%%%%%%%%%%%%%%%%%%%%%%%%%%%%%%%%%%%%%%%%%%%%%%%%%%%%%%%%%%%%%
```

```
%% (8)  create fitted signal data and calculate residuals,
%%      compute RMS values, adjust results
%%%%%%%%%%%%%%%%%%%%%%%%%%%%%%%%%%%%%%%%%%%%%%%%%%%%%%%%%%%%%%%%%%%%%%%%%%%%%%%
  A=X.A;
  Sn = [X.A*cos(X.w*TVECT2+X.phi).*exp(-TVECT2/X.tau)+x0(3)]';
  Rn = y(n_start:n_end)-Sn;
  % correct phase in regard to t=0
  X.phi = X.phi + 2*pi*mod(n_start*TS2,w/(2*pi)) -3*pi/4;
  % correct amplitude in relation to t=0
  X.A = A * exp((n_start*TS2)/tau);
  X.erms = sqrt(1/N2*Rn'*Rn);         % residual RMS value
  X.srms = sqrt(1/N2*Sn'*Sn);         % signal RMS value
  X.n    = length(Rn);                % length of fitted signal
%%%%%%%%%%%%%%%%%%%%%%%%%%%%%%%%%%%%%%%%%%%%%%%%%%%%%%%%%%%%%%%%%%%%%%%%%%%%%%%

%%%%%%%%%%%%%%%%%%%%%%%%%%%%%%%%%%%%%%%%%%%%%%%%%%%%%%%%%%%%%%%%%%%%%%%%%%%%%%%
%% calculate snr for every point with signal in time domain
%%%%%%%%%%%%%%%%%%%%%%%%%%%%%%%%%%%%%%%%%%%%%%%%%%%%%%%%%%%%%%%%%%%%%%%%%%%%%%%
 rsnr0 = 20*log10(abs(Sn./Rn));
 rsnr1 = rsnr0 + 20*log10(abs(ADCMAX./Sn));  % corrected for amplitude decline

 % relative signal-to-noise ratio, calculate RMS value
 X.snr0 = sqrt(1/N2*rsnr0'*rsnr0);           % relative signal-to-noise ratio
 X.snr1 = sqrt(1/N2*rsnr1'*rsnr1);           % snr corrected to maximum amplitude
 %%%%%%%%%%%%%%%%%%%%%%%%%%%%%%%%%%%%%%%%%%%%%%%%%%%%%%%%%%%%%%%%%%%%%%%%%%%%%%%
 %%%%%%%%%%%%%%%%%%%%%%%%%%%%%%%%%%%%%%%%%%%%%%%%%%%%%%%%%%%%%%%%%%%%%%%%%%%%%%%
```

References

[1] **Untertägige Entsorgung chemotoxischer Abfälle - Entwicklung eines richtungssensitiven Georadar-Bohrlochmessverfahrens, Entwicklung eines aktiven richtungssensitiven Bohrlochantennensystems (02C1084)**. Technical report, German Federal Ministry of Education and Research (BMBF), 2004-2008. iii, 2

[2] **Bergische Universität Wuppertal**. http://www.uni-wuppertal.de. iii

[3] **Federal Institute for Geosciences and Natural Resources (BGR), Germany**. http://www.bgr.bund.de. iii

[4] **DMT GmbH, Borehole Shuttle System**. http://www.dmt.de. iii

[5] **Sensor and Software Inc., Canada**. 2007. http://www.sensoft.ca. ix, 7, 13, 16

[6] Arthur R. von Hippel. *Dielectric Materials and Applications.* Artech House Publishers, 1954/1995. ISBN 978-1580531238. xiii, 12, 16

[7] Christian Hülsmeyer. *Verfahren, um entfernte metallische Gegenstände mittels elektrischer Wellen einem Beobachter zu melden (patent DE 165 546)*, 1904. 4

[8] H. Löwy. **Eine elektrodynamische Methode zur Erforschung des Erdinneren**. *Physikalische Zeitschrift*, **11**:697–705, 1910. 5

[9] W. Stern. **Versuch einer elektrodynamischen Dickenmessung von Gletschereis**. *Beitrag zur Geophysik*, **23**:292–333, 1929. 5

[10] W. Stern. **Über Grundlagen Methodik und bisherige Ergebnisse elektrodynamischer Dickenmessung von Gletschereis**. *Gletscherkunde*, **15**:24–42, 1930. 5

[11] R. M. Morey. **Continuous subsurface profiling by impulse radar**. *Proceedings Conference on Sub-Surface Exploration for Underground Excavation and Heavy Construction*, pages 213–232, 1974. 5

[12] R. Thierbach. **Electromagnetic reflections in salt deposits**. *Journal of Geophysics*, **40**:633–637, 1974. 5

[13] R. Unterberger. **Radar Propagation in Rock Salt**. *Geophysical Prospecting*, **26**:312–328, 1978. 5

[14] Klaus Wolny. **Untersuchung eines geoligischen Untergrundes mit Georadar**. *DPMA Erfinderaktivitäten 2001*, pages 16–21, 2001. 5

[15] D. J. Daniels. *Surface-Penetrating Radar*. Institute of Electrical and Electronics Engineers, Inc., 1996. ISBN 978-0852968628. 5, 16

[16] Satoshi Ebihara and Motoyuki Sato. **Electromagnetic Analysis and Experiments for Directional Borehole Radar Using Optical Electric Field Sensors**. In *The Sixth Well Logging Symposium of Japan*, September 2000. 7, 51

[17] **University of Sydney, School of Geosciences, Ultra-Slimline Borehole Radars**. http://www.geosci.usyd.edu.au. 7

[18] Pradip Kumar Mukhopadhyay. *Three-dimensional Borehole Radar Imaging*. PhD thesis, University of Cape Town, 2005. 7

[19] **T&A Survey BV, 3D BoreHole Radar**. http://www.ta-survey.nl. 7

[20] **Geophysical Survey Systems Inc, Salem, NH, USA**. http://www.geophysical.com. 7

[21] **MALÅ GeoScience AB**. http://www.malags.com. 7

[22] **Radarteam Sweden AB**. http://www.radarteam.se. 7

[23] Declan Vogt. **A borehole radar system for South African gold and platinum mines**. *SOUTH AFRICAN JOURNAL OF GEOLOGY*, **109**:521–528, 2006. 7, 41

[24] D.EISENBURGER, F.SENDER, AND R.TIERBACH. **Borehole Radar - An Efficient Geophysical Tool to Aid in the Planning of Salt Caverns and Mines**. *Seventh Symposium on Salt, Elsevier Science Publishers B.V., Amsterdam*, **I**:279–284, 1993. 7

[25] D.EISENBURGER, V.GUNDELACH, F.SENDER, AND R.TIERBACH. **Underground radar studies for solving geological and safeguarding problems in nuclear waste repositories**. *Proceedings of the 6th International Conference on Ground Penetrating Radar, Sendai, Japan*, pages 427–432, 1996. 7

[26] KLAUS SIEVER. **Three-dimensional borehole radar measurements a standard logging method?** In *Proceedings of the 8th Intl. Conference on Ground Penetrating Radar*, **SPIE 4048**, pages 114–120, June 2000. 7, 29, 36

[27] KLAUS SIEVER. **Low Frequency Directional Radar Logging Tool**. In *Remote Sensing by Low-Frequency Radars*, September 2001. 7, 29, 36

[28] LANBO LIU. **Geology Course 228, Lecture 11 Ground Penetrating Radar**. 2006. 12

[29] A.M. THOMAS, C.D.F. ROGERS, N. METJE, AND D.N. CHAPMAN. **Soil Electromagnetic Mapping for Enhanced GPR Utility Location**. In *Proc. of 25th International No-Dig Conference and Exhibition*, Rome, Italy, September 2006. 14

[30] JAMES CLERK MAXWELL. **A Dynamical Theory of the Electromagnetic Field**. *Philosophical Transactions of the Royal Society of London*, **155**:459–512, 1865. 14

[31] M. B. WIDESS. **How thin is this bed?** *Geophysics*, **38**:176–180, 1973. 23

[32] OLE HERMAN BJOR. **Maximum Length Sequence**. *Norsonic AS*, 2000. 28

[33] ROBERT SAURUG. *Development of a modular measuring system for the determination of roomacoustic quality dimensions.* Master's thesis, IBK - Institut für Breitbandkommunikation, Technical University Graz, Austria, 2001. 29

[34] Andreas Becker, Yi Zhou, and Volkert Hansen. **On the Calculation of the Radiation Properties of Dipole Antennas in Cylindrical Boreholes Considering Large Scatterers**. In *German Microwave Conference (GeMiC 2006)*, Karlsruhe, Germany, March 2006. 30, 37

[35] Analog Devices. *AD8331/AD8332/AD8334 - Ultralow Noise VGAs with Preamplifier and Programmable RIN*, 2006. 34, 38, 96, 102, 123, 124

[36] Conrad Nitecki. *Untersuchungen von HF-Messverstärkern mit umschaltbarer Verstärkung für die Empfangsantenne eines Bohrlochradarmesssystems.* Master's thesis, University of Wuppertal, 2005. 38

[37] C. Klarenbach, M. Kraft, C. Duncker, L. Busch, and S. Urban. **Untersuchung eines Bohrlochkabels**. *Projektarbeit am Lehrstuhl Messtechnik, Prof. Dr-Ing. A. Glasmachers, Universität Wuppertal*, 2005. 39

[38] Robert E. Blackett. **GEOTHERMAL GRADIENT DATA FOR UTAH**. *UTAH DEPARTMENT OF NATURAL RESOURCES*, page 4, 2004. 40

[39] Saft Specialty Battery Group, 12, rue Sadi Carnot, 93170 Bagnolet, France. *Primary lithium battery LSH 20*, 2006. 40, 115

[40] Erich D. Guy and Stanley J. Radzevicius. **Recognition of Borehole Radar Cable Related Effects Using Variable Offset Sounding**. *Subsurface Sensing Technologies and Applications*, **2**:13, 2001. 48

[41] Manuel Schmidt. *Elektroabsorptionsmodulatoren für den Einsatz in einem faseroptischen E-Feld-Sensorsystem.* PhD thesis, Gerhard-Mercator-Universität Duisburg, 2002. pp. 4-5. 51

[42] R. Reeder and M. Looney. **Pushing the State of the Art with Multichannel A/D Converters**. *Analog Dialogue*, **39-05**, 2005. 55

[43] W. C. Black Jr. and D. A. Hodges. **Time Interleaved Converter Arrays**. In *IEEE International Conference on Solid State Circuits*, February 1980. 57

[44] Linear Technology Corporation, 1630 McCarthy Blvd., Milpitas, CA 95035-7417, USA. *LTC2255/LTC2254 - 14-Bit, 125/105Msps Low Power 3V ADCs*, 2005. 60, 61, 102

[45] Michael Löhning and Gerhard Fettweis. **The Effects of Aperture Jitter and Clock Jitter in Wideband ADCs**. *IWADC*, 2003. 60

[46] Walter Kester. **MT-008: Converting Oscillator Phase Noise to Time Jitter**. Technical report, Analog Devices, 2005. 60

[47] Crystek Corporation, 12730 Commonwealth Drive, Fort Myers, Fl 33913, USA. *Crystek - Ultra-Low Phase Noise Oscillators CCHD/CVHD-950*, 2008. http://www.crystekcrystals.com. 60, 61

[48] B. Brannon. *AN-501: Aperture Uncertainty and ADC System Perfomance*, 2000. 61, 92

[49] O. Borchert, A. Glasmachers, and M. Aliman. **3D-Borehole Radar Data Acquisition**. In *Proceedings of the GPR2006 conference*, June 2006. 61, 66

[50] Xilinx Inc. *Virtex-4 FPGA User Guide*, 2006. 61, 104

[51] Howard Johnson. *Jitter Effects in Modern System Designs.* Signal Consulting, Inc., 2005. 61

[52] O. Borchert, M. Aliman, and A. Glasmachers. **Borehole Radar Calibration**. In *Proceedings of the 4th International Workshop on Advanced Ground Penetrating Radar*, page 19ff, Naples, Italy, June 2007. 66, 125, 131

[53] Analog Devices Corporation. *AN-737 - How ADIsimADC models data converters*, 2005. 72

[54] Analog Devices Corporation. *AD9246 - 14-Bit, 125 MSPS, 1.8 V Analog-to-Digital Converter*, 2006. 72, 95

[55] IEEE-1241-2000. *IEEE Standard for Terminology and Test Methods for Analog-to-Digital Converters.* Institute of Electrical and Electronics Engineers, Inc., 2001. ISBN 0-7381-2724-8. 80, 83, 90, 92

[56] IEEE-1057-1994. *IEEE Standard for Digitizing Waveform Recorders.* Institute of Electrical and Electronics Engineers, Inc., 1994. 80

[57] Christoph Patten. *Messtechnische Erfassung der Betriebsparameter zur Kalibrierung einer Bohrlochradar-Empfangssonde.* Master's thesis, University of Wuppertal, 2007. 80

[58] Tamas Zoltan Bilau, Tamas Megyeri, Attila Sarhegyi, Janos Markus, and Istvan Kollar. **FOUR PARAMETER FITTING OF SINE WAVE TESTING RESULT: ITERATION AND CONVERGENCE**. *Computer Standards and Interfaces*, **26**:51–56, 2004. 82, 85

[59] W.H. Press, B. P. Flannery, S. A. Teukolsky, and W.T. Vetterking. *Numerical Recipes: The Art of Scientific Computing.* Cambridge University Press, 1996. 85

[60] Philips Semiconductors / NXP. *BFT92 - PNP 5 GHz wideband transistor*, 1992. 105

[61] Ulrich Tietze and Christoph Schenk. *Halbleiter-Schaltungstechnik.* Springer-Verlag Berlin Heidelberg, 1999. 107

[62] Stollmann E + V GmbH. *BlueMod+P24 Hardware reference*, 2006. 111

[63] O. Borchert, K. Behaimanot, and A. Glasmachers. **Directional Borehole Radar Calibration**. *Journal of Applied Geophysics*, page doi:10.1016/j. jappgeo.2008.04.004, 2008. 125, 131

[64] **Asse Research Mine**. 2007. http://www.gsf.de. 131

[65] Applied Physics Systems, 1245 Space Park Way, Mountain View, CA 94043, USA. *Applied Physics System - Model 544 Miniature Angular Orientation Sensor*, 2005. 133